A MICROMECHANICALLY-INFORMED MODEL OF THERMAL SPALLATION WITH APPLICATION TO PROPULSIVE LANDING

A Dissertation
Presented to
The Academic Faculty

By

Kenneth A. Hart Jr.

In Partial Fulfillment
of the Requirements for the Degree
Doctor of Philosophy in the
School of Aerospace Engineering
Department of Aerospace Engineering

Georgia Institute of Technology

Dec 2021

A MICROMECHANICALLY-INFORMED MODEL OF THERMAL SPALLATION WITH APPLICATION TO PROPULSIVE LANDING

Thesis committee:

Prof. Julian Rimoli, Advisor
Aerospace Engineering
Georgia Institute of Technology

Prof. George Kardomateas
Aerospace Engineering
Georgia Institute of Technology

Prof. Robert Braun
Graduate Aerospace Laboratories
California Institute of Technology

Dr. Charles Campbell
Engineering Directorate
NASA Johnson Space Center

Prof. Claudio Di Leo
Aerospace Engineering
Georgia Institute of Technology

Date approved: December 7, 2021

Energy and persistence conquer all things.

Benjamin Franklin

For my family

ACKNOWLEDGMENTS

Special thanks to my advisor, Prof. Rimoli. It has been a privilege to be in his research group and I have become a capable numerical solid mechanics researcher thanks to him. Our first endeavour together was mesh generation, which started with blue noise distributions and grew into an open source mesh generator, used in several research groups across the world and officially recognized in NASA's Software Catalog. His expertise in coupled diffusion and solid mechanics modeling was integral to the success of this thesis. It was also a joy to share the opportunity to teach finite element analysis and introduce students to FEA software. Our academic lineage includes luminaries like Kirchoff, Prandtl, Timoshenko, and Ortiz - and I am proud to use the word *our*. I truly appreciate everything you have done for me.

I would also like to thank the members of my thesis committee. To Prof. Braun, for giving me opportunities to work on a variety of entry, descent, and landing research projects. These projects ignited my passion to study, understand, and solve EDL challenges. I am also grateful for his mentorship and guidance through my masters project on analytic rarefied aerodynamics and the associated papers we co-authored. To Chuck Campbell, for giving me the opportunities to intern at NASA Johnson Space Center with astrogeologists and for guiding me towards the study of landing site alteration for human-scale Mars landers. Last but not least, I would like to acknowledge Profs. Di Leo and Kartomateas for their thoughtful feedback and support in preparation of this thesis. With the help of this committee, I have co-authored four conference papers and four journal articles with 33 citations total, and released two open source projects that are depended on by at least 24 other software projects. I appreciate all of your help; thank you.

The support of my friends and fellow graduate students has been essential to completing this thesis. Starting in the beginning with Brad Steinfeldt, who helped me transition into a graduate student. I'd also like to acknowledge the Club 209 cohort - Hisham, Casey, Alex,

Peter, and Kyle - we shared a deep zeal for learning and we shared a lot of good times. Byron, Terry, and Fear have been truly reliable friends; and I have many fond memories with my fellow students in the SSDL. In the CSML, I would like to acknowledge Amir, Aarohi, Hernan, Julie, and Daniel for your camaraderie and support. My friends helped me throughout graduate school and I am very grateful to have them in my life.

For my family members, who were always supportive of me during graduate school, I am eternally grateful. I could not have done it without you. I would also like to acknowledge the moral support and patience given by my steadfast partner. Finally, I would like to acknowledge my COVID-19 rescue dog, for being a constant source of joy and a very good boy- perhaps the best.

I gratefully acknowledge the support for this work offered by the National Aeronautics and Space Administration under cooperative agreement 80NSSC17M0058.

TABLE OF CONTENTS

LIST OF TABLES

LIST OF FIGURES

LIST OF ACRONYMS

3D-XRD 3D X-ray diffraction

AABB Axis-aligned bounding box

ARES Astromaterials Research and Exploration Sciences

CDF Cumulative distribution function

CFD Computational fluid dynamics

DNS Direct numerical simulation

DSMC Direct simulation Monte Carlo

EBSD Electron backscatter diffraction

ETH Eidgenössische Technische Hochschule

FEM Finite element modeling

FFT Fast Fourier transform

LOX Liquid oxygen

NASA National Aeronautics and Space Administration

ODB Output Database, from Abaqus

PDE Partial differential equation

PDF Probability density function

PICA Phenolic impregnated carbon ablator

RNG Random number generator

RVE Representative volume element

TPS Thermal protction system

TSL Traction separation law

VTOL Vertical take-off and landing

X-μCT X-ray microtomography

XFEM Extended finite element modeling

NOMENCLATURE

Latin Letters

A	Area
a	Semi-axis length along x-axis or crack length - see context
b	Semi-axis length along y-axis
C	Cost or stiffness - see context
C_p	Specific heat at constant pressure
c	Semi-axis length along z-axis
c_v	Coefficient of variation
D	Damage parameter for cohesive zones
d	Euclidean distance
E	Young's modulus or cohesive stiffness - see context
$\mathbb{E}$	Expected value
F	Force
G_c	Fracture energy
h	Convective heat transfer coefficient
h_c	Contact conductance

K	Stiffness matrix
K_{IC}	Fracture toughness
k	Thermal conductivity
l	Left branch
n	Number density or normal vector - see context
$\mathcal{O}$	Order of growth for an algorithm
p	Probability, pressure, or parent branch - see context
Q	Rotation matrix from the body frame to the crystal lattice frame
q	Rotation quaternion
q''	Heat flux
R	Region
R^2	Coefficient of determination
r	Radius or right branch - see context
SA	Surface area
T	Temperature
t	Time or traction - see context
u	Displacement
V	Volume
v	Recession rate
$\mathbb{Z}$	Set of integers

Z Standard normal

Greek Letters

α Relative overlap tolerance between seeds or coefficient of thermal expansion - see context

Δx Spall size

δ Gap displacement

ε Strain

ϵ Levi-Cevita symbol

Θ Temperature difference

κ Thermal diffusivity

μ Mean of distribution or lognormal parameter - see context

ν Poisson's ratio

ρ Density

σ Stress tensor, standard deviation, or lognormal parameter - see context

Subscripts

0 Initial

f Fraction or final - see context

g Gas

ijk Indices

lmn Indices

M	Melt
n	Normal
$pqrs$	Indices
s	Spallation or transverse direction - see context
t	Second transverse direction

SUMMARY

During the propulsive landing of spacecraft, the retrorocket exhaust plume introduces the landing site surface to significant pressure and heating. Landing site materials include concrete on Earth and bedrock on other bodies, two highly brittle materials. During a landing event, defects and voids in the material grow due to thermal expansion and coalesce, causing the surface to disaggregate or spall. After a spall is freed from the surface, the material beneath it is exposed to the pressure and heat load until it spalls, continuing the cycle until engine shutdown. Spalls and debris entrained in the exhaust plume risk damaging the lander or nearby assets- a risk that increases for larger engines. The purpose of this work is to develop a micromechanically-informed model of thermal spallation to improve understanding of this process, in the context of propulsive landing. A preliminary simulation of landing site spallation, utilizing an empirical thermal spallation model, indicates that spallation may occur for human-scale Mars landers. This model, however, was developed for drilling through granite, which has a fundamentally different microstructure compared to typical landing sites, necessitating a more general approach. To that end, highly-detailed simulations of thermomechanical loading, applied to representative microstructures, inform a functional relationship between applied heat flux and spallation rate. These representative microstructures can be generated using an algorithm that has been validated for a wide variety of materials, including basalt from Gusev Crater, Mars.

CHAPTER 1
INTRODUCTION

1.1 Plum-Surface Interaction

Plume-surface interaction is the modification of a surface by exposure to an impinging gas. For aircraft, jet engine exhaust has caused spallation of runways and thermal buckling of aircraft carrier flight decks. [1] For rockets, launch and landing pads are damaged by the exhaust plume, requiring specialized materials and routine maintenance. Other planetary bodies do not have landing pads, which has caused problems for past surface missions and creates risks for future missions. [2] There are three primary concerns for plume surface interactions: soil entrainment, debris transport, and surface damage. This work focuses on the surface damage component of plume surface interaction.

Each celestial body has unique plume-surface interaction considerations. On Earth, launch and landing primarily occur on prepared surfaces, such a concrete structures or steel plates. These surfaces are used many times, so concrete erosion and steel warping need to be minimized. On the Moon, the impinging exhaust of a descending vehicle entrains regolith into the flow. This high-speed regolith can abrade the surfaces of nearby assets and reduce the visibility of features at the landing site. The entrainment of rocks and pebbles may also become a concern for lunar landers targeting the bottom of craters, where braccia and solid rock are more prominent above the regolith layer. On Mars, there are three broad categories of landing sites: the dunes, bedrock, and the poles. The dunes would likely have soil entrainment issues for propulsive landers, while at the poles the CO_2 ice at the landing site would sublimate. For a bedrock landing site, which may be covered by a layer of regolith, there is a risk of debris transport and surface alteration. For comets and asteroids, such as rubble piles, an impinging rocket plume may cause ice to sublimate or cohesion

damage. Landers on other bodies may not need propulsive landing, such as Titan with its significantly dense atmosphere. The plume-surface interactions are different at each celestial body. Reusability is most important on Earth, while minimizing landing risk is more important for other celestial bodies.

The plume surface interaction community is actively addressing multiple facets of this problem. Dr. Philip Metzger of NASA Kennedy Space Center and the University of Central Florida is using Apollo data and simulations to study the entrainment of regolith on the Moon and other airless bodies. [3, 4] Dr. Manish Mehta at NASA Marshall Space Flight Center is investigating soil erosion at Mars due to pulsed and continuous thrust. [5, 6, 7] Also at Marshall, Dr. Daniel Allgood is investigating an active cooling system for rocket flame deflectors and Dr. Peter Liever is simulating landing plume environments and debris transport for heavy landers. [8, 9] At the California Institute of Technology, Dr. Josette Bellan is developing a gas-granular flow simulation that predicts the soil crater morphologies from Mars Science Laboratory. [10] Finally, the author and Prof. Rimoli are simulating landing site plume impingement at the Georgia Institute of Technology.

Simulations of erosion processes have been created for propulsive landing on the Moon and Mars. On the Moon, exhaust plumes expand into vacuum, requiring a hybrid CFD and DSMC solution for the flowfield. [11, 12] Critical to the erosion process is the boundary layer flow. In this region, regolith particles can be simulated in a number of ways, however the primary erosion process is viscous erosion. [13] Regolith particles can be treated as a second phase in the flowfield, or they can be modeled directly. [14, 10] By contrast, erosion on Mars is primarily due to diffuse gas explosive erosion. [5] The atmosphere on Mars collimates the exhaust plume and creates deep pits in the regolith layer that expose the surface beneath it. The simulation of regolith erosion on the Moon and Mars remains an active area of research and is closely related to the focus of this thesis.

1.2 The Thermal Spallation Process

The damage process is also known as thermal spallation, which occurs on the surface of ceramics, concrete, and rocks exposed the heat. It occurs naturally on planetary bodies that experience cyclic heating. [15, 16] Spallation is a common term for the removal of small pieces of a material and it is used in several domains. In particle physics, it refers to the splitting of heavy atomic nuclei through collision with a high energy particle. [17]. In impact mechanics, spallation refers to material fragmenting from shockwaves propagating through a material. [18] In entry, descent, and landing, it refers to the removal of large pieces of ablative heat shields during hypersonic entry. [19] In the context of this thesis, thermal spallation refers to the removal of material from the surface of a brittle material exposed to a jet of high-temperature gas. This is distinct from ablator spallation in that the material is exposed to dissociated flow and catalysis does not occur.

The three major steps in the spallation process are shown in Figure 1.1, which is reproduced from [20]. After step (c), the material beneath the spall is heated and the cycle repeats until the heat source is removed.

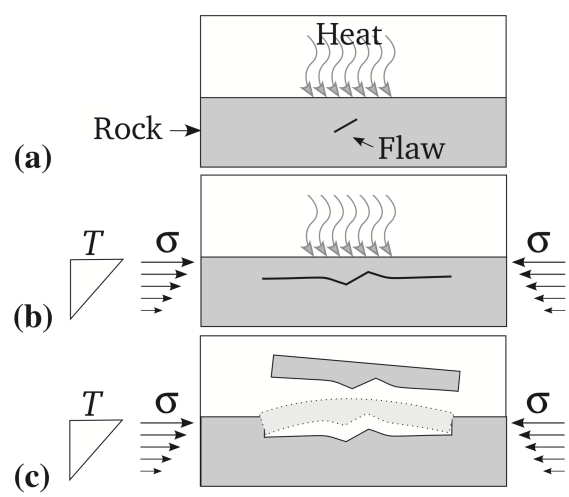

Figure 1.1: Spall-production model proposed by Preston [21, 22]: (a) An applied heat flux increases the temperature of the rock face, increasing the compressive stresses adjacent to the surface. (b) The compressive stresses cause fractures to grow parallel to the surface from incipient flaws in the rock. (c) Upon reaching a critical size, the heated region buckles and is ejected from the surface as a spall.

During the first step, the heat applied to the rock causes a temperature rise. The temperature rise is highest on the surface, then diminishes deeper into the material. This temperature rise results in a compressive stress in the material. The material beyond the region where heat is applied can be treated as a fixed boundary and when a material cannot strain despite a rise in temperature, the result is a compressive stress.

In the second step, stress in the material causes the propagation of existing flaws or defects in the material. Rocks have excellent resistance to compressive stresses, however pure compression is equivalent to pure shear in a frame rotated 45°. As shown in Figure 1.1(b), the crack begins propagating along a line rotated 45° from the direction of the applied stress. The crack propagates and eventually aligns with the that direction.

As the crack propagates, a spall begins to form as illustrated in Figure 1.1(c). From this perspective, the spall is a column that grows in length. Eventually the stress reaches the column's buckling load and the spall is liberated from the material. The spall removes some of the heat imparted onto the material, however it also exposes the new surface to the source of heat. After the spall is liberated, steps (a)-(c) are repeated for the rest of the material.

For concrete, the process is modified to include pores. The pores contain water at room temperature, however that water quickly evaporates into steam as heat is applied. The vapor applies pressure to the pore walls, which eventually fail and grow into a flaw. Rebar reinforcement also changes the progression of thermal spallation. The thermal conductivity of steel is much higher than concrete, so once bare rebar is exposed, heat is transmitted transversely and the affected area grows beyond the heated area.

1.3 Examples of Thermal Spallation

Damage due to thermal spallation is mitigated or avoided in most cases. Fires have caused significant spallation damage in tunnels, with the Tauern tunnel fire recessing 40 cm of concrete nearest the fire and spalling 600 m^3 overall. [23] One beneficial use of thermal

spallation, however, is in drilling deep boreholes through competent rock, since the drill head does not directly contact the bottom of the hole. [24, 25, 26] The exhaust from vertical takeoff and landing (VTOL) aircraft has damaged runways. [27, 28] Rockets also cause thermal spallation at landing pads, such as the Morpheus landings at NASA Kennedy Space Center. [29] Predicting recession due to thermal spallation is the first step in developing a mitigation strategy.

1.3.1 Structures Exposed to Fire

Figure 1.2: View of the damage to the Tauern tunnel. [23]

One example of spallation is the Tauern tunnel fire. This fire occurred on May 29th, 1999 in a 7 km tunnel in Austria along an important highway connecting Germany and Italy. [23] Construction work closed one of the two lanes and a phasing error in the traffic signals resulted in a truck colliding at full speed with a waiting queue. The truck immediately caught fire and a fire continued to burn in the tunnel for approximately five hours. As seen in Figure 1.2, spalled concrete covered the pavement in the tunnel. Spallation caused

the sidewalls of the tunnel to fail, though the ceiling remained intact Approximately 40 cm of the sidewall concrete had spalled away from a 100 m section of the tunnel. Overall, 600 m^3 of concrete had spalled from either the sidewalls or the ceiling of the tunnel.

1.3.2 Deep Borehole Drilling through Granite

Thermal spallation is used as contact-less drilling technique for deep boreholes in granite. [24, 30, 31, 32, 33, 34] A schematic of thermal spallation drilling is given in Figure 1.3. Rotary and percussive drill heads wear over time, requiring regular replacement. The associated cost of replacing drill heads makes geothermal energy generation, using temperature differences in Earth's crust to create electrical energy, prohibitively expensive. Flame jet drill heads do not contact the granite directly, reducing the cost of drilling these deep boreholes.

Recent advances in thermal spallation have replaced the flame with a supercritical water jet. [35, 36, 37] With a higher density than an exhaust gas, the water impinges with greater pressure on the surface. The water in the jet can be supplemented with chemicals such as sodium hydroxide to improve performance, as shown in Figure 1.4. [34]

Thermal spallation drilling has motivated most of the prior investigations into testing and modeling the spallation process.

1.3.3 Jet Aircraft Takeoff and Landing

For VTOL aircraft, their exhaust impinges on the paved surfaces of an airfield during takeoff and landing. Examples of VTOL aircraft include the Harrier and the F-35. [39, 40] The engine exhaust impinges normally to the pavement, increasing temperatures by 500-800 $^\circ$ C. Mixing fibers into the concrete has been proposed to mitigate spallation at airfields, since fibers provide channels that allow the evaporated moisture content to travel along the fibers rather than apply pressures to the pore walls. Specifically, polypropylene fibers are well-suited to mitigating spallation of concrete. [41] Much of the details regarding VTOL

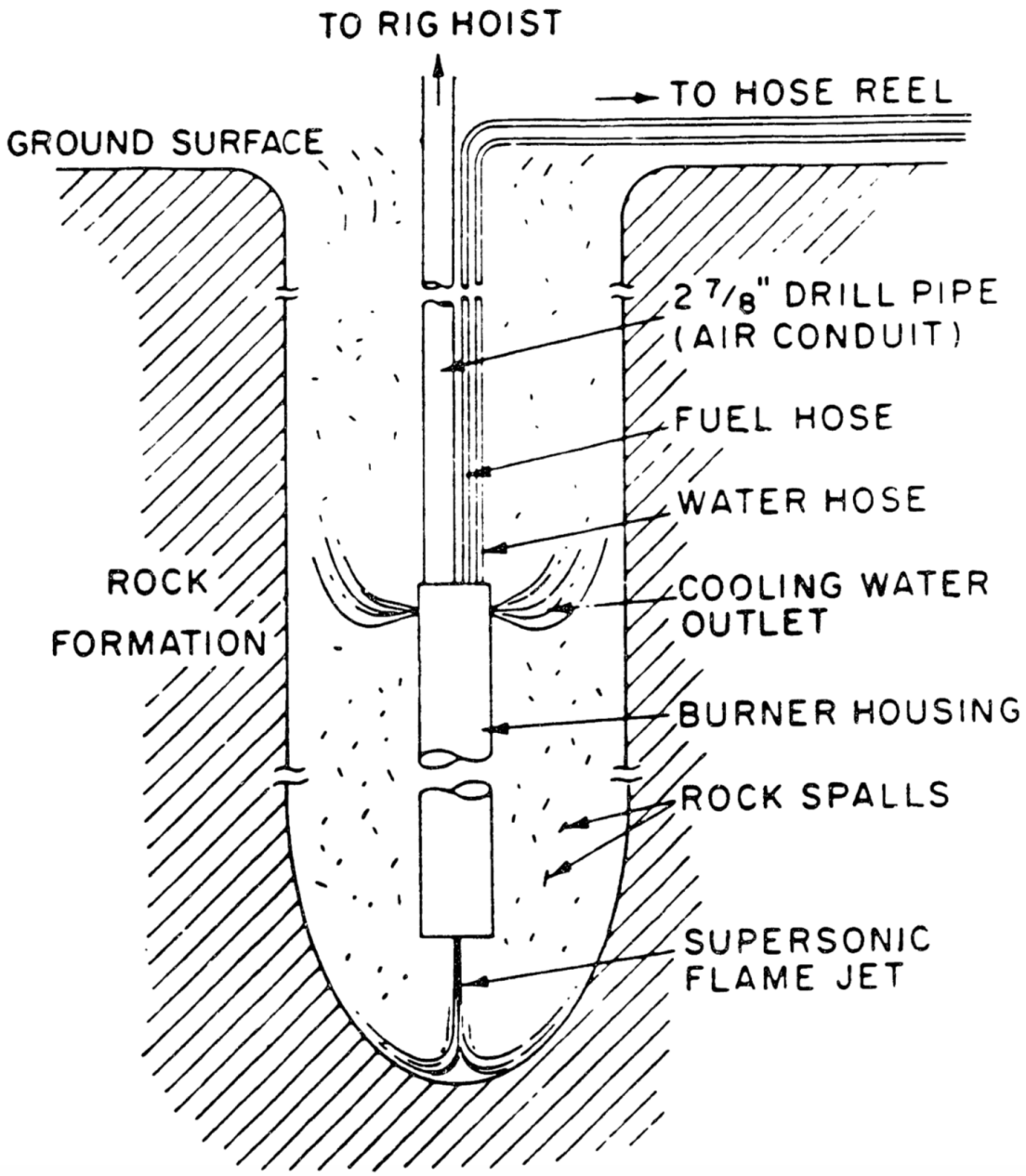

Figure 1.3: Schematic of thermal spallation drilling. [38]

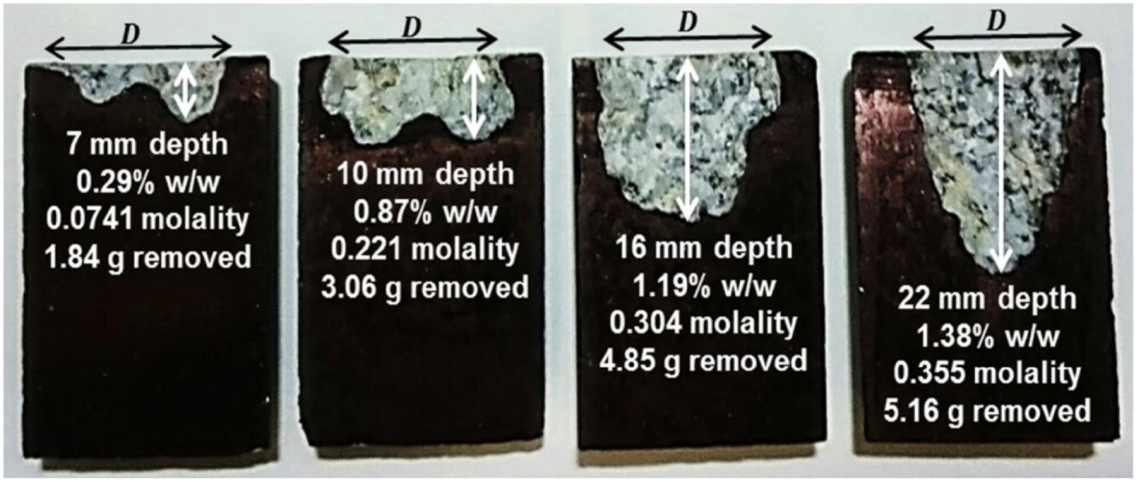

Figure 1.4: Ten minutes of Barre granite spallation with NaOH. [34]

Figure 1.5: F-35B in a vertical landing operation. [39]

jet blast and military airfield maintenance are, unfortunately, not available to the general public.

1.3.4 Landing Rockets

Figure 1.6: SpaceX CRS-10 first stage landing.

The SpaceX Falcon 9 and Falcon Heavy launch vehicles have first stages that return to Earth's surface and land on either a barge or a landing pad, such as Flight 30 shown in Figure 1.6. When the boosters are firing and have spent nearly all of their fuel, they detach from the launch vehicle and rotate such that the engines are towards the direction of motion. A boost-back burn targets the landing site, followed by a terminal burn to arrest the momentum of the booster. The booster is powered by Merlin engines, which burn kerosene and liquid oxygen (LOX) and throttle down to approximately 250 kN of thrust during landing. As the booster approaches a landing site, the visible portion of the exhaust plume interacts with the surface for roughly 4 seconds before engine shut down.

CFD analysis of the first stage during landing approximates the extreme conditions at the surface of the landing pad. [42] The core flow stagnates to 3000 K on the pad, while the baseplate of the vehicle sees exhaust at 500 K and experiences an average heat flux of 100 kW/m^2 of heat flux. Heat fluxes for the pad were not calculated, however by assuming

similar heat transfer coefficients for the baseplate and the pad, the heat flux is approximately 600 kW/m^2, or 60 W/cm^2, not including radiation.

Figure 1.7: Pitted concrete due to impinging exhaust at Landing Zone 1.

Boosters land on either an autonomous ship or a landing pad near the launch site. The deck of the ships are steel plates, which are repainted after each landing. The landing pads are made of concrete, which has spalled immediately beneath the engine and in the general vicinity. As seen in Figure 1.7, the top layer of cement has been removed, while the aggregate remains and creates a pitted texture on the landing pad surface.[1] The most likely cause for this pitting is rapid vaporization of water in the cement. Vapor pressure acts on the pore walls, causing microcracks to expand and network until the steam, and the cementing material, is freed. Damage to the drone ship deck has not been reported for successful landings.

[1]Reproduced from "SpaceX Landing Zone One - Sacred Ground 04-23-2016" by *USLaunchReport* on YouTube.

1.4 Previous Investigations

1.4.1 Ablative Thermal Protection Systems

Spallation of ablative thermal protection systems (TPS) has been characterized and studied as it hinders performance of the system. For example, the Galileo probe experienced significant heating at Jupiter and spallation of the heat shield was anticipated prior to launch. [19] Experimental results indicate 1.4 mm/s of recession occurred specifically from spallation when 300 MW/m^2 of heat flux is applied to a sample of chopped-molded carbon phenolic. Overall, the material recessed at 8.3 mm/s, with the majority of the recession caused by thermochemical mass loss. Spallation in the carbon phenolic did not occur for heat fluxes below 150 MW/m^2, which is two orders of magnitude higher than the thermal spallation of rocks. The FEAR ablative recession code solves the combined heat and mass transfer equations with multiple heat sources, but does not include spallation. [43] For the *Curiosity* rover, which used a phenolic impregnated carbon ablator (PICA), char spall was deemed very difficult to predict reliably. [44] While research data is available for char spall of TPS materials, the heat fluxes onto these materials are two orders of magnitude higher than the heat fluxes that induce spallation in geological materials.

1.4.2 Experimental Studies

Early studies of thermal spallation relied heavily on observations. Spallation occurs naturally in rocky outcrops due to the Earth's diurnal cycle. [15] Clay bricks also spall at the edges and corners. [21, 22] Modern empirical models are built on observations under controlled conditions, such as the total temperature and standoff distance of the jet. [25, 26] The onset of spalling in sedimentary rocks was investigated in the context of underground coal gasification. [45] Spallation of high-performance concrete structures due to fire poses a serious risk of structural failure. [46, 47] For normal and lightweight concretes, the onset of spallation is driven primary by moisture content and compressive external loads. [48]

Recently, a relationship between the aspect ratio of spalls and the penetration rate has been observed for flame jet spallation. [49]

Williams et al. tested the thermal spallation of many different rock types. [50] They determined whether spallation drilling could be used on a given rock type, and how to operate a drill to induce spallation. For example, limestone would not spall when exposed to a flame jet, however it began to spall irregularly when an alternating heating a quenching system was used instead. They confirmed that granite spalls readily, as well as concrete and sandstone. Other rock types either did not spall or they produced rough hole patterns.

A significant amount of experiments have been performed on Barre granite, so called for its proximity to Barre, Vermont. [24, 34, 37, 38, 51] This particular granite is considered to have similar properties to the granite deep in the Earth's crust. Similar studies have also been performed on granite from the Central Aare and Westerly regions. [36, 32, 31, 38] These studies have focused on the development of thermal spallation drilling technologies. Such developments include reducing the flame temperature and modifications to the fluid flow. For example, an rapid heating and quenching cycle can produce faster recession rates compared to heating only. Data on the thermal spallation of Barre granite are used in chapter 5 to validate the model.

1.4.3 Analytic Modeling

Analytic models are valuable for understanding parametric sensitivity and rapid analysis. The onset conditions for thermal spallation of high-strength concrete have been determined analytically. [52] An analytic approximation to the elastic-plastic transition temperature and plastic behavior of concrete at fire temperatures was developed following the 1996 Channel Tunnel fire. [53] The recession rate for flame jet spallation drilling has recently been modeled analytically, though it predicts spallation temperatures approximately 100 K below experimental results. [32]

One of the most fundamental analytic models is derived from the 1D semi-infinite solid

solution to the heat equation. [24] For a solid with constant, isotropic thermal properties subjected to a constant heat flux, the temperature distribution in that material is given by Equation 1.1.

$$T(x,t) = T_0 + \frac{2q''}{k}\sqrt{\frac{\kappa t}{\pi}}e^{\left(\frac{-x^2}{4\kappa t}\right)} - \frac{q''x}{k}\text{erfc}\left(\frac{x}{2\sqrt{\kappa t}}\right) \tag{1.1}$$

At time t_s, spallation begins and the surface temperature remains constant. The surface temperature is given by Equation 1.2, and the temperature after a time interval Δt is given by Equation 1.3. Linearizing Equation 1.3 about $\Delta t = 0$ yields Equation 1.4.

$$T(0,t_s) = T_0 + \frac{2q''}{k}\sqrt{\frac{\kappa t_s}{\pi}} \tag{1.2}$$

$$T(v\Delta t, t_s + \Delta t) = T_0 + \frac{2q''}{k}\sqrt{\frac{\kappa(t_s+\Delta t)}{\pi}}e^{\left(\frac{-v^2(\Delta t)^2}{4\kappa(t_s+\Delta t)}\right)} - \frac{q''v\Delta t}{k}\text{erfc}\left(\frac{v\Delta t}{2\sqrt{\kappa(t_s+\Delta t)}}\right) \tag{1.3}$$

$$T(v\Delta t, t_s + \Delta t) \approx T(0,t_s) + \frac{q''}{k}\left(\sqrt{\frac{\kappa}{\pi t_s}} - v\right)\Delta t + \mathcal{O}(\Delta t)^2 \tag{1.4}$$

To maintain a constant surface temperature, the condition in Equation 1.5 is imposed, which results in the relationship in Equation 1.6. Substituting Equation 1.2 into Equation 1.6 results in an analytic expression relating the applied heat flux, surface temperature rise, and recession rate, given by Equation 1.7.

$$\lim_{\Delta t \to 0}\left[\frac{T(v\Delta t, t_s + \Delta t) - T(0,t_s)}{\Delta t}\right] = 0 \tag{1.5}$$

$$v = \sqrt{\frac{\kappa}{\pi t_s}} \tag{1.6}$$

$$v = \frac{2q''}{\pi \rho C_p (T_s - T_0)} \tag{1.7}$$

The relationship in Equation 1.7 relates the recession rate to the heat flux and surface temperature rise. The minimum temperature rise depends on the properties of the material. Using the Weibull statistics approach, the minimally required temperature rise is given by Equation 1.8.[24, 38]

$$T_s - T_0 = 39.65 \left(\frac{q''}{k}\right)^{3/23} \left(\frac{1-\nu}{E\alpha}\right)^{20/23} \tag{1.8}$$

The parameters of Equation 1.8 are specific to granite, and they depend on *a priori* knowledge of the spall sizes and Weibull parameters for the material. Comparing the powers on the two terms in this equation, the temperature rise is strongly dependent on the stiffness and coefficient of linear expansion.

1.4.4 Numerical Simulation

Initial numerical simulations were developed by Rauenzahn and Wilkinson, two students of Prof. Jefferson Tester. [24, 38] These CFD simulations modeled the fluid flow within a borehole, then use Weibull statistics for the liberation of spalls. Later models assumed a heat flux, or convective heating parameters, for the fluid flow and used FEM to directly model spallation. [20, 36, 54]

Rauenzahn developed a 2D axisymmetric CFD model of the fluid flow within a borehole. [25, 26] The solver used second order upwind finite differences and explicit time advancement. Grid cells were algebraic, though orthogonality was enforced and would create degenerate quadrilateral cells at the grid boundary. Convective boundary conditions were put on the borehole boundary for heat transfer to the material. This heat flux was propagated through the material using FEM heat transfer. Overall, the CFD model was intended to have fidelity in measuring the penetration rate of a thermal spallation drill.

Temperature predictions in the material match very well with thermocouple data. Hole diameter predictions are also accurate to within 10%. Quantities such as the penetration rate and the spallation temperature were not reported.

Wilkinson improved on this simulation by increasing the complexity of the CFD model. [38] A turbulent boundary layer with multiple k-ϵ regions is introduced, to account for the presence of spalls in the flow. Additionally, a finite volume formulation where fluxes are calculated using a Roe scheme. The finite differences are taken centrally, rather than upwind, with artificial dissipation added for stability. The grid generation was also improved, from an algebraic grid to an elliptic one. This simulation also accurately predicts the borehole geometry, and it improves on the Stanton number predictions. While simulation of the flowfield was greatly improved, the model did not predict penetration rate or spallation temperature were not reported.

Walsh began the study of thermal spallation at the grain scale. [20, 55, 56] The GEODYN code simulates both the flowfield and the thermoelastics within geological materials. [57] The synthetic microstructure of the material was created by Voronoi tessellation, with the locations of the seed points optimized to fit a desired grain size distribution. Constant-temperature isotropic mineral properties were applied to the grains. The results of the model confirmed Weibull statistics trends in the Rauenzahn model. Spalls formed by this model follow a lognormal size distribution, which met expectations from experimental data. Direct comparison of the GEODYN model against experiments was not available in the literature. GEODYN is unavailable to the public, so the model cannot be reproduced or independently validated.

The von Rohr research group at ETH Zurich has also conducted tests and developed models of thermal spallation of granite. [31, 32, 33, 36, 58] They developed an implicit model relating the recession rate (v) to material properties of the granite and the measured dimensions of spalls. This model is given in Equation 1.9, where a is the average flaw size, Δx is the average thickness, h is the convective heat transfer coefficient, and T_g is the

gas temperature. This is a useful order-of-magnitude model to indicate whether spallation could be a concern for a given scenario.

$$\frac{0.57K_{IC}(1-\nu)}{E\alpha}\sqrt{\frac{\pi}{4a}} = \frac{\kappa}{vk+h\kappa}h(T_g - T_0)e^{-v\frac{\Delta x}{\kappa}} \tag{1.9}$$

Recently, Saksala created a numerical simulation using a staggered, one-way coupling of the thermal solution to a fully dynamic mechanical solution. [54] The material is modeled as an ordered mesh of equal triangles, with a mineral attribute assigned randomly to each triangle based on the composition of the granite. Constant temperature isotropic material properties are assigned to each mineral, and elements are enriched with embedded discontinuities to allow for crack propagation once the elastic limit is reached. The model reproduces spallation temperatures from [58], however recession rates were not reported.

1.5 Scope of the Work & Contributions

This thesis is focused on the direct numerical simulation of thermal spallation. This simulation numerically solves the governing equations for thermoelasticity. Since validation data is available for a polycrystalline material, granite, a microstructure mesh generator was developed to produce polycrystalline meshes. This mesh generator is used to create a granite mesh, that is then subjected to the same conditions as the validation data. After validating the simulation, it is applied to a polycrystalline Martian rock to demonstrate its predictive ability. Predicting thermal spallation is important for materials that will be subjected to significant heat flux, but cannot be tested experimentally.

The organization of this thesis is as follows. Chapter 1 introduces the process of thermal spallation and the state of the art. Chapter 2 contains an empirical model for landing site spallation. Chapter 3 describes the physics of spallation, the governing equations, and the numerical solution process. Since this process requires a discretized mesh of the material microstructure, chapter 4 discusses the process by which a microstructure description is

converted into a mesh. In chapter 5, the numerical process from chapter 2 is applied to a mesh from chapter 3 and the results are compared against experimental results. Chapter 5 also includes the results for Martian rock. Lastly, chapter 6 summarizes the key findings of the thesis and suggests future work to further develop numerical models of thermal spallation.

1.5.1 Statistical Microstructure Generator with Direct Geometry Control

A statistical microstructure generator creates computational representations of material microstructure with the same statistical distributions, such as volume fraction and grain size. The algorithm developed in this thesis creates unstructured finite element meshes with prescribed grain size, shape, orientation, and position distributions. In addition to grains, the software also supports amorphous phases, voids, and cracks. The current state of the art is a widely-used microstructure code that iteratively positions and weights seed particles to minimize the sum squared error between input and output distributions. Alternatively, the algorithm presented generates a microstructure in a single pass by sampling the input statistical distributions to create seeds, packing those seeds into a representative volume element (RVE), then tessellating the RVE to create a mesh. Inclusions and voids with arbitrary aspect ratio are implemented by extending a multi-sphere approximation, found in discrete element modeling (DEM) of granular media, from axisymmetric ellipsoids to the general case. A wide variety of material microstructures can be created using this algorithm, which is implemented in the open-source package MicroStructPy.

1.5.2 Stochastic Homogenization of Spallation Recession Rates

Spallation is a micro-scale phenomenon that contributes to the macro-scale recession of material. It is computationally intractable to model every millimeter-sized grain at a 3D landing site on the scale of meters, but homogenizing the material enables tractable modeling. Models for the average spallation rates of terrestrial materials have been developed in

the context of thermal spallation drilling, however these models are empirical and capture only the average recession rate. In reality, material defects are not uniformly distributed in the material, so the homogenized recession rate is a distributed quantity. Micromechanical modeling has been applied to studying the onset of thermal spallation; this work seeks to apply it to determine the effective recession rate of the material. This method advances the state of the art by supplementing empirical models with a physical model of recession rate.

CHAPTER 2

EMPIRICAL SIMULATION OF LANDING SITE SPALLATION

2.1 Introduction

Missions to the surface of other bodies in our solar system often decelerate before touchdown using retrorockets. Retrorocket exhaust impinges on the surface and exposes the material to temperatures similar to the combustion chamber temperature, especially as the lander reaches the surface. [59] This extreme temperature rise at the surface may initiate spallation of the landing site, resulting in non-uniform local terrain. The erosion pattern at the landing site depends on the vehicle configuration, landing trajectory, and the material properties of the landing site. Unfavorable conditions may result in an unstable landing. This work describes an empirical model of landing site spallation for rapid prediction of the erosion pattern and iteration on vehicle or trajectory design.

Previous investigations focus on the erosion of regolith at the landing site. These were motivated by the Apollo, Viking, Phoenix, and Curiosity missions. Laboratory experiments reveal the different erosion mechanisms as well as key parameters, while numerical simulations have been used to evaluate the effectiveness of mitigation strategies. Damage and erosion of the surface beneath the bedrock has not been considered in previous plume-surface interaction research. Relevant research has been conducted in the context of spallation drilling, an alternative drilling technology that may enable cost-effective production of geothermal energy. Though spallation is inherently a microstructural phenomenon, the macroscale recession rate has been empirically linked to the material properties of the material and heat convection from the jet. This result is applied to landing plume impingement, where the recession rate is spatially distributed due to unequal heating and evolves over time as the lander approaches the surface.

2.2 Methodology

Modeling landing site spallation requires two sub-models: one for the exhaust plume impingement and one for the recession rate due to spallation. A source flow model is used to create the plume, which is appropriate for low pressure bodies. Heat convection is computed by the source flow model and input into an empirical recession rate model, along with the material properties of the surface. Advancing time by Δt, the surface is recessed by $u\Delta t$, the vehicle position changes by $\mathbf{v}\Delta t$, then the plume and recession rates are recomputed for the next time step. The simulation continues until the lander reaches a final height above the surface.

The source flow model used in this simulation is JSC-26507. It was initially developed for the Reaction Control System (RCS) for the Space Shuttle to understand the pressure and heat transferred onto the International Space Station (ISS). As such, the model assumes that the exhaust expands into vacuum. Gas properties are defined by spatial distribution functions, rather than solved on a grid. These functions are based on computational fluid dynamics (CFD) results for the core flow, direct simulation Monte Carlo (DSMC) for the rarefied flow, and bridging functions are used for the transitional flow. The resulting source flow model obeys the conservation of mass and energy. Source flow modeling assumes that there are no interactions between exhaust plumes, for landers with multiple engines.

The recession rate model was developed in the context of thermal spallation drilling. [32] The model is one-dimensional, as a borehole is, but rocks have generally poor thermal conductivity so it is reasonable to assume that heat is deposited into the exposed surface without conducting deeper into the material. The recession rate is set by solving Equation 2.2 for v. If v, exceeds the limit set Equation 2.3, the applied heat flux will cause phase change in the surface material, effectively stopping the spallation.

$$\Theta_s = \frac{0.57K_{IC}(1-\nu)}{E\alpha}\sqrt{\frac{\pi}{4a}} \tag{2.1}$$

$$\Theta_s = \frac{\kappa}{vk + h\kappa} h(T_g - T_0) e^{-v\frac{\Delta x}{\kappa}} \tag{2.2}$$

$$v_M = \frac{\kappa}{\Delta x} \ln\left(\frac{T_M - T_0}{\Theta_s}\right) \tag{2.3}$$

Since the heat transfer coefficient, h, and gas temperature, T_g, vary with position on the surface, spallation recession rate, v, is also spatially varied. In the plume model, the impingement surface is assumed to remain flat despite the spallation, which is valid considering the total recession is approximately 1-2 orders of magnitude smaller than the size of the landing site. As such, there is one-way coupling between the plume model and recession model. Convective heating is computed for a given engine and trajectory, then processed by the spallation model to compute recession rate as a function of time. Integrating these rates yields the total recession distribution at the landing site.

2.3 Results

This landing site spallation model is applied to a human-scale Martian lander at a basaltic sandstone landing site.[60] The properties of the lander and landing site are given in Table 2.1. During landing, two of the six descent engines continue to fire to reduce the vehicle's thrust-to-weight ratio. This simulation considers the original design, where the cant angle is swept, and a variant where it is held constant.

The landing site recession for the vehicle in [60] and the constant-angle variant are shown in Figure 2.1. In both cases, spallation creates a shallow crater in the surface approximately 8 cm in depth. Sweeping the cant angle out results in the crater forming 1 m further away from the center of the vehicle, compared to the constant angle case. The increased distance between the spallation crater and the vehicle reduces the risk of instability on the landing legs.

Table 2.1: Lander and landing site properties

Property	Value	Units	Property	Value	Units
Chamber pressure	6	MPa	Young's modulus	20	GPa
Chamber temperature	3385	K	Poisson's ratio	0.3	
Specific heat ratio	1.2		CTE	11.6	$\mu\epsilon$/K
Nozzle area ratio	300		Fracture toughness	1.2	MPa-m$^{1/2}$
Nozzle exit diameter	1.41	m	Initial temperature	273	K
Specific Impulse	300	s	Thermal conductivity	3	W/m-K
Cant angle	45	°	Density	2300	kg/m^3
Landing speed	0.75	m/s	Specific heat capacity	375	J/kg-K
			Melt temperature	2000	K

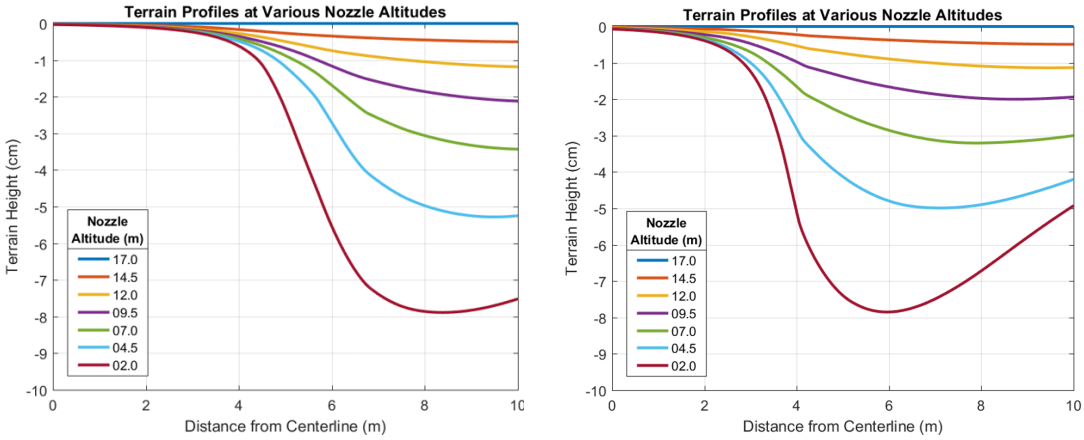

(a) Variable cant angle (b) Constant cant angle

Figure 2.1: Landing site spallation for human Mars lander

CHAPTER 3

THERMOMECHANICAL MODEL & NUMERICAL SOLUTION

This chapter discusses the underlying physics of thermal spallation, how those physics are captured by a model, and the numerical process for solving that model. The primary goal of this model is to predict the recession rate of the material as a function of the applied heat flux. Since there is an abundance of experimental data on the spallation of granite, this chapter focuses on developing a direct numerical simulation of polycrystalline materials. The model is equally valid for other polycrystalline rocks, such as basalt. First this chapter provides the background information on thermal spallation physics and governing equations, before detailing a high-fidelity direct numerical simulation of the thermal spallation of rocks.

3.1 Polycrystal Physics of Igneous Rocks

Igneous rocks are one of the three main types of rocks, along with sedimentary and metamorphic rocks. They form from cooled lava, a process that takes tens of thousands of years for granite, days for basalt, and seconds for obsidian. The longer the lava cools, the larger the mineral crystals in the rock. Which minerals form in the rock depends on the relative abundance of elements in the lava. As the crystals solidify and fuse together, flaws and defects occur at the boundary between them. Large rocks have both medium and small scale defects, but a small piece of that rock will have only small scale defects. Smaller samples have lower flaw densities, and as such the strength of a rock depends on its size. The crystal lattices form strong bonds between the atoms in their lattice, however from one crystal to another the bond is significantly weaker. These weaker grain boundaries provide a path of least resistance for damage to spread.

3.1.1 Formation of Igneous Rocks

Igneous rocks form during the cooling of lava and contain larger crystals when given more time to cool. Intrusive igneous rocks form when lava flows into cracks or faults in pre-existing rock beds. Rocks are generally poor conductors of heat, so the intrusion retains much of its heat for tens of thousands of years. Extrusive igneous rocks form when lava flows out of the crust and cools through convection with the air or through quenching in water. Granite is an intrusive rock, while basalt is extrusive. These two rocks also differ in their mineralogy. Igneous rocks are also classified by their silica (SiO_2) content. Granite has a high silica content, classifying it as a felsic igneous rock. Basalt is less than half silica, which classifies it as a mafic rock. Igneous rocks can also be porous, such as scoria, depending on the amount of dissolved gasses in the magma.

A special case of igneous rock formation occurred on Mars approximately 4 billion years ago. Magma on the surface of Mars was slowly crystallizing, with the olivine crystals coalescing faster than the other minerals due to its higher diffusivity in magma. [61] An event caused the basalt to solidify nearly instantaneously, leaving the other minerals in very small grains relative to the olivine. This event is most likely the loss of the Mars magnetic field. Based on the sizes of the crystals, including the large olivine crystals, and the diffusivity of these minerals, the time between the event and when the magma first flowed onto the surface could be estimated. The relative size of the olivine crystals and the diffusion rates of the minerals can be used together to determine how much time past between the first appearance of the magma on the surface and the event that cooled it instantly. For the basalt at Gusev crater, Martian history is embedded in the microstructure of the rock.

3.1.2 Brittle Fracture

Igneous rocks are brittle materials and fail due to brittle fracture, as opposed to ductile fracture. [62] A major difference between ductile and brittle materials is that a brittle ma-

terial is significantly strong in compression than it is in tension. Failure also occurs nearly instantaneously, whereas a ductile material will continue to deform plastically after yielding. For granite, the unconfined tensile strength is an order of magnitude smaller than the unconfined compressive strength. The qualifier *unconfined* refers to a lack of confining pressure, which would increase the ultimate strength of the material. The Mohr-Coulomb failure theory captures this additional hydrostatic stress, however it does not accurately predict failure with a tensile principle stress. [63, 64] The Hoek-Brown theory improves the tensile failure prediction compared to Mohr-Coulomb by introducing a non-linear bend to the failure envelope. [65, 66] Brittle fracture occurs nearly instantaneously when a brittle material, such as a rock, experiences stress than exceeds its failure envelope.

3.1.3 Scale Effect on the Strength of Rocks

Rock samples have different strength values depending on their size. [66, 67] Figure 3.1 shows that larger granite samples have diminishing strength until a floor is reached. This trend is a matter of scale, where large rock samples may have a density of very small flaws and a density of medium size flaws. A small sample cannot contain a medium size flaw, therefore it may have the same density of very small flaws but zero density of medium flaws. Overall, the density of flaws in the small sample is lower. A lower density of flaws results in higher strength of the sample. Increasing the sample size, eventually all of the flaw sizes are represented and a further increase in size would not result in further diminution of the strength.

Strength size-dependence is an important property of rocks that illustrates the importance of scale. Material properties and simulations must use a common scale, otherwise the effects of natural flaws and defects may be under- or over-represented in the simulation results. For thermal spallation specifically, experimental results and prior numerical models indicate that this phenomenon occurs on the grain scale. Consequently, the strength of large masses of granite would be too low for a simulation on the scale of tens of grains.

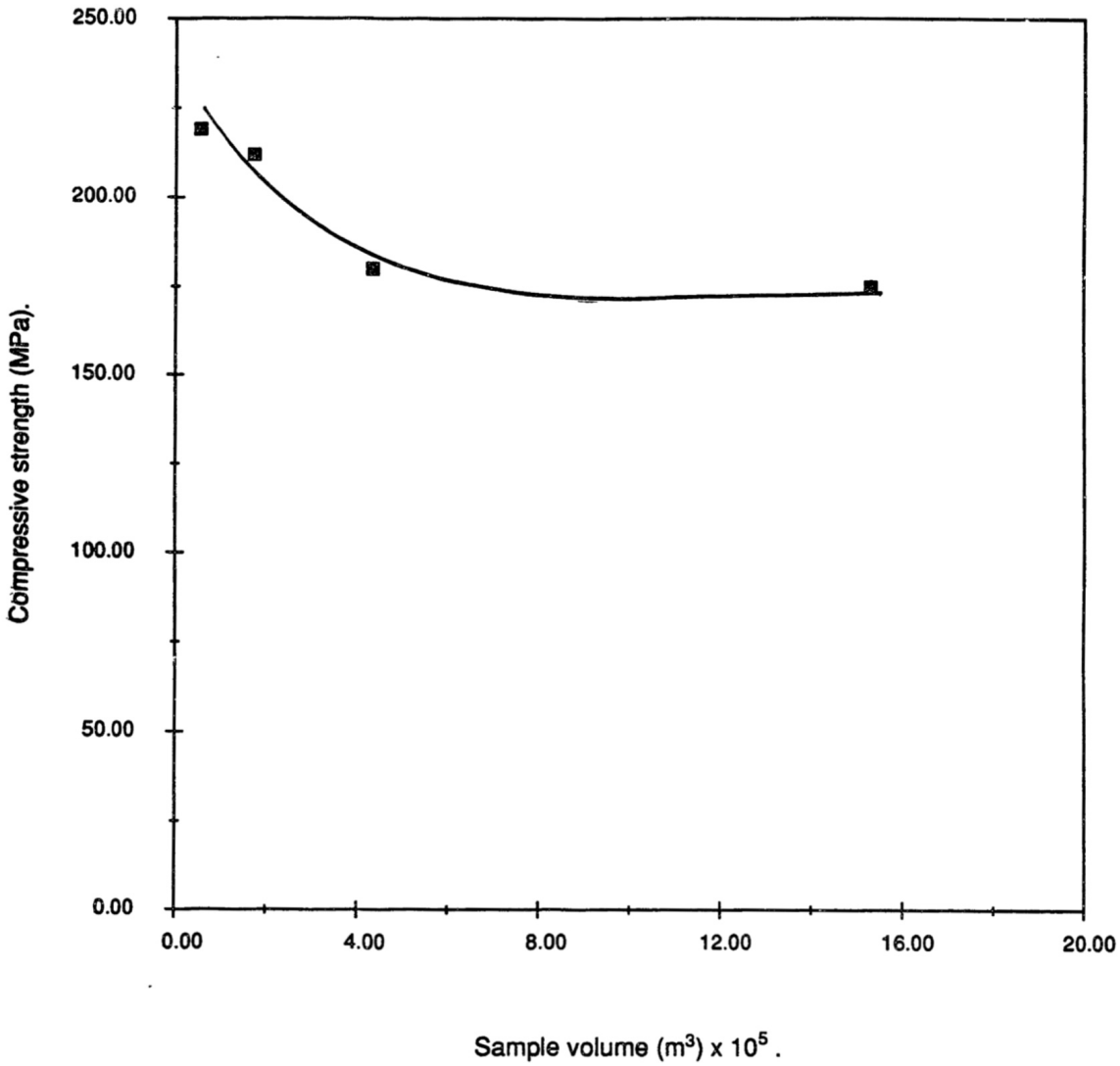

Figure 3.1: Compressive strength of granite versus test sample volume. [38]

3.1.4 Damage Evolution at the Crystal Length Scale

Damage evolution in granite, at the grain scale, occurs at grain interfaces. [69] Damage initiates at the grain boundaries. [70] The microcracks network to create crack surfaces, then a release of strain energy in the cohesive zone initiates a transgranular crack.

Cohesive zone modeling is frequently used to enable crack growth at the grain boundaries. [71] Grains are bonded together by a layer that could have finite initial thickness or no thickness. This layer has elasticity, however it is not a continuum since its volume can go to zero. It behaves more like a spring than a solid. In this context, a crack is a cohesive

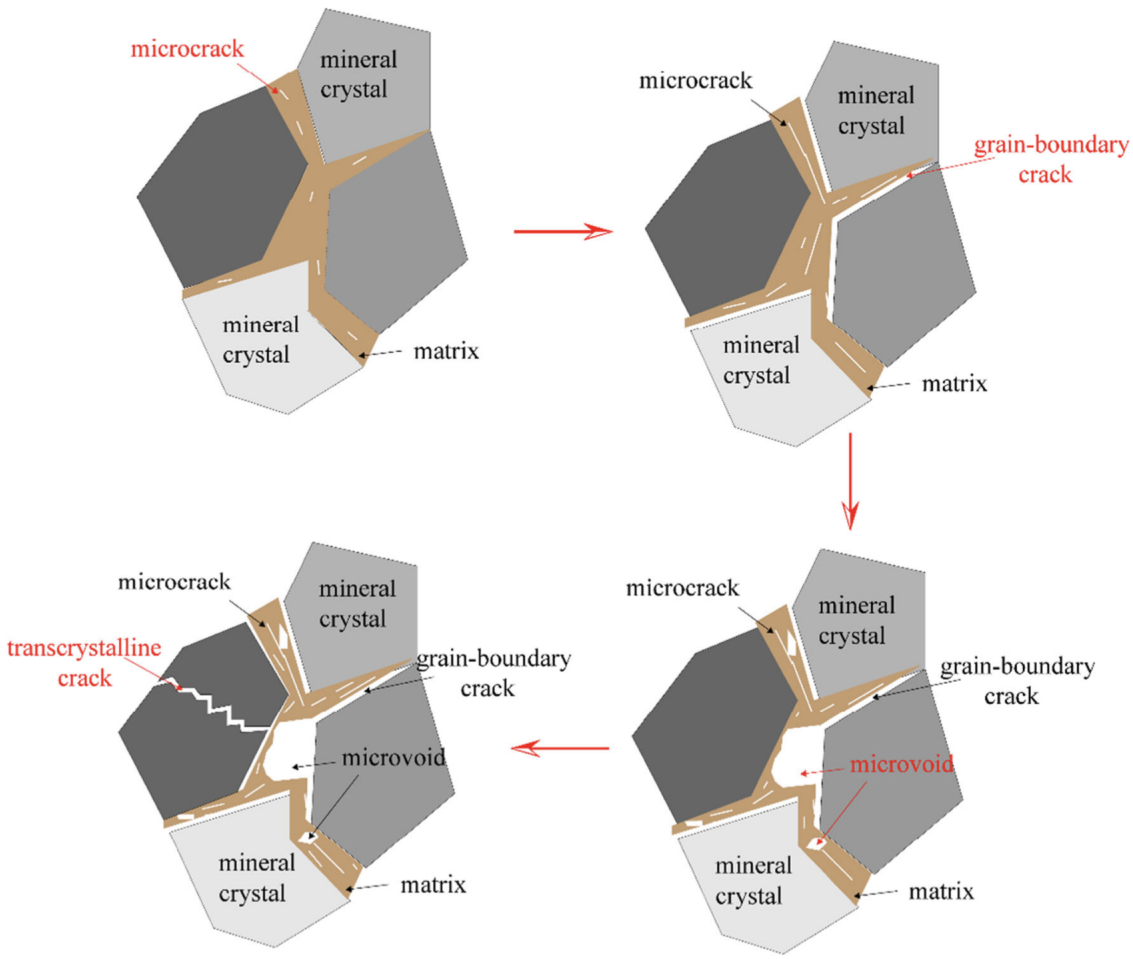

Figure 3.2: Evolution of damage in high-temperature granite. [68]

zone that has gone beyond its yield strength and failed.

The challenge of modeling damage evolution in granite is the transgranular crack. The grain boundaries are known *a priori*, so cohesive zones can be introduced at every grain boundary to cover all possibilities. For a crack to grow through the grain, there are an infinite number of paths it could take. Furthermore, the objective of this model is to predict the recession rate due to spallation rather than the spall size. Transgranular cracks are unnecessary in this model since the objective is to predict recession rates and not spall sizes.

3.2 Thermoelastic Governing Equations

Thermal spallation is a thermomechanical process whereby rapid heating causes existing flaws in the material to expand, coalesce, and free pieces of the material from the surface. As pieces are removed, virgin material is exposed to the heat source and the process continues until either the material is fully spalled or the increased temperature causes a phase change. For example, exceeding the solidus temperature results in melted constituent phases that fill the pre-existing flaws.

3.2.1 Modeling Assumptions

The model of thermal spallation developed based on certain fundamental assumptions. These assumptions are:

1. Zero body forces on the material.
2. Zero internal heat generation.
3. Tractions follow the Cauchy stress principle within grains.
4. Mineral grains are linearly elastic.
5. Uniform material properties within a grain.
6. The tractions at grain boundaries follow a traction-separation law.
7. The temperature jumps at grain boundaries follow a contact conductance law.
8. Damage evolves at grain boundaries only.
9. The material is anhydrous.
10. Uniform heat flux applied.

The first assumption removes body forces from the model. Gravity is a body force that acts on spalling materials, however stress due to gravity is dominated by stress due to confined thermal expansion. For example, a 500 K temperature rise in granite, which has a Young's modulus of approximately 40 GPa and thermal expansion coefficient of 8×10^{-6} K^{-1}, would result in a compressive stress of 160 MPa. With a density of 2.7 g/cc and Earth's surface gravity of 9.81 m/s^2, the pressure due to gravity reaches the same level at a depth of 6 km. Since spallation occurs on the scale of millimeters, neglecting gravity has an insignificant affect on the accuracy of the model. The second assumption removes internal heat generation from the model. In effect, the strain energy of the solid remains strain energy and there is no conversion to thermal energy.

The assumptions of Cauchy stress, linear elasticity, and uniform grain properties are based on the nature of igneous rocks and the length scale of regard. The mineral grains in the rock are fundamentally crystals, organized in a lattice. At the atomic scale, the tractions do not obey the Cauchy stress principle, $t_i = \sigma_{ij} n_j$, as atoms that are not adjacent can still exert forces on each other. Since the length scale of regard is millimeters and the crystal unit cells are on the scale of angstroms, lattice effects can be ignored and the grains can be treated as continuum solids. Linear elasticity is also assumed for these grains because there is an order of magnitude difference in the yield strength of the crystals compared to the grain boundaries. The yield strength of single crystals is on the order of 1 GPa, while for the grain boundaries it is on the order of 0.1 GPa. As the stress rises, grain boundaries will fail first and release the grains as spalls before the grains reach their yield points. Therefore, the assumption of linear elasticity is appropriate for this model because grains will be liberated before yielding. Lastly, uniform properties within a single grain are assumed because voids and dislocations within the grains are small relative to the grain size. These features are present when crystals are studied for their material properties, so their influence on the bulk response of the crystal has already been homogenized into the bulk material properties.

The assumptions of a traction-separation law (TSL) and contact conductance law governing the grain boundaries are common modeling treatments of bonds between materials. [72, 73, 74, 75] Grain boundaries are non-linear and jagged surfaces that can remain partially in contact after a deformation is applied. Instead of directly modeling these surfaces and their contact state, an equivalent planar surface is assumed with a TSL governing the tractions and contact conductance law governing the temperature jumps. In assuming contact conductance, radiation between the two surfaces is ignored. The absolute temperatures are relatively low, for radiation, and similar to each other across grain boundaries. For example at 700 K, a 10 K temperature difference across the boundaries will produce 9 mW/mm^2 of heat flux in conduction and 0.8 mW/mm^2 in radiation. The contact conductance is assumed to be unaffected by damage to the cohesive layer. If the gap opening exceeds the cohesive length, then conductance is deactivated and if the gap closes, then conductance is reactivated. The tractions and temperature jumps across the planar surface need not be uniform. In this work, the parameters of the TSL and contact conductance law are uniform throughout the material because of a lack of data that capture the effects of dissimilar and anisotropic mineral grains with mismatching crystal orientations. This modeling assumption implies that there is no initial distribution of flaws or damage in the material.

In this model, damage is assumed to evolve at grain boundaries only and not through the grains. This assumption contradicts experimental observations of spallation, where spall widths are on the order of 0.1 mm and the grains are several times larger. [31] Crack growth through the grains is not included in the model due to the limits of modern computers. Extended finite element modeling (XFEM) can capture crack growth through a continuous medium, however there can be no interaction with the TSL once a transgranular crack reaches the grain boundary. [76] Another approach would be to introduce cohesive zones within the grains themselves, however this would exponentially increase the number of degrees of freedom in FEM since finer meshing would be required within the grains.

Adding cohesive zones would create finite element models that would be intractable to solve on modern computers. Transgranular damage is not included in this model due to the limitations of modern computers.

The remaining assumptions are that the material is anhydrous and that heat flux is applied uniformly. Pore pressure has a dominant impact on the thermal spallation of concrete, however flaws and voids are dominant for rocks. [32] As such, pore pressure is not included in this model. Uniform heat flux is assumed due to the poor thermal conductivity of rocks. For reference, the conductivity of granite is two orders of magnitude lower than copper. Heat conduction is approximately 1D, into the material, regardless of temperature gradients on the surface of the material. Model results, such as the recession rate, can be applied in cases with non-uniform heat flux because heat flux within the material is relatively weak compared to the applied heat flux. Therefore the majority of the heat flux going into the material, normal to the surface, and very little conducting in the transverse direction. The uniform heat flux results can be applied to non-uniform scenarios due to the poor thermal conductivity of igneous rock.

3.2.2 Equilibrium within the Grains

Thermal Equilibrium

The temperature distribution within the grains is governed by the heat equation, given in Equation 3.1.

$$\frac{\partial}{\partial x_i}\left(k_{ij}\frac{\partial T}{\partial x_j}\right) = \rho C_p \frac{\partial T}{\partial t} \tag{3.1}$$

In the heat equation, x_i are the body coordinates, t is time, $k_i j$ is the thermal conductivity tensor in body coordinates, T is the temperature, ρ is the density, and C_p is the specific heat at constant pressure. While not explicitly stated in Equation 3.1, the material properties of the grain are generally dependent on temperature. For example, quartz crystals

undergo a lattice transition at approximately 850 K that changes the thermal conductivity and density of the grains. Density changes also occur due to thermal expansion, however these volumetric changes are significantly smaller than the observed changes in density.

The thermal conductivity of a mineral is expressed in the literature using a reference frame attached to its crystal lattice, $k_{ij}^{(c)}$. Let Q rotate the body frame into the lattice frame,

$$k_{ij} = Q_{pi} k_{pq}^{(c)} Q_{qj} \tag{3.2}$$

The crystal orientation, Q, is treated as constant in both temperature and time. Crystals of the same mineral, (c), can have different orientations in the body frame. In chapter 5, the crystal orientations are sampled from a uniform random distribution, creating unique properties for each grain. For minerals with significant anisotropy, this can produce stresses on grain boundaries even between grains of the same mineral.

The internal heat generation term is not included in Equation 3.1 due to the modeling assumptions discussed in subsection 3.2.1.

Mechanical Equilibrium within the Grains

To maintain static equilibrium within the grains, the stress distribution must follow Equation 3.3, which states that the divergence of stress is zero. [77]

$$\frac{\partial \sigma_{ij}}{\partial x_j} = 0 \tag{3.3}$$

The body forces are not included in equilibrium due to the assumptions discussed in subsection 3.2.1. The accelerations are also excluded since grains do not undergo significant translations or rotations as their grain boundaries fail. Applying the assumption of linear elasticity from subsection 3.2.1, the stress in the grains is governed by Hooke's law, Equation 3.4.

$$\sigma_{ij} = C_{ijkl}\left[\varepsilon_{kl}^{(t)} - \alpha_{kl}\left(T - T_0\right)\right] \tag{3.4}$$

In Hooke's law, C_{ijkl} is the stiffness tensor, $\varepsilon_{kl}^{(t)}$ is the total strain tensor, α_{kl} is the thermal expansion coefficient tensor, T is the current temperature, and T_0 is the initial temperature. The material properties C_{ijkl} and α_{kl} are both expressed in the body frame, which is a rotation from the crystal lattice frame. The thermal expansion coefficient, α_{kl}, is rotated into the body frame using the same process as Equation 3.2, where Q rotates from body frame to crystal frame.

$$\alpha_{kl} = Q_{pk}\alpha_{pq}^{(c)}Q_{ql} \tag{3.5}$$

$$C_{ijkl} = Q_{mi}Q_{nj}C_{mnpq}^{(c)}Q_{pk}Q_{ql} \tag{3.6}$$

For the stiffness tensor, the rotation process in Equation 3.6 follows the standard tensor rotation operations. In this subsection k represents an index into tensor quantities, whereas in Equation 3.1 it represents the thermal conductivity. Both C_{ijkl} and α_{kl} are generally functions of temperature, though it is not made explicit in Equation 3.4.

The total strain, $\varepsilon_{kl}^{(t)}$, is the infinitesimal strain measure, which is a linearization of the finite strain measures. Infinitesimal strain is assumed since the failure displacements of the cohesive zones are small relative to the size of the grains. This strain measure is given in Equation 3.7, where u_k is the displacement field and x_k are the coordinates in the deformed body frame.

$$\varepsilon_{kl}^{(t)} = \frac{1}{2}\left(\frac{\partial u_k}{\partial x_l} + \frac{\partial u_l}{\partial x_k}\right) \tag{3.7}$$

Substituting Equation 3.7 into Equation 3.4 yields Equation 3.8, which relates the stress state to displacement gradients in the grain. Taking the divergence of Equation 3.8 and

assuming T_0 is uniform for the grain yields Equation 3.9, three partial differential equations (PDEs) that govern the displacement fields within a grain of mineral (c) and rotation Q from the body axes.

$$\sigma_{ij} = C_{ijkl}\left[\frac{1}{2}\left(u_{k,l} + u_{l,k}\right) - \alpha_{kl}\left(T - T_0\right)\right] \tag{3.8}$$

$$Q_{mi}Q_{nj}C^{(c)}_{mnpq}Q_{pk}Q_{ql}\left[\frac{1}{2}\left(u_{k,jl} + u_{l,jk}\right) - Q_{rk}\alpha^{(c)}_{rs}Q_{sl}\frac{\partial T}{\partial x_j}\right] = 0 \tag{3.9}$$

In general, Q is constant while $C^{(c)}_{mnpq}$ and $\alpha^{(c)}_{rs}$ vary with temperature, T. Solutions to Equation 3.9 must satisfy the strain compatibility relationship, given by Equation 3.10, where ϵ is the Levi-Cevita symbol. [77]

$$\epsilon_{ipm}\epsilon_{jqn}\frac{\partial \varepsilon^{(t)}_{mn}}{\partial x_p \partial x_q} = 0 \tag{3.10}$$

3.2.3 Jump Conditions at Grain Boundaries

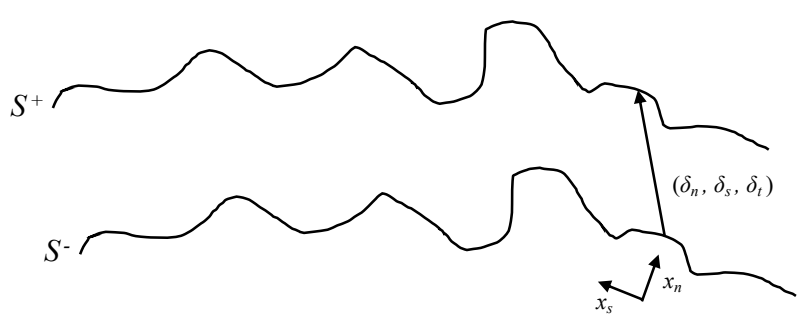

Figure 3.3: Diagram of grain boundary separation.

The temperature (T) and displacement (u) PDEs developed in subsection 3.2.2 apply within each individual grain. At the grain boundaries, illustrated in Figure 3.3, there are jump conditions that relate T and u values on one side of the boundary to those on the other side.

The temperatures are connected through a gap conductance law. Similar to Fourier's

law, the temperature difference across a gap is proportional to the heat flowing through it. Displacements are connected through a traction separation law (TSL). The relative displacement between points that are initially coincident creates a traction/load on the grains. Greater displacement causes a greater load, until the cohesive zone yields. After yielding, the load diminishes to zero. When the two surfaces are compressed together, they experience contact and the cohesive layer is not damaged or altered by contact.

Thermal

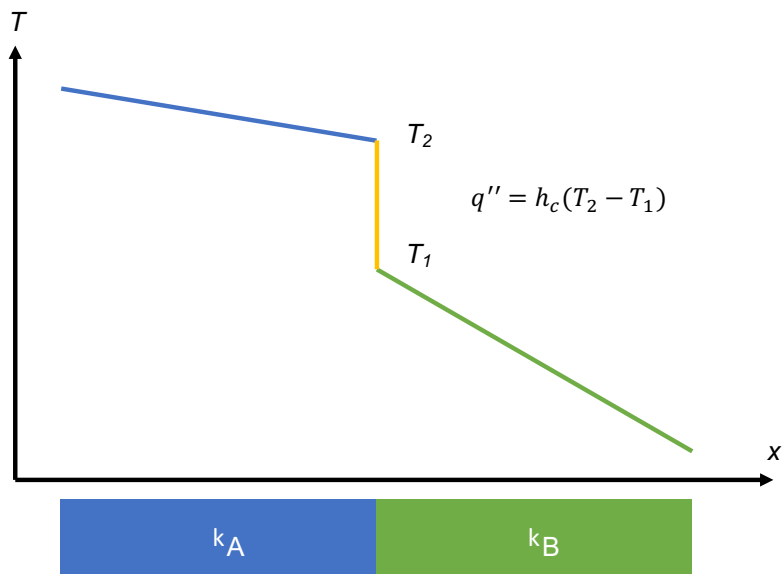

Figure 3.4: Illustration of contact conductance.

Of the three modes of heat transport, conduction and radiation apply to grain boundaries. Following the modeling assumptions in subsection 3.2.1, radiation is ignored because it is an order of magnitude smaller than contact conductance. Thermal conduction occurs across grain boundaries in pure compression and in shear. In tension, however, the thermal contact conductance, h_c, drops to zero as the clearance, δ_n in Figure 3.3, increases. The conductive heat flux from S^+ to S^- is governed by Equation 3.11. [75] Figure 3.4 illustrates the temperature distribution when contact conductance is applied at the interface between two materials. Though not explicit in Equation 3.11, the conductance h_c is a function of the

gap length δ_n. As the contact conductance h_c increases, the surfaces S^+ and S^- approach the same temperature. As it decreases, a temperature jump is created between the surfaces and heat is lost from the system. For geological materials, negligible heat loss occurs at grain boundaries.

$$q_c'' = h_c \left(T^+ - T^-\right) \tag{3.11}$$

Mechanical

The mechanical jump conditions create traction on either side of the grain boundary. The value of this traction follows a TSL, which relates the traction to the separation distance between the two sides of the grain boundary and the damage state of the grain boundary.

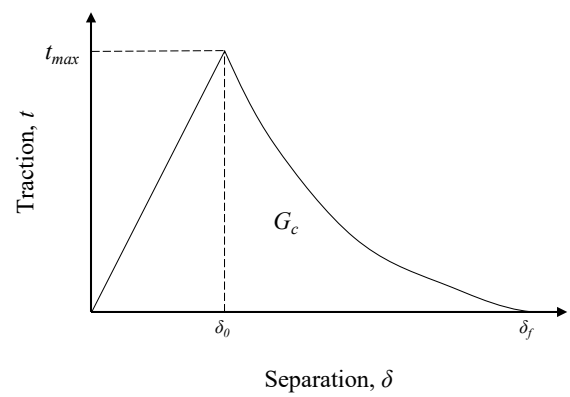

Figure 3.5: General traction-separation law.

A general traction-separation law is shown in Figure 3.5. The traction vector is a linear transformation of the separation vector, $\delta^{(L)}$. This vector is defined by resolving the displacement on the two sides of the boundary into the local frame of the grain boundary, as in Equation 3.12.

$$\delta^{(L)} = \begin{bmatrix} \delta_n \\ \delta_s \\ \delta_t \end{bmatrix} = \begin{bmatrix} u_n \\ u_s \\ u_t \end{bmatrix}^+ - \begin{bmatrix} u_n \\ u_s \\ u_t \end{bmatrix}^- \tag{3.12}$$

Without damage, the traction at this interface is expressed in Equation 3.13. In most cases, the off-diagonal terms are zero and the traction vector components are uncoupled from the terms in the separation vector.

$$\begin{bmatrix} t_n \\ t_s \\ t_t \end{bmatrix} = \begin{bmatrix} E_{nn} & E_{ns} & E_{nt} \\ E_{ns} & E_{ss} & E_{st} \\ E_{nt} & E_{st} & E_{tt} \end{bmatrix} \cdot \begin{bmatrix} \delta_n \\ \delta_s \\ \delta_t \end{bmatrix} \tag{3.13}$$

If the boundary has not been damaged, the traction is given by Equation 3.13. Otherwise, the traction magnitude is given by Equation 3.14, where $\bar{t}$ is the traction computed by Equation 3.13.

$$t_i = (1 - D)\bar{t}_i \tag{3.14}$$

The damage parameter D varies on a scale from 0 to 1, with 1 being total failure of the grain boundary. It is a function of the maximum total separation experienced by the grain boundary, δ_{max}, where total separation is defined in Equation 3.15. Given the maximum total separation, δ_{max}, the damage parameter is defined in Equation 3.16.

$$\delta = \sqrt{\delta_i \delta_i} \tag{3.15}$$

$$D = 1 - \left(\frac{\delta_0}{\delta_{max}}\right)\left(\frac{1}{1 - e^2}\right)\left[1 - e^{2\left(\frac{\delta_f - \delta_{max}}{\delta_f - \delta_0}\right)}\right] \tag{3.16}$$

The separation at damage initiation, δ_0, can be defined by the maximum tractions in each direction, $(t_n^{max}, t_s^{max}, t_t^{max})$. Damage initiation occurs once the condition in Equation 3.17 is true, given the relationship between t and δ in Equation 3.13.

$$\left(\frac{t_n}{t_n^{max}}\right)^2 + \left(\frac{t_s}{t_s^{max}}\right)^2 + \left(\frac{t_t}{t_t^{max}}\right)^2 = 1 \tag{3.17}$$

Additionally the final separation distance, δ_f, can be expressed in terms of the fracture energy, G_c. The integral under the damaged section of the curve in Figure 3.5 is equal to the fracture energy, G_c, of the boundary. Therefore, the final separation distance can be computed directly from Equation 3.18.

$$G_c = \int_{\delta_0}^{\delta_f} t_i d\delta_i \tag{3.18}$$

Initially, there is no separation between the grains. Under compression, the displacements u^+ and u^- are identical. In tension and shear, the separation is defined by Equation 3.12. The resultant traction is linear with separation per Equation 3.13, until the maximum traction condition in Equation 3.17 is reached. In the second stage, damage accumulates according to Equation 3.16 and reduces the magnitude of the traction by Equation 3.14. Damage continues to accumulate until the total work per unit area meets the the fracture energy, at which point the grain boundary has failed entirely. Post-failure, the surface is traction-free on both grains unless contact occurs, at which point the normal displacements are identical.

3.2.4 Boundary, Initial, and Terminal Conditions

Initially, the temperature throughout the material is uniform and there no displacement field or pre-existing strains, shown in Equation 3.19. On the surface where heat is applied, there is a heat flux boundary condition and, optionally, a pressure boundary condition. The pressure would arise from fluid impinging on the surface if the heat flux is due to convection. Radiative heat transfer would not be accompanied by pressure. Let the heat be applied to the x_3^+ surface, the boundary conditions on this surface are given by Equation 3.20. The other sides of the material are adiabatic and constrained against normal displacement, as shown in Equation 3.21. These conditions on the sides create mirror symmetry, which are appropriate for representative volume elements (RVEs) that represent an infinite extent of material. There are two terminal conditions in thermal spallation, given in Equation 3.22.

Either the material melts, ceasing spallation, or all of the unconstrained material has been spalled.

$$T(x_1, x_2, x_3; t = 0) = T_0 \quad ; \quad u_i(x_1, x_2, x_3; t = 0) = 0 \tag{3.19}$$

$$q''(x_1, x_2, x_3 = x_3^+; t) = q_0'' \quad ; \quad p(x_1, x_2, x_3 = x_3^+; t) = p_0 \tag{3.20}$$

$$q''(x_1 = x_1^+, x_2, x_3; t) = u_1(x_1 = x_1^+, x_2, x_3; t) = 0 \tag{3.21a}$$

$$q''(x_1 = x_1^-, x_2, x_3; t) = u_1(x_1 = x_1^-, x_2, x_3; t) = 0 \tag{3.21b}$$

$$q''(x_1, x_2 = x_2^+, x_3; t) = u_2(x_1, x_2 = x_2^+, x_3; t) = 0 \tag{3.21c}$$

$$q''(x_1, x_2 = x_2^-, x_3; t) = u_2(x_1, x_2 = x_2^-, x_3; t) = 0 \tag{3.21d}$$

$$q''(x_1, x_2, x_3 = x_3^-; t) = u_3(x_1, x_2, x_3 = x_3^-; t) = 0 \tag{3.21e}$$

$$V_s = V_{uc} \quad \text{or} \quad T = T_{\mathrm{m}} \tag{3.22}$$

3.2.5 Summary

The thermomechanical model of thermal spallation consists of governing PDEs within the mineral grains, jump conditions between the grains, loads and boundary conditions on the exterior of the material, initial conditions, and terminal conditions. Temperature is governed by the heat equation, Equation 3.1, within the grains and a contact conductance law, Equation 3.11, at the grain boundaries. Displacement is governed by mechanical equilibrium, Equation 3.9, within the grains and a traction separation law, Equation 3.14, at the grain boundaries. For heat flux applied to the $+x_3$ face, symmetry boundary conditions

are imposed on the $\pm x_1$ and $\pm x_2$ faces. The $-x_3$ face is constrained from motion in the x_3 direction and is adiabatic. The initial conditions are uniform initial temperature and no pre-stress or displacement field in the material. The terminal conditions are either all of the material has spalled or the surface temperature reaches the melting point of the material.

3.3 Numerical Solution Process

3.3.1 2D Plane Strain Solution

The model presented above is fully 3D, however modern computers are limited such that a statistically representative volume element would be computationally intractable. The model is instead simplified to 2D plane strain, with 2D heat conduction. The classical plane strain approach is used, rather than generalized plane strain. The plane does not represent a plane of symmetry in a cylindrical material, where mineral grains would be toroidal masses. Fully 3D simulation would affect the results of the model as there are crystal misorientations that cannot be represented in 2D. Future work to realize this model in 3D is discussed in section 6.3.

3.3.2 Staggered One-Way Coupling

General solutions to the system of equations defined in section 3.2 cannot be found analytically, so instead they are computed using direct numerical simulation (DNS). A full 3D simulation of the material is currently infeasible on modern computers due to the need for high mesh density at grain boundaries. A 2D plane strain model is used instead, which is common practice in 2D crack propagation models. [78] The material is discretized into finite elements, with unstructured triangular elements inside the grains and cohesive elements at the grain boundaries. Polygonal elements were considered, however the FEM solver does not support them at this time. [79]

The equations presented in subsection 3.2.2 show that the mechanical PDE is strongly influenced by temperature, but the thermal PDE is weakly influenced by displacement.

Additionally, mechanical wave propagation in igneous rocks is orders of magnitude higher than temperature propagation, so changes in stress occur nearly instantaneously compared to changes in temperature. Staggering the solution of these two equations avoids using an unnecessary quasi-static approach to solving the mechanical equations. Time is advanced through the thermal simulation, then a static mechanical analysis is performed at the end of each thermal step. A Crank-Nicolson scheme advances time in the thermal simulation, while the mechanical analysis is solving $Ku = F$, as in standard FEM. [80]

The simulations are performed by Abaqus, with a Python manager that prepares input files and processes output files from each time step. The flowchart for the manager is shown in Figure 3.6. The two "step" blocks are calls to Abaqus, with the other blocks performed by the manager.

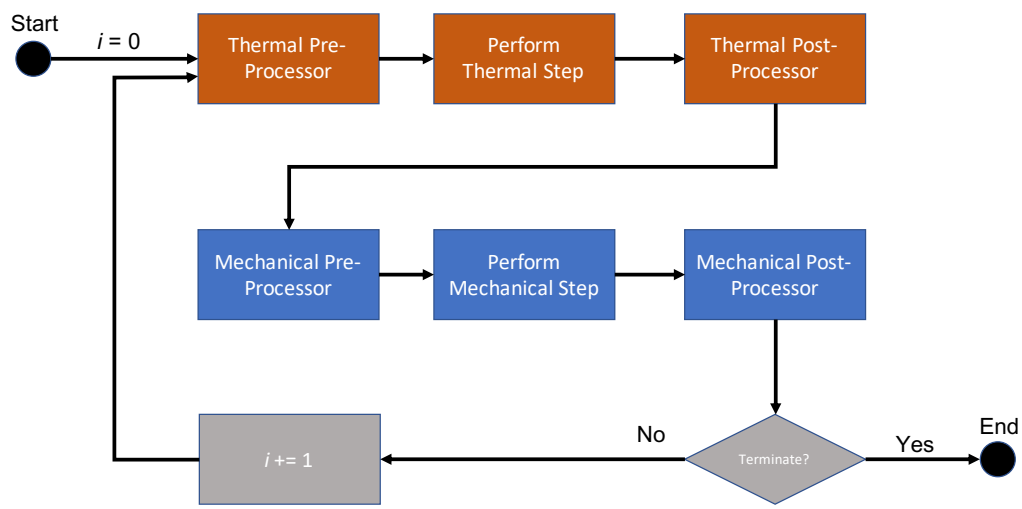

Figure 3.6: Staggered thermomechanical simulation of thermal spallation.

3.3.3 Initialization

At the beginning of the simulation, mesh and job files are created from defined parameters for the run. These parameters include the magnitude of the heat flux, size of the domain, and the properties of the constituent materials. The first step is to run MicroStructPy [81, 82], to create a domain with the same composition and grain size distributions as the material being

simulated. Cohesive elements are inserted between elements at grain interfaces. A material section is created for each grain, and the material orientations of these sections are sampled from a uniform random distribution. To uniformly sample orientations, the components of a quaternion are sampled from the standard normal distribution, Equation 3.23, then the quaternion is normalized to have unit magnitude, Equation 3.24. [83]

$$q' \sim Z + Zi + Zj + Zk \tag{3.23}$$

$$q = \frac{q'}{||q'||} \tag{3.24}$$

An undirected graph of the elements is also generated, which is used in the mechanical post-processing step. Job parameters such as heat flux magnitude and time step size are loaded into template Abaqus input files and all input files in `*INCLUDE` statements are copied to the simulation directory.

3.3.4 Time Advancement in Thermal Analysis

Pre-Processor

The thermal pre-processor updates the thermal mesh and heat flux boundary condition. If it is the first step, $i = 0$, then there are no updates from the initial mesh and boundary conditions. The nodes, elements, and contact pairs in the thermal mesh are updated with the outputs from the $i - 1$ mechanical step. Nodal coordinates are updated with the displacements computed by the mechanical step. Elements are removed from the thermal mesh based on the mechanical post-processor output. If an entire grain is removed, then the contact pairs associated with it are also removed. The thermal job is also updated to reflect changes to the initial and boundary conditions. The initial temperature field of step i is set to the final temperature field of step $i - 1$.

Thermal Step

The thermal step takes the job file created by the thermal pre-processor and runs it with Abaqus. The temperature jump conditions in Equation 3.11 are implemented with a gap conductance interaction between contact pairs. Since the nodal coordinates were updated by the pre-processor, gaps that are sufficiently wide will not conduct heat ($\kappa = 0$). In this model, sufficiently wide means the cohesive element has failed in the normal direction.

The boundary conditions of the thermal model are adiabatic on all sides except the side with an applied heat flux. For example if heat is applied to the $+z$ face of the domain, then the $\pm x$, $\pm y$, and $-z$ faces are all adiabatic. Since many applications are nearly infinite in the $-z$ direction, additional grains must be included in the simulation to avoid numerical artifacts in the simulation results. For granite, this ghost layer should be at least four times the average grain width.

The Crank-Nicolson algorithm is used to advance the temperature states in time. For a 1D mesh with constant mesh size, The temperature at node n is advanced from timestep i to $i+1$ by Equation 3.25, where the central difference operator is defined in Equation 3.26. For grid points on the ends of the mesh, a one-sided finite difference is used instead.

$$k\,\frac{\delta_x^2 T_n^i + \delta_x^2 T_n^{i+1}}{2\left(\Delta x\right)^2} = C_p \rho\,\frac{T_n^{i+1} - T_n^i}{\Delta t} \tag{3.25}$$

$$\delta_x^2 T_n^i = T_{n+1}^i - 2T_n^i + T_{n-1}^i \tag{3.26}$$

Crank-Nicholson is an unconditionally stable, implicit scheme. The temperature gradient term in Equation 3.1 is taken as the average value at steps i and $i+1$. The thermal properties k, ρ, and C_p are each functions of temperature. While they do not change significantly from steps i to $i+1$, Abaqus iterates the solution for time $i+1$ to ensure consistency between the temperatures and material properties.

Post-Processor

After the thermal step is complete, its results are post-processed. The final temperature of each node is reported from the Abaqus ODB file. These final nodal temperatures are used as initial conditions in thermal step $i + 1$ and in the thermal strain for mechanical step i. The post-processor will also repeat the thermal step if an ODB file is not found. If there is an ODB file, the next step is the mechanical pre-processor.

3.3.5 Static Mechanical Analysis with Temperature Change

Mechanical Pre-Processor

Similar to the thermal pre-processor, the mechanical pre-processor updates the mechanical mesh and job file. If $i = 0$, no updates are needed and the initial mesh and job are used in the mechanical step. The job file is updating by creating a `*RESTART` from the $i - 1$ mechanical step. Displacement, stress, and damage fields calculated for step $i - 1$ are loaded as initial conditions for step i. The initial temperature field for the mechanical job is taken from the end of step $i - 1$ and the final temperature field is from the end of step i. These temperatures set the material properties of the grains and their difference results in a thermal strain, $\alpha_{kl}(T - T_0)$. This strain is applied in addition to the strains from the end of step $i - 1$.

Since the mechanical steps use the `*RESTART` option, a new mesh does not need to be created for each step. When spalls are removed from the mesh, `*MODEL CHANGE` steps are included to remove the elements and contact pairs associated with those spalls. An equivalent mesh file is generated by the mechanical pre-processor to keep track of the model changes, for the simulation overall post-processor.

Mechanical Step

The mechanical step is a static finite element analysis that takes place instantaneously, at the end of step i. The domain is traction-free on the surface where heat is applied, and fixed on the other boundaries. For example, the $\pm x$ faces are fixed in x, $\pm y$ faces are fixed in y, and $-z$ face is fixed in z. The only load applied is the ΔT at each node in the mesh, representing the change in temperature from the beginning of step i to the end.

The static finite element procedure solves the linear system of equations $Ku = F$. For a 1D bar with constant properties, the stiffness matrix and force vector are given by Equation 3.27 and Equation 3.28 respectively. Cohesive elements create additional degrees of freedom and force balancing equations compared to Equation 3.27. In this case, additional rows would be inserted into K, with a stiffness E_{nn} instead of E. The value of E_{nn} would follow the damage behavior in Equation 3.14, if the tension in the layer exceeds the yield strength. Iteration on the static analysis is required since the displacement field determines the damage state of the cohesive elements, the damage changes the stiffnesses in matrix K, and that matrix is used to solve for the displacements. Since the simulation uses anisotropic triangular elements instead of 1D bars, the assembled stiffness matrix and force vector have a different shape than Equation 3.27 and Equation 3.28. These equations are provided as a reference for a simplified case.

$$K = \frac{EA}{\Delta x} \begin{bmatrix} 1 & -1 & 0 & \dots & & \\ -1 & 2 & -1 & 0 & \dots & \\ 0 & -1 & 2 & -1 & 0 & \dots \\ & & & \ddots & & \\ & \dots & 0 & -1 & 2 & -1 \\ & & \dots & 0 & -1 & 1 \end{bmatrix} \tag{3.27}$$

$$F = E\alpha\Delta T \begin{Bmatrix} -1 \\ 0 \\ \vdots \\ 0 \\ 1 \end{Bmatrix} \tag{3.28}$$

As in the thermal step, the $-z$ boundary condition is artificial, imposed to limit the domain to a size that is suitable for modern computers. To avoid numerical artifacts in the simulation results, at least four grain widths should be added to the $-z$ side of the domain, in a ghost layer. In the Abaqus implementation of this model, there are cohesive elements and contact pairs at the grain interfaces. the cohesive elements do not enforce contact on their own, so contact is enforced separately with a pressure-overclosure relationship that does not use softening.

If there are spalls to be removed, `*MODEL CHANGE` steps are performed before the static finite element analysis. These steps remove the spalls identified at the end of job $i-1$ before performing the job i static step.

3.3.6 Spall Identification and Removal

The results from the mechanical step are used to determine if a spall has formed and should be removed from the material. First, the cohesive elements with damage $D \geq 0.8$ are removed from an undirected graph of the mesh elements. It may be the case that not all of the cohesive elements surrounding a spall have failed, for example a single element with $D < 0.8$. This is a numerical feature, rather than a realistic one, so an additional step is taken to identify these cohesive elements.

As shown in Figure 3.7, under-damaged cohesive elements are identified by finding the shortest paths between the continuum elements on each side of the fully damaged elements. These shortest paths are computed using the undirected graph, where the vertices

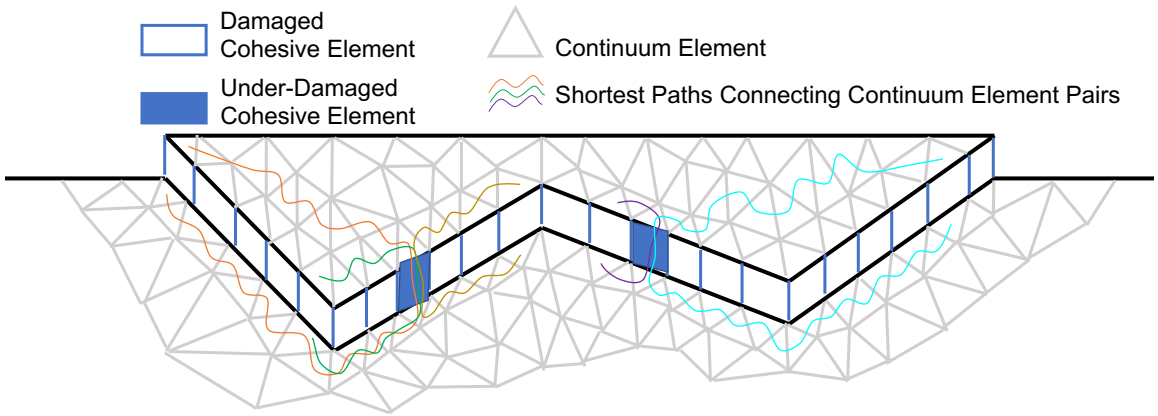

Figure 3.7: Identification of under-damaged cohesive elements using shortest paths.

of the graph are the elements and the edges are weighted by the distances between element centroids. Inspecting Figure 3.7 visually, it is clear which cohesive elements should be removed. The shortest paths approach algorithmically gives the job manager the ability to identify these elements. If the under-damaged cohesive elements represent less than one-third of the total area of cohesive elements removed, then the spall is considered to be *topologically* separated from the main body.

Topological separation is a necessary, but not sufficient, condition for a spall to be removed from the material. For example, if a grain in the middle of the material became topologically separated, then it could not be removed because it is fully surrounded. To be removable, a spall must also satisfy a *geometric* condition. As shown in Figure 3.8a, the surface attached to the removed cohesive elements has a set of normal vectors, n_{1-4}. The mathematical condition that must be true to remove a spall with a given set of normal vectors, N, is that

$$\exists\, u \quad n_i \cdot u \geq 0 \quad \forall\, n_i \in N \tag{3.29}$$

The linear system of inequalities $n_i \cdot u \geq 0$ ensures that the pull direction, u, would not cause the spall to collide with the remaining material at any of its boundaries. From the expressions in Equation 3.29, it is not immediately clear how to test for the existence

of a pull direction, u. An equivalent condition to Equation 3.29 is that u exists if N can be contained by a hemisphere. For a given u, the set of points on that sphere that have a positive dot product with u is a hemisphere. In Figure 3.8b, the normal vectors are all contained in the $+y$ hemisphere, so this spall can be removed. If, however, there were an n_5 that was mostly in the $+x$ direction with a small $-y$ component, the set would still fall within a hemisphere, with a pull direction in the $(+x, +y)$ quadrant. To systematically test for the existence of a pull direction, the convex hull of the set N is taken.

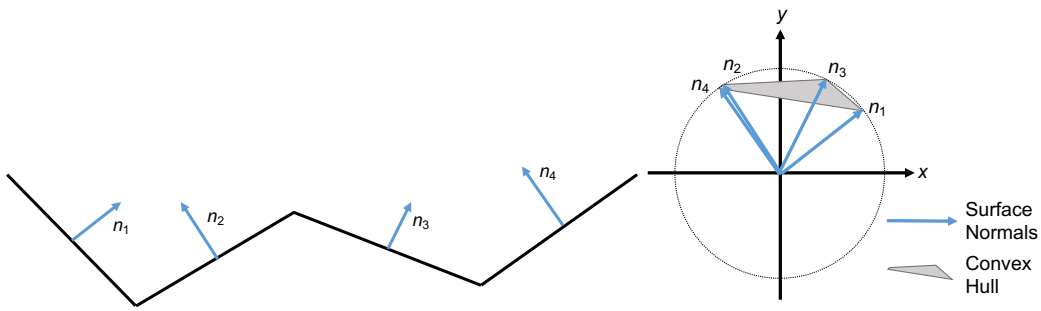

(a) Inward surface normals. (b) Normals and their convex hull.

Figure 3.8: Spall normal vectors and their convex hull.

If the origin is contained within this convex hull, then N spans more than a hemisphere and a pull direction does not exist. On the other hand, if the convex hull does not contain the origin, then the set N spans less than a hemisphere, a pull direction u exists, and the spall is *geometrically* removable. This approach to testing if a spall can be removed is general for any number of dimensions and does not need to be modified for 3D simulations.

For time steps where multiple potential spalls have formed, the geometric conditions are modified if the spalls shared a grain boundary. If the spall in Figure 3.7, for example, had a jagged grain boundary between the two halves, then each half would not have a pull direction. The union of the two halves is removable, but not each half individually. To catch for these cases, the algorithm first tests the unions of neighboring spalls, then tests them individually. If an individual spall is removable, the algorithm iterates to check if other spalls can be removed after that individual has been removed. For example, if the n_2 grain boundary extended to divide the spall in Figure 3.7 into two individuals, initially the

spall on the left would be considered removable and the spall on the right would not. After removing the spall on the left, the spall on the right no longer has that confining surface, so it would be considered removable in the second iteration.

3.3.7 Reapplication of the Heat Flux

The heat flux applied to the top of the domain is updated to reflect the changes in nodal coordinates and element removal. The total heat applied to the domain during each thermal step is held constant, so if a surface element stretches or rotates then the heat applied to it must change. To compute the heat flux on each surface element, it is projected onto the plane perpendicular to the direction of the applied heat flux. For example, if heat is applied in the z-direction, each surface element is projected onto the xy plane. Once projected, the job manager checks for overlapping surface elements, then determines which elements to apply the heat flux to using ray-tracing. This ensures that the total heat flux remains constant, and that heat is only applied to those surfaces that are visible to the heat flux. For flame-jet spallation, heat would be applied wherever the hot gas flows, however an estimate for that flux value would be inaccurate without CFD.

3.3.8 Termination Conditions

After material has been removed from the domain, there is a check to determine if the model should terminate. If the top surface of the domain penetrates the ghost layer, then the model should terminate. This check prevents the domain from becoming small enough that numerical artifacts are introduced into the simulation results. For granite, this ghost layer should be approximately four times the average grain size.

CHAPTER 4
SYNTHETIC MICROSTRUCTURE GENERATION

4.1 Introduction

The numerical solution process described in chapter 3 requires a finite element mesh of the material microstructure. This mesh would need to statistically represent the real microstructure of the material. Creating such a mesh requires the ability to convert textual information about the material, such as volume fractions and grain sizes, into a system of grains. This chapter describes a generic algorithm that creates meshes that are suitable for solving the numerical model in chapter 3.

It is well-established that the macroscopic behavior of a material depends on its features at lower scales, known as the microstructure of the material. [84, 85] For example, the linear elastic response of a material can be approximated by relationships accounting for the volume fraction and individual elastic responses of its constituents. [86, 87, 88, 89] In another example, the effective heat conductivity of a material is generally affected by its average grain size and aspect ratio. [90, 91] A key challenge in mechanics of materials is then to determine this relationship between microstructure and the effective behavior of materials.

Most common approaches to achieve this goal involve homogenization techniques, with varying levels of assumptions and complexity. Many of these methods, such as the Eshelby method for dilute concentrations [86], the Mori-Tanaka method for non-dilute mixtures [89], and classical laminated plate theory [92], are analytical and require a relatively basic characterization of the material. The most dominant methods for arbitrary microstructures and complex behaviors, however, involve direct numerical simulation (DNS) of the microstructure, beginning with the pioneering work of Asaro and Needleman. [93] Since

DNS approaches rely on accurate geometric description of the underlying microstructures, it is critical to both experimentally characterize them and reproduce their geometry for a given representative volume element (RVE).

Microstructure characterization generally involves a variety of techniques, such as measuring grain sizes directly and binning the data [94, 95], analyzing single 2D slices of the material, serial-sectioning electron backscatter diffraction (EBSD), 3D X-ray diffraction (3D-XRD), and X-ray microtomography (X-μCT). [96, 97, 98, 99] These investigations often result in a statistical description of the microstructure, such as composition, grain size distributions, and aspect ratio of the grains. [96] Alternatively, the microstructure can be represented by n-point correlation functions. [85, 100, 101, 102, 103] This work focuses on the creation of synthetic microstructures using the former distributions instead of correlation functions due to greater availability in the community of interest.

Several algorithms convert a microstructure characterization into representative volume element (RVE) meshes suitable for DNS. One family of algorithms solve the inverse problem associated with n-point correlation functions, including global optimization of states in a pixel grid and phase recovery from the fast Fourier transform (FFT). [85, 102] Another family of algorithms rely on dual complexes of the Delaunay triangulation. These algorithms generally generate a triangulation from a set of given seed points, then construct the corresponding dual to generate polygonal (2D) or polyhedral (3D) tessellations representing the grains in the microstructure. Since, in this approach, the seed points of the Delaunay triangulation become grains in the dual tessellation, desired microstructural properties are determined by the seed placement algorithm. Microstructural properties in this approach are also determined by the dual tessellation, which in turn are determined by the choice of dual points in the original triangulation. This dual point can be the circumcenter of the triangle as in a Voronoi diagram, [104] the barycenter as in the barycentric dual, [105] or the power center as in the power diagram, also known as a Voronoi diagram in Laguerre geometry. [106] The seed points can be optimized to fit grain size distributions, [20]

and by introducing Laguerre geometry the grain sphericity distributions can also be recreated. [107] As shown in Figure 4.1b, The Laguerre method produces cells that have similar geometry to their corresponding seeds when the seeds are densely packed. [108]

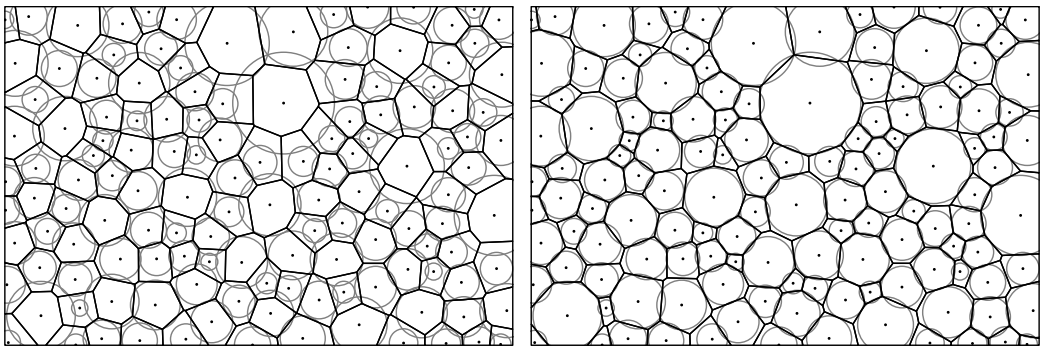

(a) Voronoi tessellation (b) Laguerre-Voronoi tessellation

Figure 4.1: Voronoi and Laguerre-Voronoi tessellations

In this chapter, we introduce a novel method for synthetic microstructure generation from statistical distribution for the size, shape, orientation, and position of multi-phase materials. This method follows a traditional seed generation, placement, and tessellation framework similar to others available in the literature [105, 108, 109, 110, 97, 111, 112, 113, 114], with the addition of several critical improvements. In particular, our method (i) allows for controlled seed overlap to better represent microstructural statistics, (ii) utilizes multi-sphere representation of 3D ellipsoids to account for arbitrarily elongated grains, and (iii) introduces a novel application of the axis aligned bounding box (AABB) tree structure for accelerated seed placement. [115] Primitive geometries are generated according to the size of the domain, the size distributions of each phase, and the volume fractions. These primitives are positioned sequentially in the domain according to multivariate distributions and use the AABB tree to reduce the number of collision checks. Overlapping seed geometries results in a better correlation between seed volume and grain volume, since without overlap the volume of the grain is equal to the volume of its seed plus some of the void between it and neighboring seeds - effectively increasing the average grain size. An extension of the multi-sphere approach for prolate spheroids in [116] and [113] enables direct

modeling of arbitrary ellipsoidal grains. The spheres are converted into cells through Laguerre tessellation [106, 117], followed by quality tetrahedralization [118, 119] to generate unstructured meshes suitable for DNS. Comparing the output distributions from the DNS meshes with the input distributions quantifies the error associated with this microstructure generation algorithm and defines its range of applicability.

This chapter is organized in the following manner. The microstructure generation algorithm is detailed in section 4.2. The performance study in section 4.3 describes a correlation between coefficient of variation in seed volume and the optimal overlap tolerance during seed placement. Example applications are presented in section 4.4, with conclusions and future work in section 4.5. The algorithms in this work are implemented in MicroStructPy, an open source and freely available software package.

4.2 Methodology

As mentioned in the introduction, the proposed method for generating synthetic microstructures generally follows the traditional seed placement and tessellation framework, with the addition of several critical improvements which include the controlled overlap between seeds, a multi-sphere approach for non-spherical grains, and accelerated seed placement using a novel AABB tree. The overall process of this approach is given in Figure 4.2, with each step being described in the following subsections. These steps approximately correspond to the plots shown in Figure 4.3, where Figure 4.3a is the output from Step 2, Figure 4.3b is the output from Step 3, Figure 4.3c is the output from Step 4, Figure 4.3d is a pre-processing step for Step 5, and Figure 4.3e is the output from Step 5. As a final note before proceeding to further develop our method, we must mention that all algorithms described in this work are generic and work identically both in 2 and 3-dimensions. Most figures are shown in 2D for the sake of clarity.

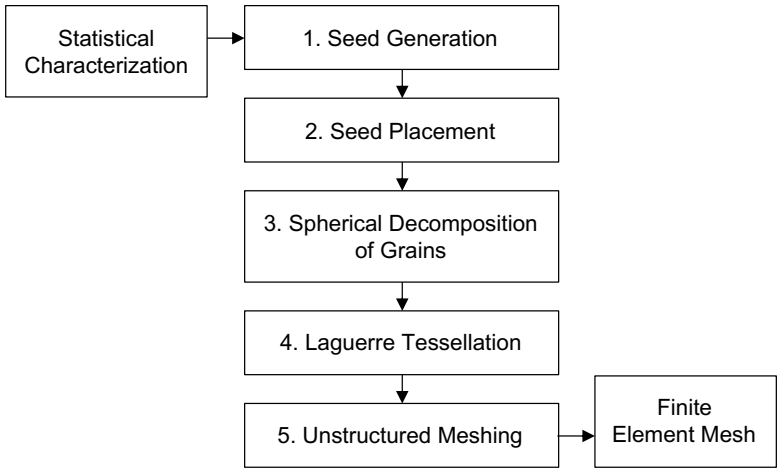

Figure 4.2: Flowchart of the synthetic microstructure generation process.

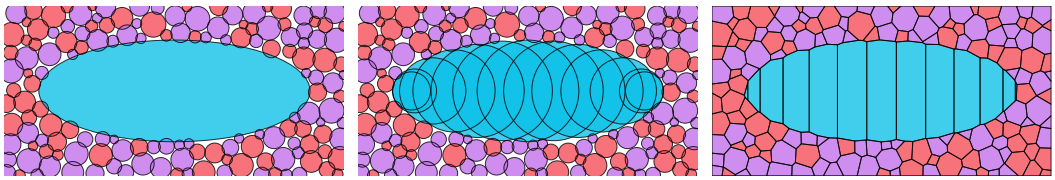

(a) Seed geometries (b) Circular breakdown of seeds (c) Laguerre tessellation

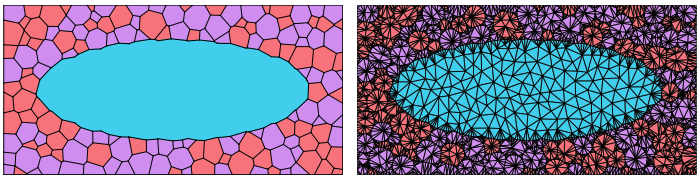

(d) Internal geometry removal (e) Unstructured mesh

Figure 4.3: Steps for converting primitive geometries into an unstructured mesh.

4.2.1 Seed Generation

The first step in our approach is to generate a list of seeds for the microstructure (Step 1, Figure 4.2), where each seed will become a grain in Step 4. The list is created by adding seeds until the total volume of seeds equals the volume of the domain. The phase number, i, of each seed is sampled from a categorical distribution, where the probability of each phase, p_i, is proportional to its number density, n_i. The average number density of phase i is defined as

$$n_i = \frac{V_{f,i}}{\mathbb{E}\left[V_i\right]} \tag{4.1}$$

where $V_{f,i}$ is the volume fraction of phase i and $\mathbb{E}[V_i]$ is the average volume of a seed of phase i. The average number of seeds of phase i per unit volume is n_i. Therefore, the probability p_i that a seed is of phase i, is the number of seeds of that phase divided by the total population of seeds, that is:

$$p_i = \frac{n_i}{\sum_j n_j} \tag{4.2}$$

Once the phase of a seed is determined by weighted sampling, the grain shape distributions associated with that phase are sampled to create a seed. These distributions may include grain size, aspect ratio, and orientation. *This algorithm supports parametric and non-parametric distributions*, though this paper focuses on parametric distributions for the purpose of validation. The volume of this seed is added to the total volume and the process continues until the list volume is greater than or equal to the volume of the domain. The formal seed generation process is given in algorithm 1.

Algorithm 1: Seed generation process

```
Input: domain volume
Input: probabilities for each phase, (p_1, ..., p_k)
Output: list of seeds
X ← categorical random variable s.t. p(X = i) = p_i
list of seeds ← empty list
volume of seeds ← 0
while volume of seeds < domain volume do
    sample x from X
    sample seed from phase x
    add seed to list of seeds
    volume of seeds += seed volume
end
```

4.2.2 Seed Placement

The seed placement step positions a set of seeds within the microstructure domain. Seeds may overlap each other, though a seed may not be entirely contained within another seed. Ensuring an appropriate amount of overlap between seeds requires collision detection be-

tween a seed and its neighbors. In this algorithm, trial positions for a seed are generated, then collision detection is performed to verify appropriate overlap with neighboring seeds. The AABB tree data structure is used to quickly determine which seeds are neighboring, then seeds are decomposed into spheres to check for overlap using the general sphere-sphere overlap detection method. This approach ensures that arbitrarily shaped grains can be placed in the microstructure without complex collision detection schemes. An example output of the seed placement algorithm is given in Figure 4.3a.

Placement Algorithm

Seeds are placed in the domain in descending order by volume, since at the end of the placement step it is easier to find space for smaller grains compared to larger ones. The position of the first seed is determined without collision checks. Seed positions can be specified by *any arbitrary multivariate distribution*, with the default being uniform random throughout the domain. This allows us not only to replicate particle size and shape distributions, but also match their corresponding spatial distribution. For subsequent seeds, a trial position is sampled from the position distribution associated with its phase, then that position is tested for overlap with existing seeds. If the relative overlap between seeds exceeds a prescribed tolerance, then the position distribution is re-sampled until the condition is satisfied. This process continues until all of the seeds have been positioned. Seed overlap is allowed because gaps between the seeds will add their volume to nearby grains, resulting in a mismatch between input and output grain size distributions.

To test if seed i overlaps with seed j, the two seeds are decomposed into spheres as discussed in subsection 4.2.3. Let seed i be decomposed into m spheres and seed j into n spheres. Furthermore, let $\boldsymbol{x}_k$ be the center and r_k the radius of the k-th sphere approximating seed i, while $\boldsymbol{x}_l$ and r_l are the center and radius of the l-th sphere approximating seed

j. Seeds i and j overlap if

$$||\boldsymbol{x}_k - \boldsymbol{x}_l|| + \alpha \min(r_k, r_l) < r_k + r_l \tag{4.3}$$

is true for any $k \in \mathbb{Z}_m$ and $l \in \mathbb{Z}_n$, where $\mathbb{Z}_m$ and $\mathbb{Z}_n$ are the integers from 1 to m and 1 to n, respectively, and the parameter α is the relative overlap tolerance. This tolerance is on the interval [0, 1], where $\alpha = 0$ corresponds to no overlap, and $\alpha = 1$ to an overlap with identical size to that of the smallest seed of the pair currently checked. A sensitivity analysis for α and correlation with variation in grain size is detailed in section 4.3.

As seeds are added to the domain, the number of overlap checks increases. Checking against all of the placed seeds is a brute force approach that does not scale well for large numbers of seeds. To improve the scaling of the overlap detection algorithm, placed seeds are organized into an axis-aligned bounding box (AABB) tree. The overall algorithm for placing seeds in the domain is given in algorithm 2. If the condition on line 16 is checked 10,000 times for a single seed, that seed is removed from the microstructure and execution resumes at line 5. Any empty space left in the domain after seed placement is filled in by tessellating the domain, shown in Figure 4.1 where the seeds are shown in gray and their corresponding grains are shown in black.

AABB Tree Acceleration

An AABB tree is a binary tree data structure that groups boxes that are near each other.[115] It is a special case of the bounding volume hierarchy, where all of the shapes are AABBs and a special case of the R-tree where each node has either zero or two children, to take advantage of binary tree search algorithms. An example AABB tree is shown in Figure 4.4.

In the context of seed placement, the AABB tree accelerates the placement algorithm by reducing the number of overlap checks. Each seed, regardless of its geometry, is fully contained withing an AABB and, consequently, if two seeds overlap then their AABBs

Algorithm 2: Seed placement process

```
Input: pre-placement seeds
Input: position distributions for each phase, (X_1, ..., X_k)
Output: placed seeds
c_v ← seed volume standard deviation / volume mean
α ← correlation from Equation 4.14 or Equation 4.15
sort seeds largest to smallest by volume
placed seeds ← empty list
for seed ∈ pre-placement seeds do
    i ← phase of seed
    repeat
        sample x from X_i
        place seed at x
        candidates ← seeds that may overlap with seed
        clears ← True
        for candidate seed ∈ candidates do
            check for overlap with seed using Equation 4.3
            clears &= seeds do not overlap
        end
    until clears;
    add seed to list of placed seeds
end
```

would also overlap. Seeds are added to the domain incrementally, so the next seed to be placed must not satisfy Equation 4.3 with any of the existing seeds. If seed i is the seed to be placed, the indices of j to test for overlap are 1 to $i - 1$. Testing all seeds from 1 to $i - 1$ is a brute force approach and is computationally wasteful if seeds i and j are not in the same part of the domain. For example, if the seed is in the left half of Figure 4.4b, it is clear that the seed will not overlap with seeds 2, 4, 7, or 9. Those seeds are on the right branch of the tree in Figure 4.4a, so testing for overlap with the right side bounding box has replaced four overlap checks with one check. Checking for overlap between AABBs is a matter of checking whether any of the limits of the two AABBs do not overlap. For 2D AABBs, if any of the inequalities in Equation 4.4 are true, where l and u denote lower and

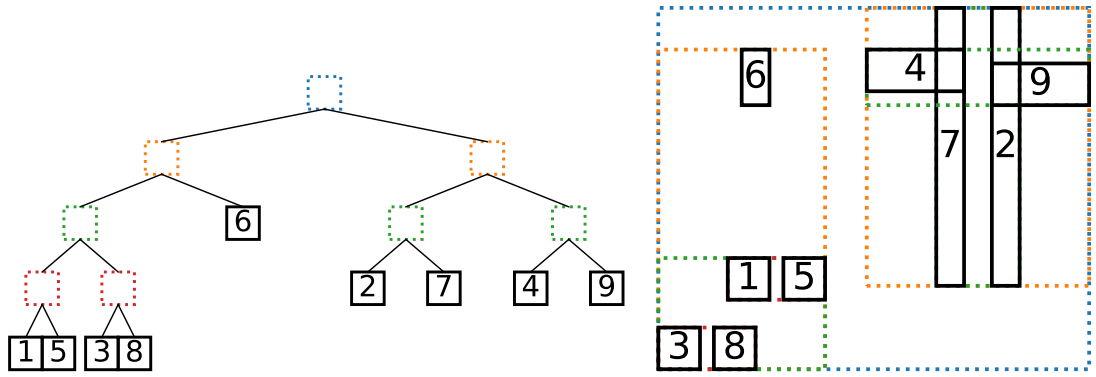

(a) AABB tree

(b) Spatial distribution of AABBs

Figure 4.4: AABBs organized in a tree and their positions in space, with AABBs numbered by insertion order.

upper bounds respectively, then there is no overlap between AABBs i and j.

$$\begin{aligned} x_l^{(i)} &> x_u^{(j)} \qquad & x_u^{(i)} &< x_l^{(j)} \\ y_l^{(i)} &> y_u^{(j)} \qquad & y_u^{(i)} &< y_l^{(j)} \end{aligned} \tag{4.4}$$

In terms of growth rate, the brute force method grows with $\mathcal{O}(n)$, while the AABB tree method is bounded between $\mathcal{O}(n)$ and $\mathcal{O}(\log n)$, depending on how well-balanced the tree is. The tree in Figure 4.4a is well-balanced since its depth, 4, is close to its theoretical minimum depth, $\log_2 9$. Careful updating of the AABB tree as seeds are positioned in the domain can keep the tree well-balanced and eliminate unnecessary overlap checks.

There are three different techniques for creating an AABB tree: top down, bottom up, and incremental insertion. The top down method divides the AABBs into two large groups, then subdivides each of those groups into two smaller groups and recurses until the AABBs have been isolated. The bottom up method groups AABBs into pairs, then groups pairs together, and recurses until there is one large group. The incremental insertion method updates the tree as AABBs are added sequentially. Both top down and bottom up methods are considered "offline" methods, since all of the object positions are determined before the tree is built. The incremental insertion method is an "online" method, which is

ideal for situations where the tree is used to inform the positions of subsequent objects.

The standard insertion method assigns costs to three different options at each node in the tree: 1) add the AABB to the left child, 2) add it to the right child, or 3) create a new parent. The first two options are straightforward, though it should be noted that the terms "left" and "right" are arbitrary and have no connection to physical space. The third option is to demote the parent node to a child, then create a new parent which bounds the AABBs of the new children. For example, if there are two seeds in the domain, there are AABBs surrounding each seed and those AABBs are children to a parent AABB that bounds both seeds. When a third seed is added, the three options are 1) group seeds 1 and 3 and put seed 2 on a separate branch, 2) group seeds 2 and 3 and put seed 1 on a separate branch, and 3) keep seeds 1 and 2 in a group and put seed 3 on a separate branch. The first two options are better if seed 3 is closer to seeds 1 or 2, respectively, while the third option is better if seed 3 is further from seeds 1 and 2. The costs assigned to each of these options should reflect this intuition, and include general best practices for binary trees such as minimizing the depth of the tree. If the best option does not have the lowest cost, the tree will contain more overlapping AABBs and testing for overlap will require a greater number of checks.

For example, methods developed for ray-tracing graphics, a common application of AABB trees, estimate these costs based on the surface area of the bounding box, since the surfaces of objects in a scene are reflecting light. Applying these cost functions to seed placement, however, yields significantly imbalanced trees with bounding boxes that do not contain AABBs in close proximity. Thus, in this work we propose to adopt the volume cost model given by Equation 4.6-Equation 4.8 in order to yield balanced AABB trees for microstructure generation.

The objective of this cost model is to minimize the overlap volume between siblings and minimize the sum of all bounding volume. For the example above, if seeds 1 and 3 are closer to each other than they are to seed 2, then the volume bounding them will be smaller than if seeds 1 and 2 or 3 and 2 were grouped together. Similarly, if seed 3 is between

seeds 1 and 2, keeping 1 and 2 together would result in an undesirable overlap with seed 3. As the AABB descends the tree during insertion, the algorithm chooses the option that minimizes the sum of the overlapping volume and bounding volume costs. Let p denote the parent AABB, l denote the left child, r denote the right child, and x denote the AABB to be inserted. The cost functions therefore are:

$$C(\text{min push down}) = V(p \cup x) - V(p) \tag{4.5}$$

$$C(\text{left}) = C(\text{min push down}) + V(l \cup x) - V(l) + V((l \cup x) \cap r) \tag{4.6}$$

$$C(\text{right}) = C(\text{min push down}) + V(r \cup x) - V(r) + V(l \cap (r \cup x)) \tag{4.7}$$

$$C(\text{new parent}) = V(p \cup x) + V(p \cap x) \tag{4.8}$$

The push down cost is the change in volume of the parent. The cost of choosing the left branch is the push down cost plus the change in the left branch volume plus the sibling overlap volume. The cost of choosing the right branch is mirror symmetric to the left branch cost. Finally, the cost of creating a new parent is the volume of the new parent plus the overlap between the previous parent and the new node. If a child node is chosen but it is not a leaf node then the same process is repeated, which guarantees that each node has either zero or two children.

The performance improvement using an AABB tree over brute force overlap checking is shown in Figure 4.5. The data plotted are walltimes to position seeds in a cube domain, where the seeds are spherical and have lognormally distributed volumes with a coefficient of variation of 1.8, a typical value for crystalline microstructures. [108] The domain has unit edge length and the mean grain volume is set to target a given number of grains. The walltime values were generated on a laptop computer with a 2.9 GHz Intel® Core™ i9 processor and 32 GB of memory. Brute force searching for overlap is significantly slower than using an AABB tree towards the end of the seed placement process. The hierarchi-

cal nature of the tree reduces the number of overlap checks, as approximately half of the existing seeds are eliminated each time the algorithm descends the tree. Overall, a brute force algorithm grows at approximately $\mathcal{O}(n^{2.5})$, while the AABB tree algorithm grows at approximately $\mathcal{O}(n^{1.9})$. From the figure we can see that, for a case with 10,000 seeds, this translates into an improvement of two orders of magnitude: a generation that takes over one day and 3 hours using the brute force approach is completed in under 17 minutes using our AABB tree method.

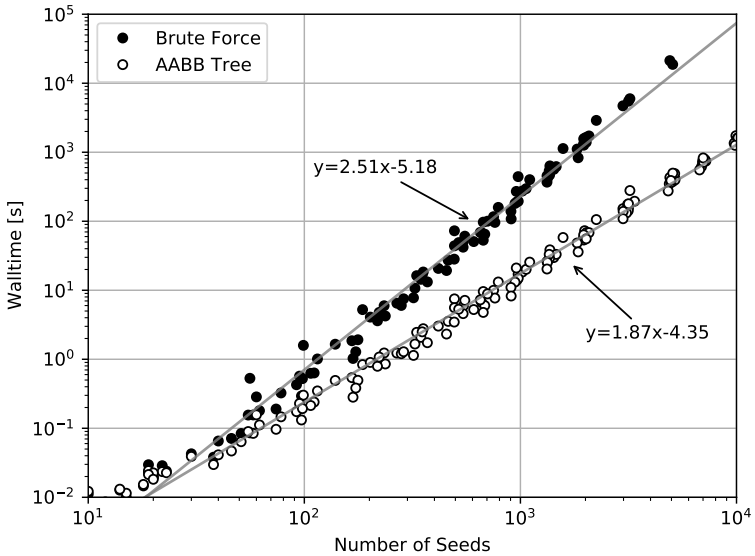

Figure 4.5: Walltime improvement using an AABB tree.

4.2.3 Spherical Decomposition of Grains

Once the seeds are placed in the domain, they are decomposed into sets of spheres (circles in 2D). This decomposition step is necessary because the Laguerre tessellation in Step 4 operates on a set of spheres, not on arbitrary geometries. Elliptical seeds in 2D are decomposed into circles that are tangent to the ellipse, following the algorithm in Ilin and Bernacki. [113] An example of their circular decomposition algorithm is given in Figure 4.3b. In this work, we extend this method to the general 3D ellipsoid in a similar manner, where cross sections of the ellipsoid are decomposed into circles which are promoted

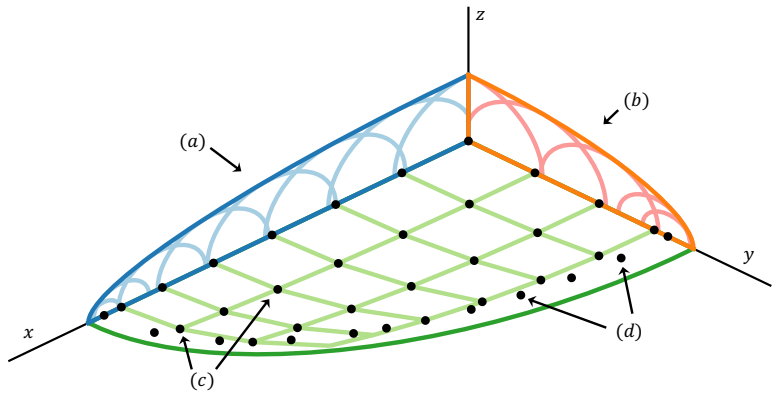

Figure 4.6: Multi-sphere centers for an ellipsoid with axes $a = 5$, $b = 3$, $c = 1$, and parameter $x_1 = 0.9$. (a) Multi-circle approximation of the xz plane, (b) Multi-circle approximation of the yz plane, (c) Grid of non-terminal circle centers, (d) Centers of spheres tangent at the xy plane.

into spheres. Our approach is explained in details in the paragraphs below.

Let us consider an ellipsoidal grain as the one depicted in Figure 4.6, where the centers of the spheres of the corresponding decomposition are shown for the first quadrant only for purposes of clarity. Let the ellipsoid have semi-axes (a, b, c) such that $a \geq b \geq c$. As shown in (a) and (b) of Figure 4.6, the elliptical cross sections in the xz and yz planes are decomposed into circles according to the algorithm in [113]. The terminal circles, which are tangent to the ellipse at the x axis, are removed from the output and will be replaced with a 3D equivalent. The centers of these cross section circles lie on the x and y axes and are gridded to create (x, y) pairs for the centers of the spheres. This grid is rectangular and some of the grid points lie outside the xy cross section of the ellipsoid. A mapping, given below, is applied to these grid points to ensure that they are all contained within the xy cross section of the ellipsoid.

$$(x', y') = \left(x\sqrt{1 - \frac{1}{2}\left(\frac{y}{b}\right)^2},\ y\sqrt{1 - \frac{1}{2}\left(\frac{x}{a}\right)^2} \right) \tag{4.9}$$

The resultant, mapped, grid are the points (c) in Figure 4.6. Once the sphere centers are mapped, their radii are determined to be the distance to the ellipsoid. If the grid creates a sphere that is tangent to the ellipsoid at the xy plane, i.e. the solid green equator in

Figure 4.6, then that sphere is removed and replaced. The replacement spheres, (d), are generated by uniform sampling points at the equator and computing the radius of curvature at each point. Since curvature is a tensor for surfaces, radius of curvature in this case refers to curvature in the z direction, perpendicular to the xy plane. The sphere associated with an equatorial point has a radius equal to the radius of curvature, and a center that is displaced from the equatorial point by one radius length and in the direction normal to the equator.

For prolate ellipsoids, where $a > b = c$, this method yields the same results as Markauskas et al. [116] By gridding the xy plane and careful treatment of the ellipsoid boundary, the multi-sphere method can be applied to general ellipsoids. Manufacturing processes, such as cold-drawing [120], can create ellipsoidal grains in a microstructure that are impossible to represent with a single seed sphere in tessellation-based synthetic microstrtuctures. Multi-sphere approximation improves tessellation-based synthetic microstructure generation by faithfully reproducing anisotropic grains, which are commonly ellipsoidal in geometry.

4.2.4 Laguerre Tessellation

We now use the spheres generated in the previous step as seeds for a Laguerre tessellation, also known as Voronoi power diagrams [106], to generate the geometry of the grains. After this step, all overlaps and voids from the seed generation phase will be eliminated. The Laguerre tessellation is a generalization of the Voronoi diagram, where the seed points are weighted. Examples of the Voronoi diagram and Laguerre tessellation are given in Figure 4.1. Let $\text{pow}(\boldsymbol{p}, s)$ be the power distance between the point $\boldsymbol{p}$ and the sphere s, which has radius r and center $\boldsymbol{c}$. Note that, in this context, pow is a distance measure between a point and a sphere and should not be confused with exponentiation. The power distance is defined by Equation 4.10, where $||\boldsymbol{p} - \boldsymbol{c}||$ is the Euclidean distance between points $\boldsymbol{p}$ and $\boldsymbol{c}$. The region of space associated with each seed $s \in S$ is given by Equation 4.11.

$$\text{pow}(\boldsymbol{p}, s) = ||\boldsymbol{p} - \boldsymbol{c}||^2 - r^2 \tag{4.10}$$

$$R(s) = \{\boldsymbol{p} \mid \text{pow}(\boldsymbol{p}, s) < \text{pow}(\boldsymbol{p}, t) \quad \forall\, t \in S - \{s\}\} \tag{4.11}$$

Voronoi diagrams are a subset of Laguerre tessellations, where r is constant for all seeds $s \in S$. A unique feature of Laguerre tessellations is that $R(s)$ may be empty, depending on the weight and distance to nearby spheres. For example, a sphere contained entirely within another sphere will have an empty cell. In general, spheres that are not entirely overlapped by other spheres will always have a non-empty cell, since $\exists x.\text{pow}(x, s) < 0 < \text{pow}(x, t)$.

The Laguerre tessellation is constrained to the domain of the microstructure. Seeds on the boundary of the domain are clipped and the clipped volume is re-distributed to the interior of the domain. The influence of this clipped volume on the output mesh statistics, such as volume fractions and grain size distributions, depends on the size of the domain. A domain that is relatively large, compared to the size of the grains, has a sufficient number of interior grains to minimize the impact of clipped volume on output mesh statistics. Since RVEs, by definition, require a sufficient number of seeds to be statistically representative, the clipped volume does not significantly impact output mesh statistics.

4.2.5 Unstructured Meshing

The polygonal mesh is converted into an unstructured mesh using Triangle in 2D and TetGen in 3D. [118, 119] Before meshing, facets between cells of the same grain are removed to prevent unnecessary internal geometry, as shown in Figure 4.3c and Figure 4.3d. Additionally, facets between cells of the same phase are also removed if that phase is considered amorphous (e.g., matrix material in a composite) or homogeneous (e.g., a single crystal). The facets between grains of the same phase in Figure 4.3c are not removed because these grains could have different crystallographic orientations or a cohesive interface. Quality of

the unstructured mesh can be controlled by specifying the maximum cell volume and the minimum interior angle. In 2D, additional points can be inserted along grain boundaries for additional resolution at grain boundaries. The mesh shown in Figure 4.3e, for example, was generated with maximum edge length, maximum cell volume, and minimum interior angle quality controls. Figure 4.3e also shows the ellipse internal geometry in Figure 4.3c does not appear in the final mesh.

4.3 Error-Minimizing Seed Overlap Tolerance

Introducing overlap of the seeds improves the correlation between seed volume and grain volume. Seed geometries, such as spheres, cannot completely cover the volume of the domain, which leads to voids between the seeds. Tessellation will assign the volume of these voids to nearby seeds, causing an increase in the volume of the grain relative to the volume of the seed. Overlap between seeds is introduced to counteract the volume increase, as a seed will lose the volume that lies within a neighboring grain. By carefully choosing the amount of overlap, volume increases due to voids are balanced by volume decreases due to overlap and the resulting mesh more accurately represents prescribed grain size distributions.

The seed placement algorithm in subsection 4.2.2 allows for overlap between grains, relative to the the radius of the smaller grain. The allowable overlap is defined by the previously introduced parameter α. As a consequence, for a given microstructure, the error between a desired grain volume distribution and the output volume distribution generated by our algorithm depends on the value of α. In this section, the error-minimizing tolerance is determined for hundreds of lognormal grain volume distributions. Trends between the coefficient of variation in grain volume and optimal tolerance α are characterized empirically and results are extended beyond lognormal volume distributions. The results for several example applications are given in section 4.4 and show good agreement in 2D and 3D for microstructures with multiple phases and unique grain size distributions.

4.3.1 2D

Agreement between the input seed volume distribution and output grain volume distribution generated by our method depends on the overlap tolerance α. For a single volume distribution, α can be tuned to minimize the error between the input and output distributions. In the following, multiple input distributions are accounted for via a parametric study, and results are utilized to find the optimal value of α for each distribution, to finally develop a functional relation between the coefficient of variation, c_v, in grain volume and the corresponding error-minimizing value of α. The volume c_v was chosen as the input quantity since it is the non-dimensional standard deviation. This study first considers 2D microstructures with log-normal distribution in area,

$$A \sim e^{\mu+\sigma Z} \tag{4.12}$$

where the grain area, A, is non-dimensionalized by the area of the unit cell. The parameters μ and σ are the mean and standard deviation, respectively, of the exponent while Z is the standard normal. This study swept the parameters μ and σ, the overlap tolerance α, and the random number generator (RNG) seed on the ranges defined in Table 4.1.

Table 4.1: 2D Overlap Tolerance Design of Experiments

Parameter	Min	Max	Resolution
μ	-10	-7	0.125
σ	0	3	0.125
α	0	1	0.05
RNG seed	0	4	1

The maximum likelihood estimators, $\hat{\mu}$ and $\hat{\sigma}$ are computed for each of the 65,625 combinations of these parameters, with the primary figure of merit being the sum-squared error:

$$r^2 = (\mu - \hat{\mu})^2 + (\sigma - \hat{\sigma})^2 \tag{4.13}$$

The values of α that minimize the median r^2 value across all RNG seeds are shown in Figure 4.7. The tuning sweep for one particular (μ, σ) pair is shown in Figure 4.8.

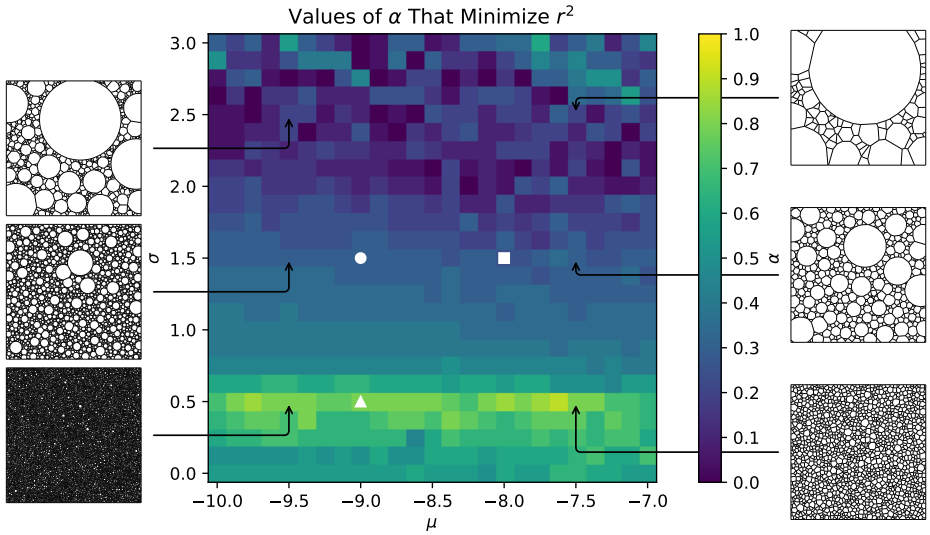

Figure 4.7: Values of α that minimize r^2, shown with example microstructures.

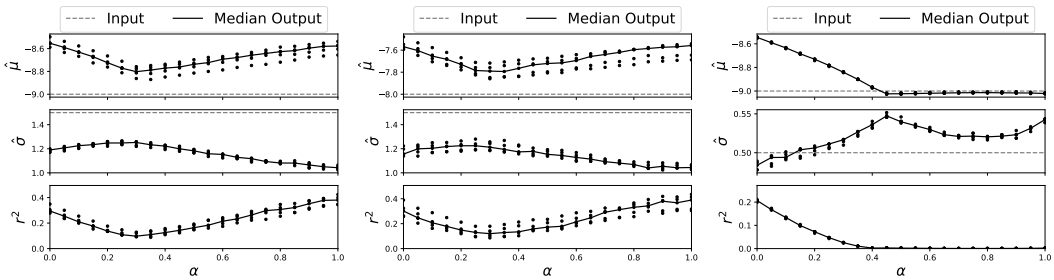

(a) $\circ : \mu = -9, \sigma = 1.5$ (b) $\square : \mu = -8, \sigma = 1.5$ (c) $\triangle : \mu = -9, \sigma = 0.5$

Figure 4.8: Tuning α for three sets of (μ, σ), where each point at an α station corresponds to a unique RNG seed.

The data in Figure 4.7 indicate that optimizing values of α are independent of the parameter μ. Median grain size, e^{μ}, influences the total number of grains, but optimal α values are primarily a function of σ. This μ-independence is confirmed in Figure 4.8a and Figure 4.8b, which have different μ and the same σ. The input and output grain area distributions for four values of α from Figure 4.8c are shown in Figure 4.9.

Given that the error-minimizing α depends on σ, these results can be extended to other distributions by considering the coefficient of variation, c_v, of the grain areas, which is

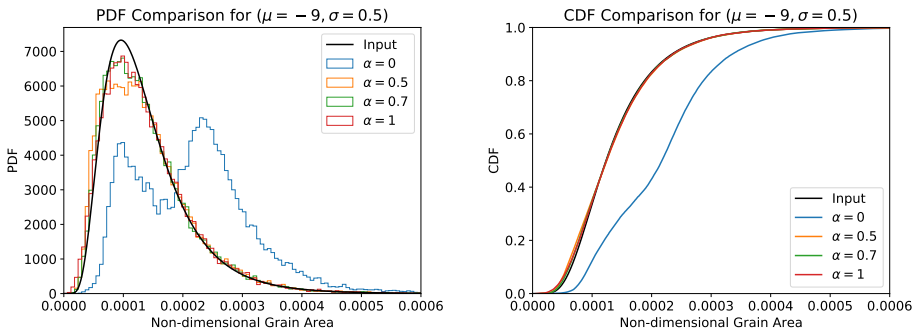

(a) Probability density function (b) Cumulative distribution function

Figure 4.9: Comparison of grain area distributions for $(\mu = -9, \sigma = 0.5)$

related to σ through $c_v = \sqrt{e^{\sigma^2} - 1}$. Collapsing the results of Figure 4.7 and mapping σ to c_v yields the relationship between α and c_v in Figure 4.10.

The kernel of the fit between c_v and α should not diverge to $\pm\infty$ as c_v increases and it should capture the local maximum at $c_v \approx 0.5$. A polynomial cannot satisfy the first criterion, so a rational polynomial was chosen instead. The second order rational polynomial captures the local maximum without overfitting to the data. The least-squares rational polynomial fit to the average α value is given by:

$$\alpha = \frac{0.182c_v^2 - 0.0135c_v + 0.198}{c_v^2 - 0.613c_v + 0.390} \tag{4.14}$$

Choosing α using this trend with the c_v in seed area results in seeds with minimal error between the input and output area distributions. For example, in Figure 4.9 the parameter $\sigma = 0.5$ corresponds to $c_v = 0.53$ and Equation 4.14 yields $\alpha = 0.70$. Using the relationship in Equation 4.14 to determine the overlap limit between seeds, the coefficient of variation of the seed area distribution is compared against that of the grains in Figure 4.11a.

4.3.2 3D

For the 3D case, the same design of experiments as in 2D is used except the parameter μ is held fixed at -10. The correlation was discovered to be invariant of μ in that study, so

the smaller value in that range was selected. Performing the same analysis results in the correlation trend show in Figure 4.10. The least-squares rational polynomial fit is given by:

$$\alpha = \frac{0.457c_v^2 - 0.575c_v + 0.253}{c_v^2 - 1.07c_v + 0.419} \tag{4.15}$$

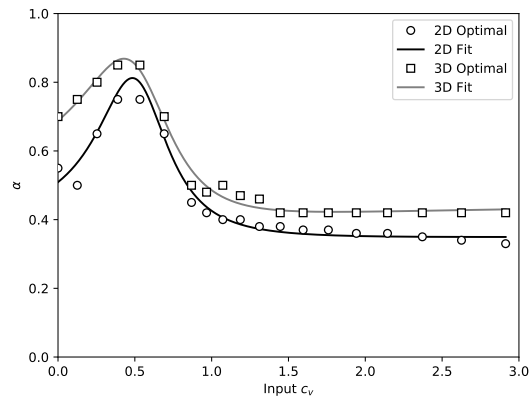

Figure 4.10: Values of α that minimize r^2 for various coefficients of variation.

Since results are available for dense packing of spheres without overlap [108], they provide a basis of comparison for this algorithm. Shown in Figure 4.11b is a comparison of the input and and output coefficients of variation for the seed and grain volumes, respectively. Allowing the seeds to overlap according to the condition in Equation 4.3, using a value of α determine by Equation 4.14 in 2D or Equation 4.15 in 3D, enables improved agreement between seed and grain coefficients of variation.

4.4 Examples of Application

Four example applications for this algorithm are given below. The first microstructure is a 2-phase polycrystal in 2D, with unique grain size distributions for each phase. The second contains ellipsoidal voids in 3D, where the void width is held constant and the aspect ratios are distributed. The third example is a 3-phase polycrystal with elliptical grains that are packed into a non-rectangular domain. Finally, the fourth example is a 2-phase polycrystal in 3D with unique log-normal grain sizes for each phase. Each of these examples use

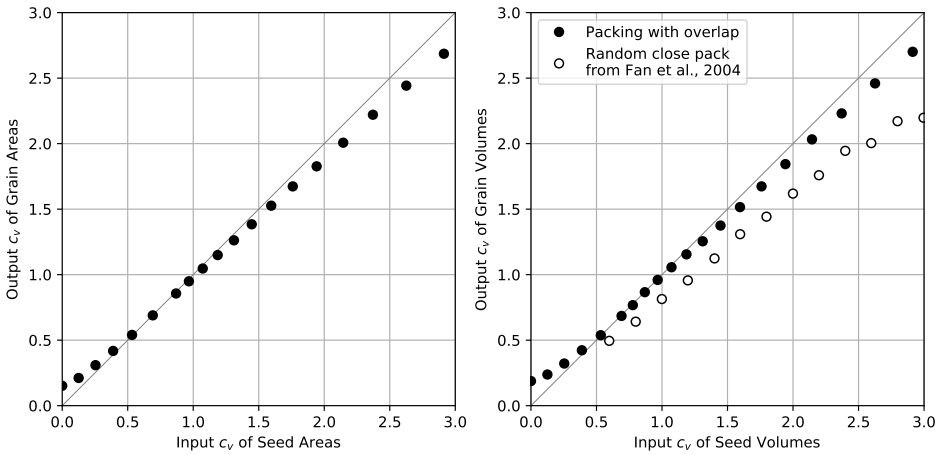

(a) 2D (b) 3D

Figure 4.11: Comparison of input and output coefficients of variation.

parametric distributions for the purpose of validation, however the algorithm also supports non-parametric distributions.

4.4.1 Two Phase Composite

In this example, a material is created from two constituents with unique grain size distributions. These materials are described in Table 4.2. The resulting microstructure and output size distributions, represented by cumulative distribution functions (CDFs), are shown in Figure 4.12, with maximum likelihood estimators and goodness-of-fit metrics given in Table 4.2. The R^2 value is the coefficient of determination and measures how well the size of each grain matches the size of its corresponding seed.

Table 4.2: Input and output distributions for two phase composite

Phase	Input Volume Fraction	Output Volume Fraction	Input Size Distribution	Output Size Distribution	R^2
1	0.75	0.752	1 + Exp(1)	0.849 + Exp(1.31)	0.973
2	0.25	0.248	Triang(1, 5, 5)	Triang(1.2, 5.2, 5.0)	0.989

In this example, there is very good agreement between the input and output parameters. Equation 4.14 was developed using lognormal area distributions, which is not the case here, yet the grain size distributions are recovered as shown in Figure 4.12. The R^2 values in the

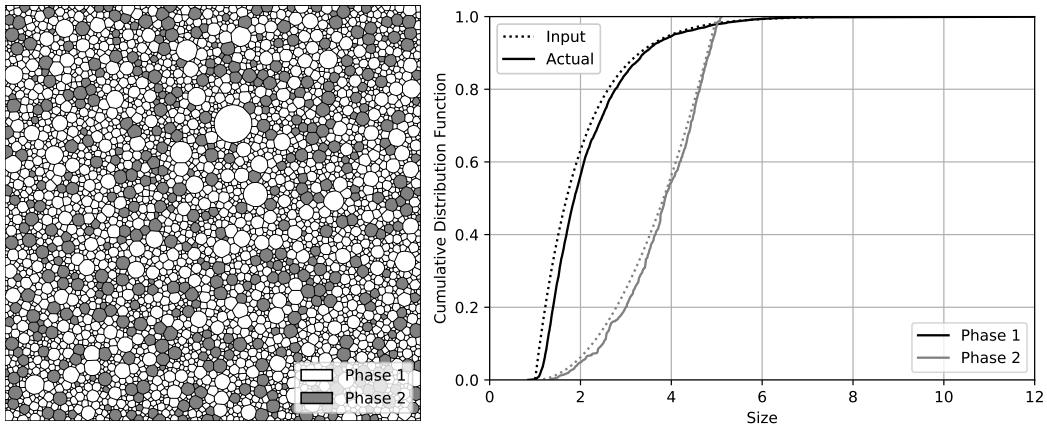

(a) Output microstructure. (b) Input and output grain size distributions.

Figure 4.12: Output microstructure and CDF curves for two phase composite example.

last column of Table 4.2 compare the sizes of the seeds with their corresponding grains. Values near 1 indicate that sizes of an output grain is nearly equal to the size of its seed circle. The data presented in Table 4.2 are for a single instance of the microstructure. Re-running with 10 different RNG seeds, the largest error in volume fractions is 0.009 and the lowest R^2 value is 0.971. The average volume fraction error is 0.003 and average R^2 is 0.98. Overall, there is significant agreement between the input and output grain size distributions, as well as the volume fractions of the two phases.

4.4.2 Ellipsoidal Voids

Ellipsoidal geometries can be generated using the multi-sphere algorithm discussed in subsection 4.2.3. To demonstrate this algorithm, ellipsoidal voids are packed into a 3D microstructure. These voids have a constant height, distributed aspect ratios, and are non-uniformly positioned in the microstructure. The spatial and geometric parameters for the voids are given in Table 4.3. Note that the microstructure domain is a cube with edge length 5. The resulting microstructure, as well as CDF curves of the input and output distributions are shown in Figure 4.13.

The output parameters for each void are taken from an ellipsoid of best fit, in a least-squares sense, to the mesh points on the exterior of the void. The size and shape distri-

Table 4.3: Void spatial and geometric parameters

Parameter	Input Distribution	Output Distribution	R^2
r_z	0.10	0.099	-
r_x/r_z	$U(5, 10)$	$U(5.74, 10.5)$	0.870
r_x/r_y	Arcsine(1,5)	Arcsine(1.05, 5.03)	0.999
θ_z	$U(0°, 180°)$	$U(3°, 179°)$	0.885
z	Triang(0, 5, 5)	Triang(0.20, 5.03, 4.90)	1.00

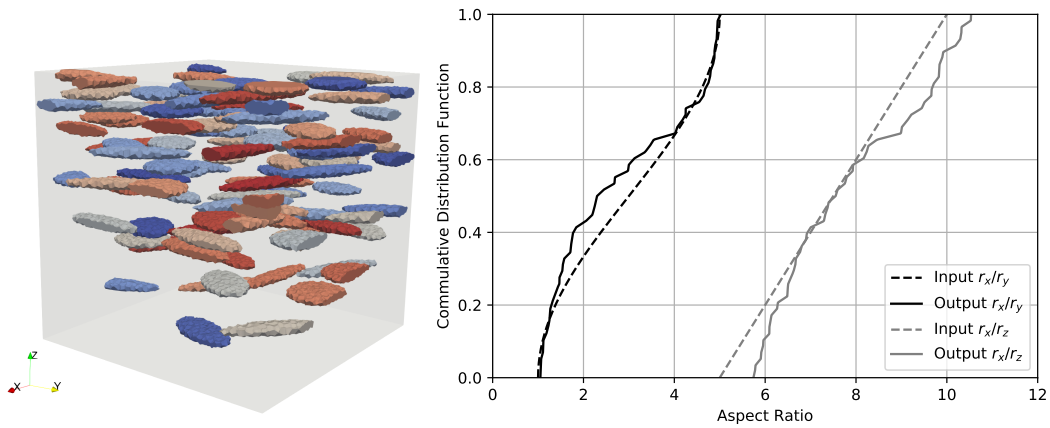

(a) Output microstructure. (b) Input and output aspect ratio distributions.

Figure 4.13: Output microstructure and CDF curves for ellipsoidal void example.

butions agree with the output distributions, notably the ratio between the two long axes of the ellipsoid. The orientation and position distributions also agree well with the inputs. Preferred void position for the top of the RVE is shown in Figure 4.13a and the precise distribution of void positions matches the input distribution to within 4%. Overall, these results indicate strong agreement between the input and output size, shape, orientation, and position distributions for 3D ellipsoids.

4.4.3 Multiple Ellipses in a Elliptical Domain

In this example, three ellipse phases are packed into an elliptical domain to demonstrate meshing in non-rectangular domains. All of the ellipses have random orientation and one has significantly high aspect ratio. The input parameters and the maximum likelihood estimators are given in Table 4.4. The resultant mesh and the output size distributions are

Table 4.4: Ellipse Input Parameters

Parameter	Input Distribution	Output Distribution	R^2
Phase 1			
Volume fraction	0.2	0.20	-
r_x	1	1.03	-
r_y	$U(10, 20)$	$U(10.3, 20.3)$	0.990
Phase 2			
Volume fraction	0.4	0.37	-
r_x	3	3.02	-
r_y	1.5	1.49	-
Phase 3			
Volume fraction	0.4	0.43	-
r	$0.5e^{N(0,0.5)}$	$0.125 + 0.431e^{N(0,0.517)}$	0.939

given in Figure 4.14. The strong agreement between input and output shape parameters in Figure 4.14b offers compelling validation that the algorithm can faithfully reproduce input sizes distributions and volume fractions.

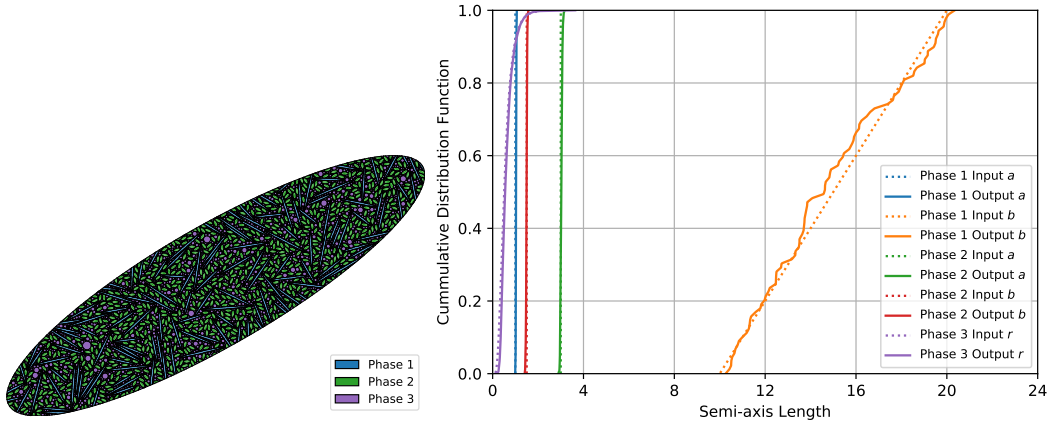

(a) Output microstructure. (b) Input and output size distributions.

Figure 4.14: Output microstructure and CDF curves for ellipse example.

4.4.4 Two-Phase Polycrystal

This example demonstrates the algorithm's ability to recreate 3D polycrystals with lognormal volume distribution. The two phases have different coefficients of variation and are present in a 1:3 ratio. The input distributions and maximum likelihood estimates based on

Table 4.5: Polycrystal Input Parameters

Parameter	Input Distribution	Output Distribution	R^2
Phase 1			
Volume fraction	0.25	0.24	-
V	$0 + e^{N(0,0.9)}$	$0.016 + 0.97e^{N(0,0.91)}$	0.964
Phase 2			
Volume fraction	0.75	0.76	-
V	$0 + 0.5e^{N(0,1.1)}$	$0.032 + 0.51e^{N(0,1.04)}$	0.955

the output are given in Table 4.5. The microstructure and volume distributions are shown in Figure 4.15.

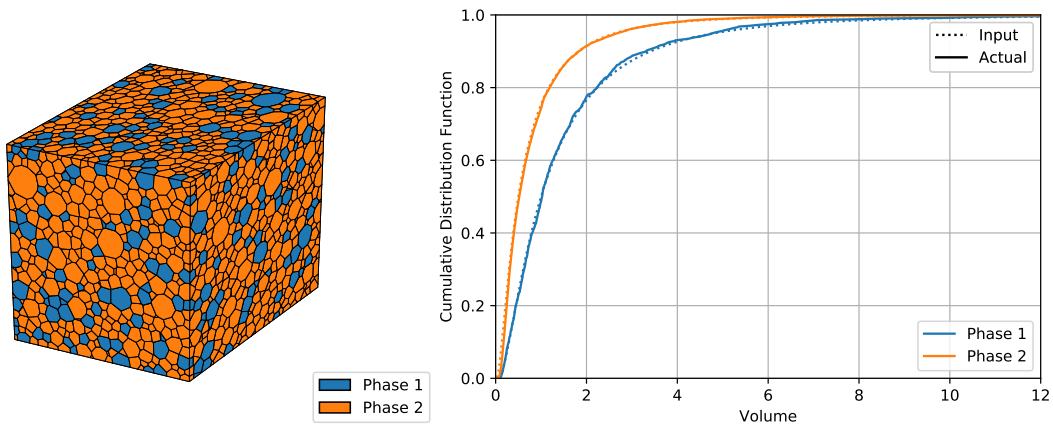

(a) Output microstructure. (b) Input and output volume distributions.

Figure 4.15: Output microstructure and CDF curves for polycrystal example.

The results in Table 4.5 show that the algorithm reproduces polycrystal microstructures in 3D. The two phases have different coefficients of variation, 1.12 and 1.53, which individually would require different α values according to Equation 4.15 for optimal fitting. In this example, the coefficient of variation for the combined phases is 1.42, so the corresponding α from Equation 4.15 is used. The volume distributions in the microstructure are nearly identical to the inputs and the grain volumes match the seed volumes with an $R^2 > 0.95$. The near-total agreement between the grain volume distributions and volume fractions in this example further validate the algorithm in its ability to reproduce microstructures with multiple phases and unique size distributions.

4.4.5 Pegmatitic Granite

The methodology presented in section 4.2 can also be applied to materials with empirically-derived volume fractions and grain size distributions. For example, Voutilainen et al. used X-μCT to study several rock specimen, including pegmatitic granite, which is more coarse-grained than granite. [121] The primary constituents are potassium feldspar (K-feldspar), quartz, and plagioclase feldspar and their volume fractions are 10%, 43%, and 47% respectively. The RVE is shown in Figure 4.16a, while Figure 4.16b shows the empirically-derived grain size distributions, reproduced from [121] as probability density functions (PDFs).

The volume fractions of K-feldspar, quartz, and plagioclase feldspar in the synthetic RVE are 10%, 43%, and 47% respectively. As shown in Figure 4.16b, the output grain size distributions nearly agree with the input distributions. The presented methodology is applicable to parametric and empirically-derived grain size distributions, including those obtained though X-μCT.

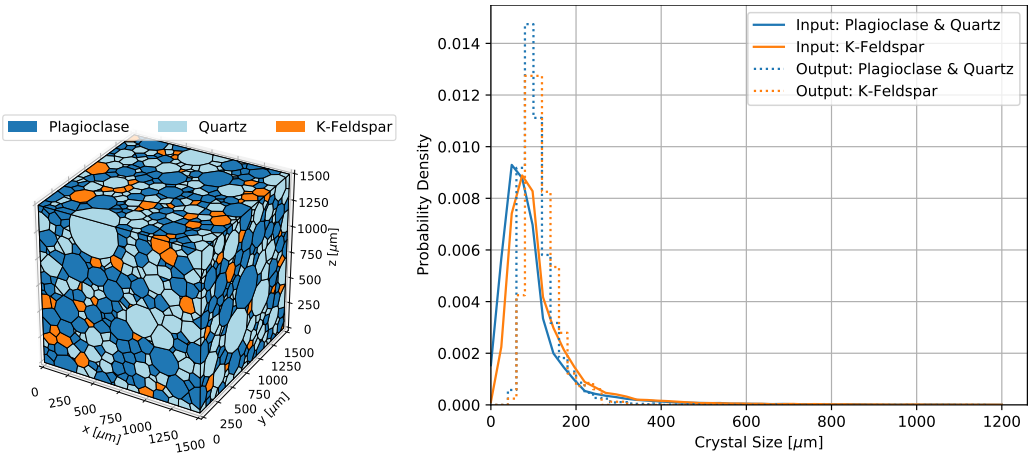

(a) Output microstructure. (b) Input and output size distributions.

Figure 4.16: Output microstructure and PDF curves for granite example.

4.5 Summary

Synthetic microstructures are generated in this work by sampling seeds, positioning them within a domain, decomposing geometric primitives into circles or spheres, tessellating the domain, and quality meshing. Seeds are sampled first by converting volume fractions into population fractions for each phase, then sampling the size and shape distributions corresponding to the phases until the volume of seeds matches the volume of the domain. Next the seeds are positioned in the domain from largest to smallest with overlap testing accelerated by an axis aligned bounding box tree structure. An empirical model estimates the acceptable amount of overlap between seeds based on the coefficient of variation in seed volumes. Decomposition of 2D ellipses follows a previously published approach, which has been extended to decompose arbitrary 3D ellipsoids. Laguerre Voronoi tessellation and unstructured meshing are performed by existing algorithms, ultimately transforming a mathematical description of material microstructure into a mesh instance suitable for direct numerical simulation. This algorithm is implemented in the open source and freely available package called MicroStructPy.

CHAPTER 5
RESULTS

5.1 Introduction

The model presented in chapter 3 has been validated against experiment results for the thermal spallation of Barre granite. [38] The primary goal of the model is to predict recession rate as a function of applied heat flux. The results in Table 4.3 of [38] include both recession rate and spallation temperature for multiple applied heat flux values. Comparison with the spallation temperature is included in this chapter, even though the goal of the model is not to predict temperatures. Both the recession rate and surface temperatures are within the variability of granite physical properties.

The remainder of this chapter is organized as follows. First, section 5.2 compares the simulation results with measured experimental results. These experiments were performed on Barre granite. The transient response is compared first, followed by a detailed discussion of the simulation results for a single heat flux value. After discussing the results for a single heat flux value, the results for all six heat fluxes are presented and compared against the measured data. In the third section, section 5.3, the validated numerical model of thermal spallation is applied to Martian basalt. Results are presented for a nominal porosity, followed by a sensitivity analysis to that porosity value. Lastly, section 5.4 summarizes the results of the simulation.

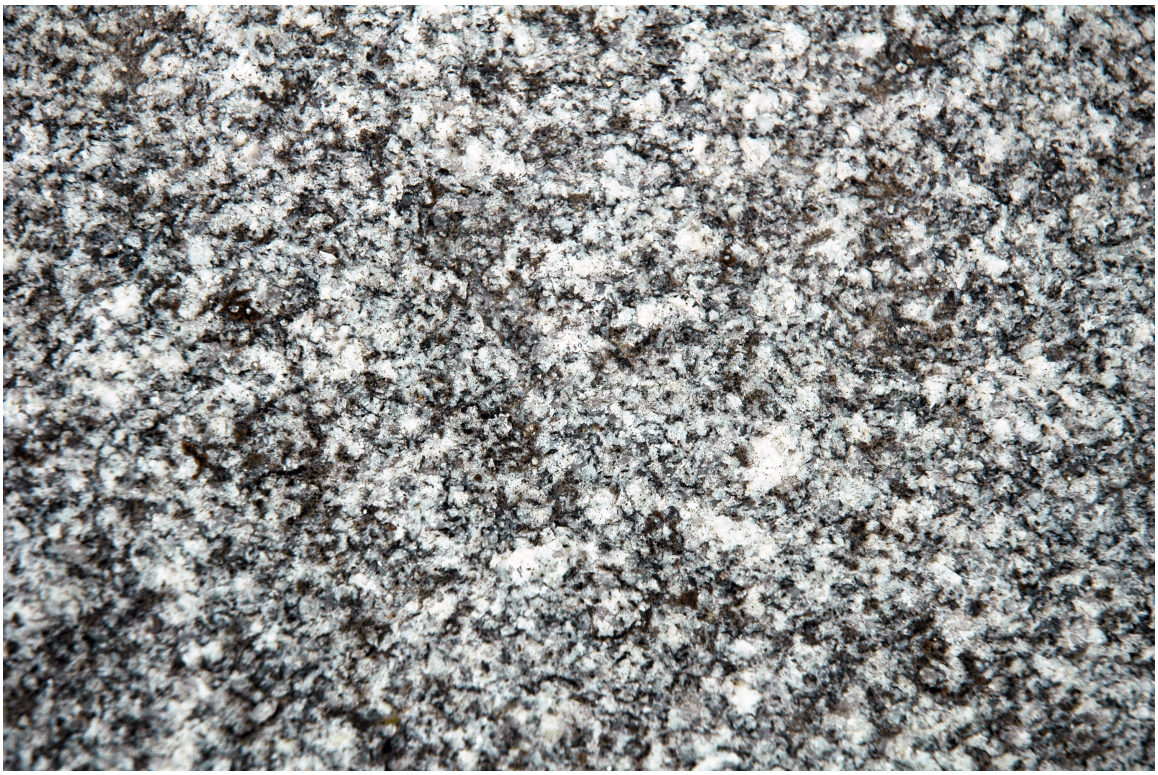

Figure 5.1: Photograph of Barre granite.

5.2 Validation with Barre Granite

5.2.1 Barre Granite Studies

Barre granite, shown in Figure 5.1[1], is an igneous rock intrusion located near Barre, Vermont. It has been used in numerous crack propagation [122, 123, 124, 125, 126] and thermal spallation experiments. [24, 25, 26, 34, 37, 38, 51] Barre granite has similar properties to the crystalline basement rock, deep under the Earth's surface, making it useful for understanding the performance of flame jet spallation drills at significant depth. [25, 38] The results from these studies provide validation data for the thermal spallation model.

The granite composition is approximately 50% plagioclase, 22% quartz, 10% microcline, 8% biotite, 4% muscovite, and 4% other minerals. [127] The feldspar has an average grain size of 0.83 mm, quartz has an average of 0.9 mm, and the biotite has an average

[1]Photo credit: James St. John

of 0.43 mm. [124, 125] The muscovite is assumed to have the same average grain size as biotite. From the values in Table 5.1, the feldspar minerals have a significantly lower thermal expansion coefficient (α) compared to the quartz, muscovite, and biotite. When heat is applied, approximately 60% of the material expands significantly less than the other 40%, creating significant eigenstress in the material.

The temperature-dependent and anistropic material properties of the minerals are available in the literature. The properties of plagioclase are averaged from albite and anorthite. [128, 129, 130, 131, 132, 133, 134, 135] For microcline, the properties were often listed under K-feldspar. [128, 131, 135, 136, 137] The properties of quartz include the α-β transition, where the crystal structure shifts from orthorhombic to trigonal. [131, 132, 137, 138, 139, 140, 141, 142] Muscovite [140, 143, 144, 145] and biotite [131, 132, 140, 144, 146, 147, 148] properties are also available in the literature. The room temperature isotropic properties of plagioclase (pl), microcline (k), quartz (qz), muscovite (ms), and biotite (bt) are provided in Table 5.1, however the fully anisotropic and temperature-dependent properties are available in the cited literature.

Table 5.1: Room temperature isotropic properties of Barre granite minerals.

Property	pl	k	qz	ms	bt	Units
ρ	2.69	2.56	2.65	2.82	2.95	g/cm^3
C_p	705	610	698	799	779	J/kg-K
k	2.00	1.78	4.85	2.79	2.27	W/m-K
E	77.7	71.5	114	81.5	63.3	GPa
ν	0.28	0.28	0.08	0.24	0.26	-
α	4.70	3.14	11.5	11.3	17.8	10^{-6}/K

5.2.2 Synthetic Representation of Microstructure

Synthetic microstructures for Barre granite are created from the data above using the software package MicroStructPy. [82] An example microstructure with a length of 30 mm and height of 15 mm is shown in Figure 5.2. Heat is applied to the $+y$ surface and, as the simulation evolves, that top surface progresses downwards. Once the top surface crosses the

$y = 0$ line, the simulation terminates. The 5 mm layer of material beneath this line ensures that the adiabatic heat flux boundary condition on the $-y$ surface does not interfere with the simulation results. The length, height, and ghost layer thickness values were determined through a convergence study on the domain dimensions.

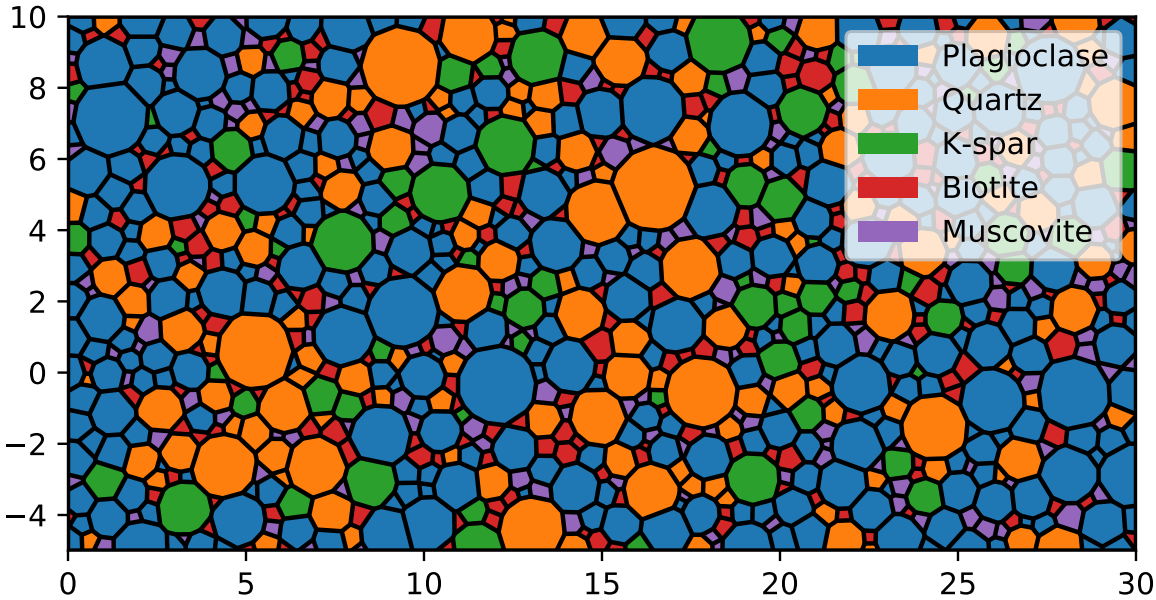

Figure 5.2: Synthetic microstructure of Barre granite.

Comparing Figure 5.1 and Figure 5.2, the synthetic microstructure contains mostly-circular grains, while the granite microstructure is more stippled and angular. The grain boundaries in the synthetic microstructure are linear and each grain is a convex polygon, a consequence of the Laguerre-Voronoi tessellation, discussed in subsection 4.2.4. Despite the difference in grain geometry, the microstructure in Figure 5.2 has the same grain size distribution and composition as the reported values for the granite in Figure 5.1.

At the grain boundaries there are three key material properties: the gap conductance, the maximum stress, and the fracture energy. The gap conductance is tuned, in the following subsection, to match the transient thermal response of the granite. The maximum stress and fracture energy are set based on the overall strength of Barre granite. [149, 150]

The following subsection shows the results of tuning the gap conductance according to the transient response at an applied heat flux of 0.5 MW/m^2. In the steady-state subsection,

the recession rates and surface temperatures at multiple heat fluxes are compared against experimental results.

5.2.3 Transient Response

Before spallation occurs, the temperature within the material follows the semi-infinite solid solution for isotropic materials:

$$T = T_0 + \frac{2q''}{k}\sqrt{\frac{\kappa t}{\pi}} \tag{5.1}$$

where κ is the thermal diffusivity. The bulk thermal conductivity appears in both the k and κ terms, and it is influenced by the contact conductance between the grains. The lower the contact conductance, the lower the bulk thermal conductivity. Rearranging the terms in Equation 5.1 creates a linear expression in time:

$$\frac{1}{k}t = \frac{\pi}{4}\rho C_p \left(\frac{T - T_0}{q''}\right)^2 \tag{5.2}$$

The coefficient $1/k$ is an unknown parameter, while values for t and the right hand side of Equation 5.2 are given in Figure 5.3. The value of ρCp is estimated by rule of mixtures from Table 5.1 and q'' is 0.5 MW/m^2 in Figure 5.3, which reproduces the experimental data and semi-infinite solid model from Figure 4.8 in [38]. Based on the rule of mixtures, the volumetric heat capacity is approximately 1.9 MJ/m^3-K. Applying linear regression to Equation 5.2, the thermal conductivity of this Barre granite sample is approximately 3.1 W/m-K.

The objective, therefore, is to determine the contact conductance value that yields an effective thermal conductivity of 3.1 W/m-K. This value was determined using DNS by applying heat flux to the synthetic microstructure in Figure 5.2 and measuring the average surface temperature over time. The contact conductance value that most closely matches the homogeneous thermal conductivity is 900 W/m^2-K.

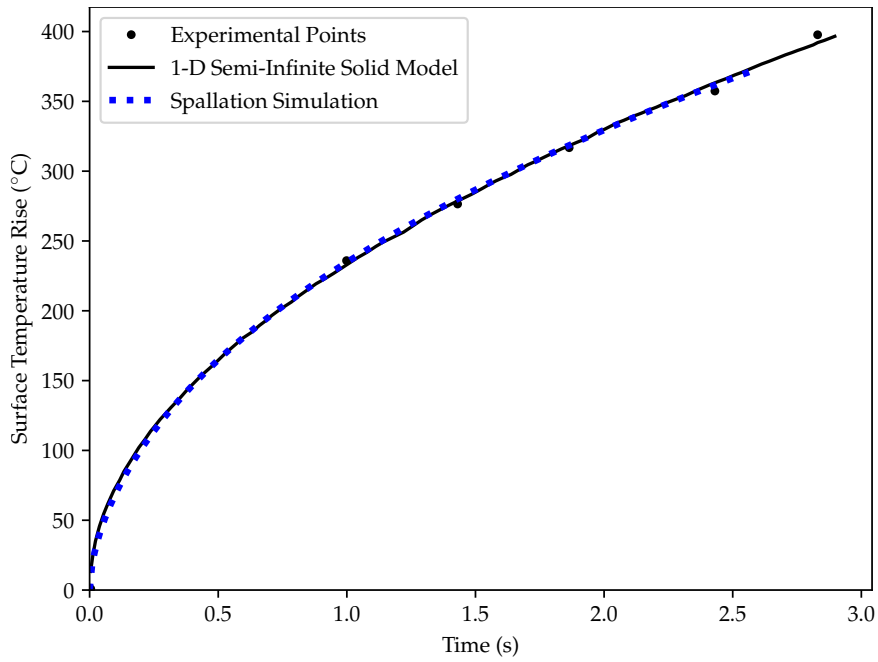

Figure 5.3: Transient thermal response of Barre granite from experiments and simulation.

For reference, typical contact conductance values are in the range of 400-2000 W/m^2-K. [151] Contact conductance values depend on the surface roughness of the grains at their interface, with smoother surfaces having higher conductance values. [152] For the same amount of heat flux, a higher conductance value results in a smaller temperature difference across the interface, which is illustrated by Equation 3.11. At 900 W/m^2-K, the grain boundaries are considered rough surfaces.

The 0.5 W/m^2 applied heat flux is not high enough to induce spallation. At higher heat fluxes, the surface temperature rises according to Equation 5.1 until spallation begins. Once spalls begin to transport heat away from the material, the surface temperature reaches a steady-state. The following subsection compares the steady-state surface temperature and recession rates documented in [38] with the simulation results.

5.2.4 Steady State Response

Thermal spallation results are presented for a range of heat flux values, from 0.8 to 2.9 MW/m^2, in Table 4.3 of [38]. The results for 1.4 MW/m^2 are discussed first, followed by a

comparison over the entire range.

Spallation with 1.4 MW/m^2 of Applied Heat Flux

Figure 5.4 shows the average surface temperature rise and the recession depth from DNS. This figure also shows a model fit of the temperature and depth profiles. Similarly, Figure 5.5 shows the temperature rise histories of surface nodes, with the median trend and a model fit.

The model fits in Figure 5.4 and Figure 5.5 take the kernels in Equation 5.3 and Equation 5.4, where the $\sim$ indicates an estimated quantity. The substitution in Equation 5.6 is used for convenience, with the three fundamental parameters to these kernels being the time to reach steady-state (t_s), the volumetric heat capacity (ρC_p), and the effective bulk thermal conductivity, (k). With three independent curves, these three quantities can be uniquely determined by minimizing the sum of squared residuals.

$$d(t) = \tilde{v}\max(0, \tilde{t_s} - t) \tag{5.3}$$

$$\Delta T_{\text{surf}}(t) = 2q''\sqrt{\frac{\min(t, \tilde{t_s})}{\pi\tilde{k}\,\widetilde{(\rho C_p)}}} \tag{5.4}$$

$$\Delta T_{\text{spall}}(t) = \frac{2q''}{\pi\tilde{v}\widetilde{(\rho C_p)}}\,e^{-\pi\left(\frac{\tilde{v}^2\widetilde{(\rho C_p)}t}{2\tilde{k}}\right)^2} + \frac{q''\tilde{v}}{\widetilde{(\rho C_p)}}\,\text{erfc}\left(\frac{-\widetilde{(\rho C_p)}\tilde{v}^2 t\sqrt{\pi}}{2\tilde{k}}\right) \tag{5.5}$$

$$\tilde{v} = \frac{\tilde{k}}{\pi\tilde{t_s}\widetilde{(\rho C_p)}} \tag{5.6}$$

The best fitting parameters to these models are a time to reach steady-state (t_s) of 1.1 s, a volumetric heat capacity (ρC_p) of 1.8 MJ/m^3-K, and a thermal conductivity (k) of 3.7 W/m-K. These fitting parameters are *not* meant to be estimates of the physical properties of granite. They are, however, meant to create a unify model across the three trends observed

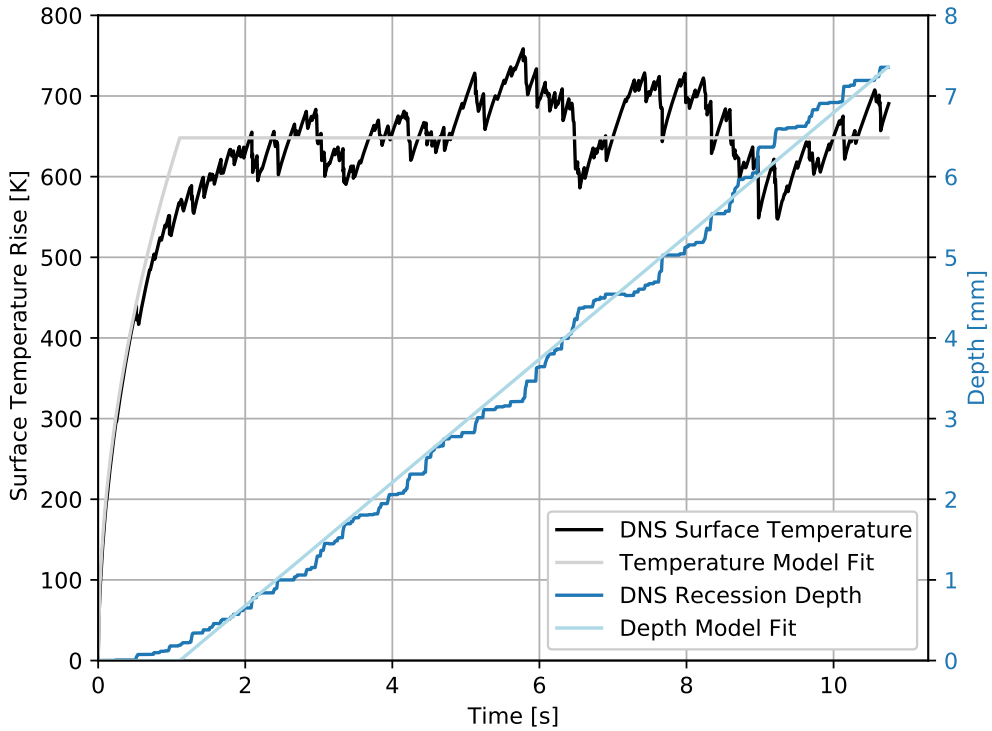

Figure 5.4: Simulated temperature and recession for Barre granite exposed to 1.4 MW/m^2.

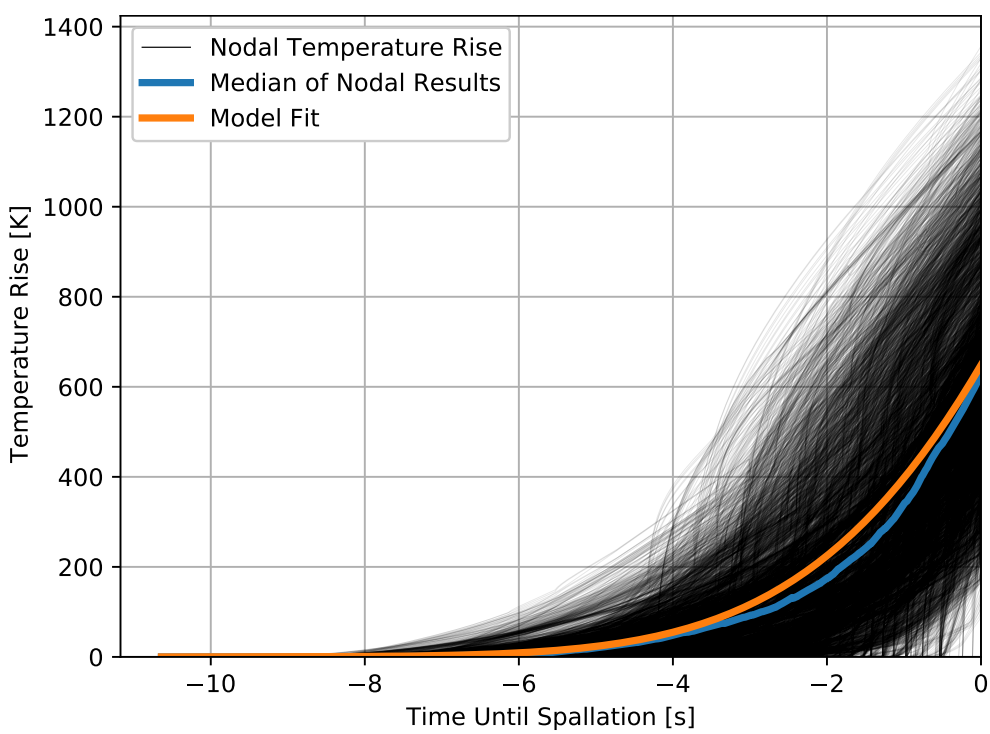

Figure 5.5: Simulated nodal temperatures for Barre granite exposed to 1.4 MW/m^2.

in the simulation results: recession depth, surface temperature rise, and the median temperature rise history. The fact that the volumetric heat capacity and the thermal conductivity values are in agreement, to within 20%, with the published values is a strong indication that the 1D semi-infinite solid solution is an appropriate kernel to model thermal spallation.

Snapshots of the simulation in Figure 5.4 are shown in Figure 5.6 for further discussion of the simulation results. Figure 5.6a and Figure 5.6b show the temperature and xx stress component shortly before reaching the steady-state conditions. Some of the surface grains have already spalled away, though in the middle of the domain the temperature distribution is approximately 1D. The increase in temperature creates compressive stress along the top of the domain, with some individual grains experiencing tension. These grains are feldspar and surrounding by quartz, biotite, and muscovite.

As time advances, the average surface temperature rise is approximately 648 K. The surface roughness in Figure 5.6 is consistent with the snapshots in Figure 1.4. Grains that protrude from the surface achieve much higher temperature rises since they spend more time subjected to the heat flux. These protruding grains also contain complex stress distributions. The grains are free to expand except where they are bonded to the domain. There are no tractions on those free boundaries, however the cohesive zones are putting stresses into the grains. This combination of boundary conditions within the protrusions create complex stress distributions. The surface roughness is approximately 3 grain widths. Surface grains experiencing tension will propagate that tension down into the material. These complex stress structures within the material weaken the cohesive zones before the grains they are attached to become directly exposed to the heat flux. The surface temperature distribution remains approximately 1D throughout the simulation, while the stress distribution changes significantly. Generally, the stress is mostly compressive, but the distribution of grains with low and high thermal expansion coefficients greatly affects the stress distribution in the top layer of material.

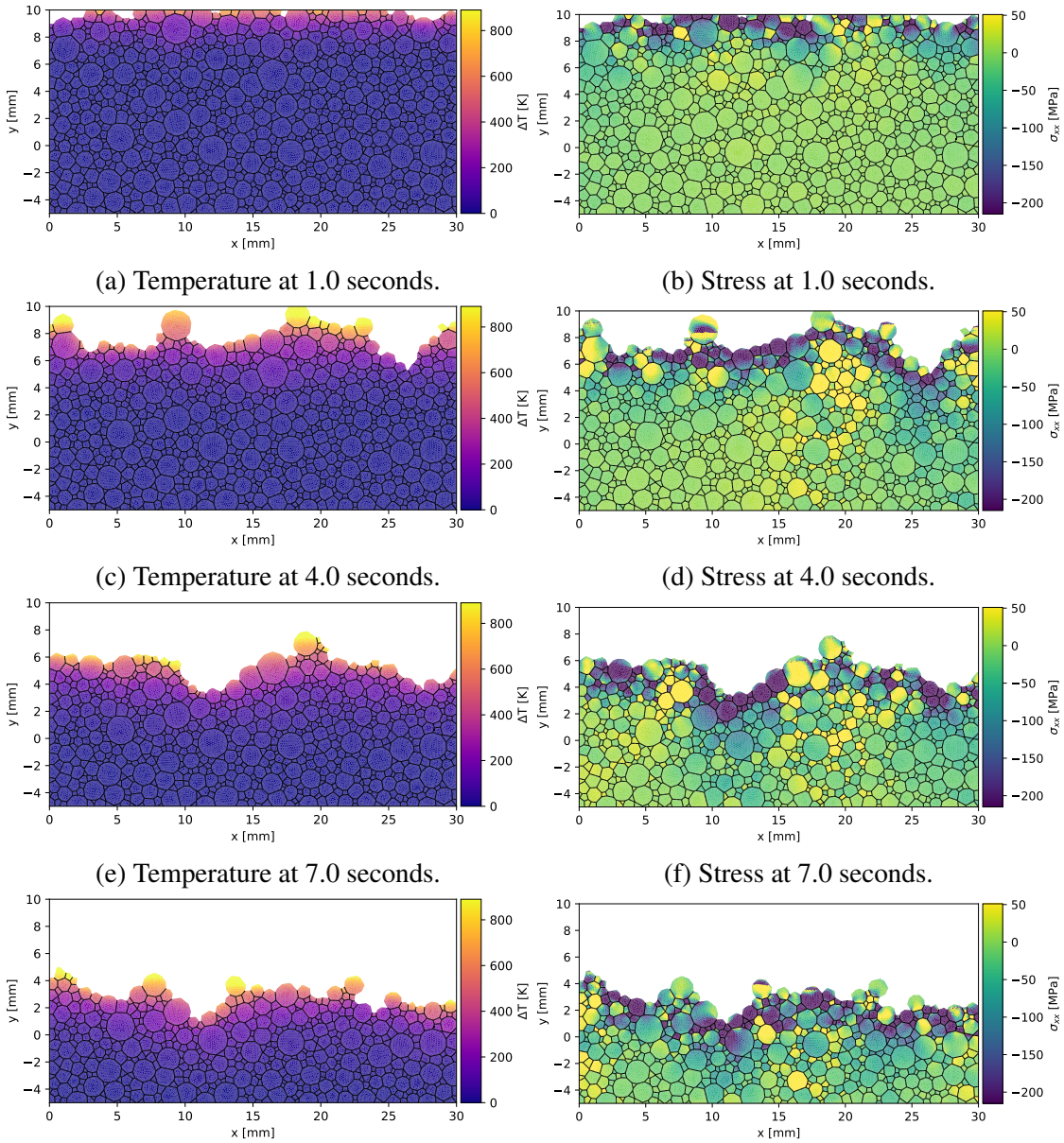

(a) Temperature at 1.0 seconds.

(b) Stress at 1.0 seconds.

(c) Temperature at 4.0 seconds.

(d) Stress at 4.0 seconds.

(e) Temperature at 7.0 seconds.

(f) Stress at 7.0 seconds.

(g) Temperature at 10.0 seconds.

(h) Stress at 10.0 seconds.

Figure 5.6: Snapshots of Barre granite exposed to 1400 MW/m^2

Range of Heat Fluxes

A range of heat fluxes are applied to Barre granite in [38], from 0.8 MW/m^2 to 2.9 MW/m^2. These heat fluxes are applied to the microstructure in Figure 5.2 and the average surface temperature rise and recession rate are measured for comparison. Figure 5.7 and Figure 5.8 show the the temperature rise and recession rate, respectively, from the experimental results and from the simulation. In Figure 5.7, additional temperature data from [38] are shown to indicate the range of temperatures sampled from the experiments. To reflect this uncertainty, and the temperature variance about the steady state shown in Figure 5.4, the dispersion in the simulation results is included in Figure 5.7. Similarly, the variability of the recession rate shown in Figure 5.4 is captured by the dispersion in Figure 5.8.

Comparing the surface temperature results in Figure 5.7, the simulation matches experimental measurements at lower heat flux values. At higher heat fluxes, the simulation under-predicts the surface temperature rise. This is consistent with the over-predicted recession rates at higher heat flux values. According to the analytic model, $v\Delta T \propto q''$, so an under-prediction of the temperature rise is balanced by the over-prediction in recession rate. Overall, the trends in the measured and simulated results are consistent. At 1.4 and 2.9 MW/m^2, the same temperature is measured multiple times, so the spread in temperatures at these heat fluxes is unknown.

The differences between the measured and simulated surface temperature rises are on the order of 100 K, about 15-20%. This spread is comparable to the spread in measured temperatures at 1.9 MW/m^2. For the recession rates, the differences are on the order 0.25 mm/s, which is also about 15-20%. These differences are on the order of accuracy in the observations, though there is room for better fitting. The errors may be attributable to different flaw distributions in individual minerals and in the homogeneous granite. Contact conductance accounts for differences in thermal conductivity, however dislocations and inclusions within the grains can diminish the volumetric heat capacity. If the mineral grains have a lower heat capacity, then the same amount of applied heat will create a larger temper-

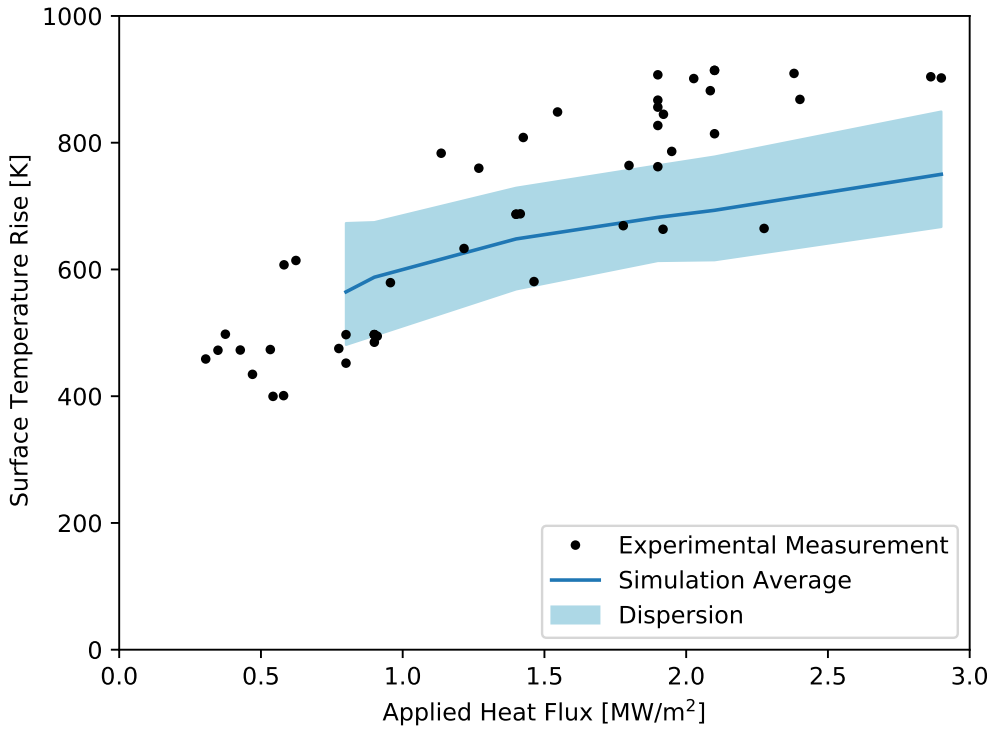

Figure 5.7: Comparison of surface temperature rises for a range of heat fluxes.

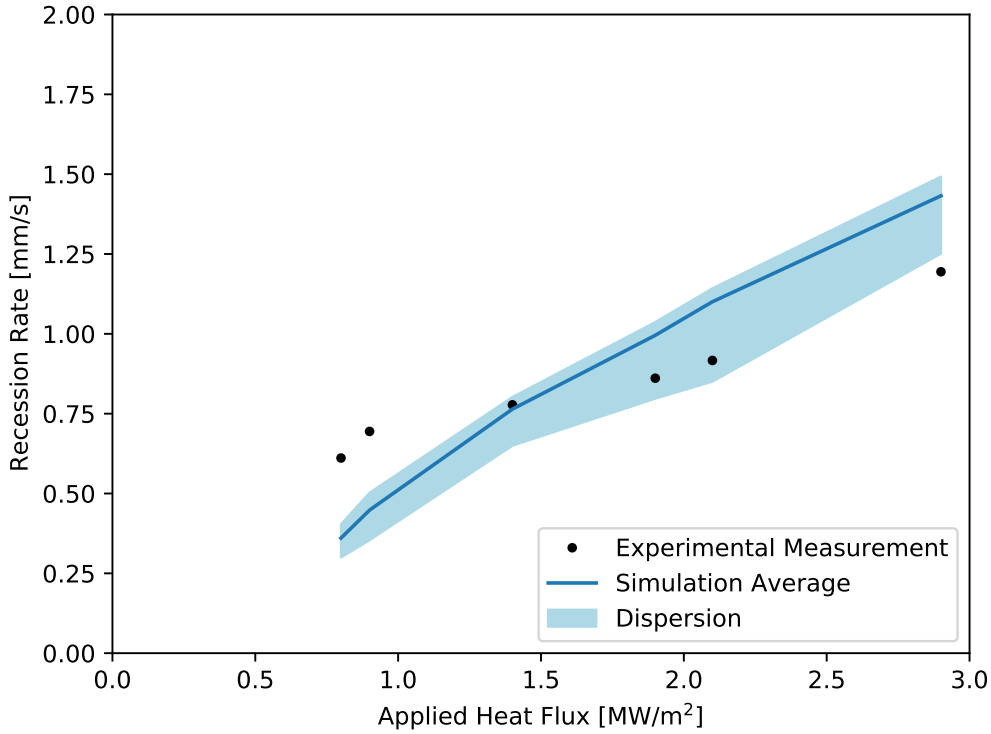

Figure 5.8: Comparison of recession rates for a range of heat fluxes.

ature rise. The thermal inertia, $\sqrt{k\rho C_p}$, of the simulated material matches that of the Barre granite sample, through tuning the gap conductance. Homogeneous physical properties of rocks, such as bulk thermal conductivity, can vary by over 30% for the same type of rock, taken from the same site. [140] The 15-20% error between the simulation and measured results is acceptable and appropriate for the material used to validate the simulation.

5.3 Application to Martian Basalt

5.3.1 Properties of Basalt at Gusev Crater, Mars

The composition of several basalts is given in Table 5.2. These percentages are by weight, however scaling by the densities in Table 5.3 produces volume fractions. Based on the proportions of feldspar end members, the feldspar is a plagioclase with approximately 50% anorthite which categorizes it as an andesine. The olivine crystals also appear to be in the middle of their series, at approximately 50% forsterite. Diopside and hypersthene are the remaining main minerals, with trace amounts of magnetite, chromite, ilmenite, and apatite. Only plagioclase, olivine, diopside, and hypersthene are included in the numerical simulation. Additionally, a nominal porosity of 15% is added to the simulation. The pores are on the scale of the aphanitic components.

The basalts at Mars are *picritic*, meaning they are rich in olivine and the olivine crystals are larger than the rest of the components. Grain size distributions are not available for Gusev basalt, however it is similar to shergottites and Hawaiian picritic basalt.[61] The distribution for olivine is taken from a shergottite and the distribution for the aphanitic components is from Hawaiian picritic basalt.[153, 154] These distributions are reproduced in Figure 5.9.

The composition and grain sizes, in Table 5.2 and Figure 5.9, are sufficient to generate a synthetic microstructure of Martian basalt. The aspect ratio of the olivine phenocrysts is an informed estimate based on discussions at the Astromaterials Research and Exploration Sciences (ARES) Division at NASA Johnson Space Center. [155] The domain size

Table 5.2: Percent Weight Composition of Gusev Basalts[61]

Component	End Member	Adirondack	Humphrey	Mazatzal
Feldspar		36.8	38.0	40.0
	Orthoclase	0.18	0.53	0.65
	Albite	17.68	19.88	22.17
	Anorthite	18.97	16.60	17.42
Olivine		21.7	20.2	28.6
	Forsterite	11.18	9.86	12.89
	Fayalite	10.51	10.33	15.73
Diopside		13.17	15.70	16.23
Hypersthene		18.86	16.60	7.42
Magnetite		5.26	4.87	3.06
Chromite		0.91	0.99	0.87
Ilmenite		0.93	1.10	1.08
Apatite		1.28	1.40	1.49

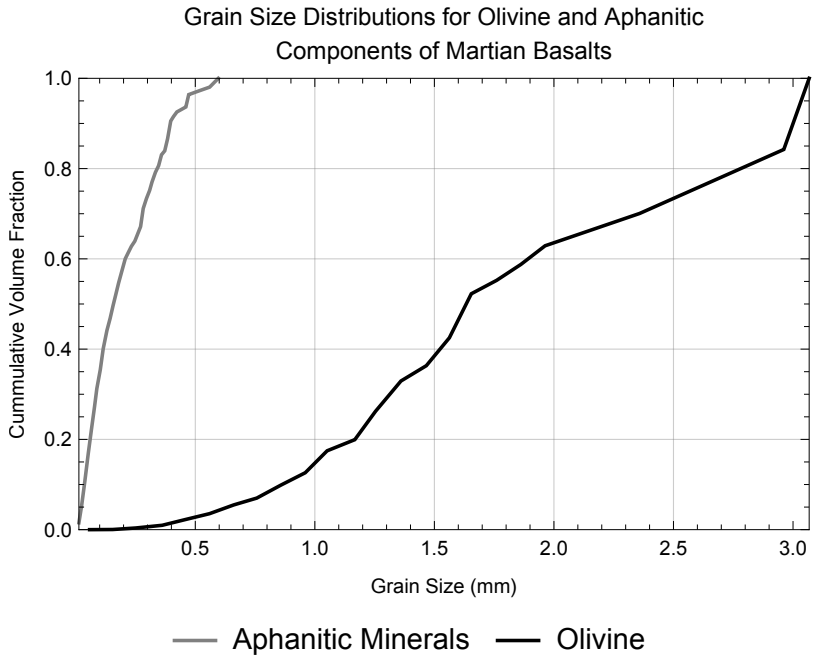

Figure 5.9: Grain size distributions in Martian basalt.

of the microstructure was scaled based on the olivine phenocrysts, rather than the aphanitic components. The resulting RVE contains over 11,000 grains, as shown in Figure 5.10.

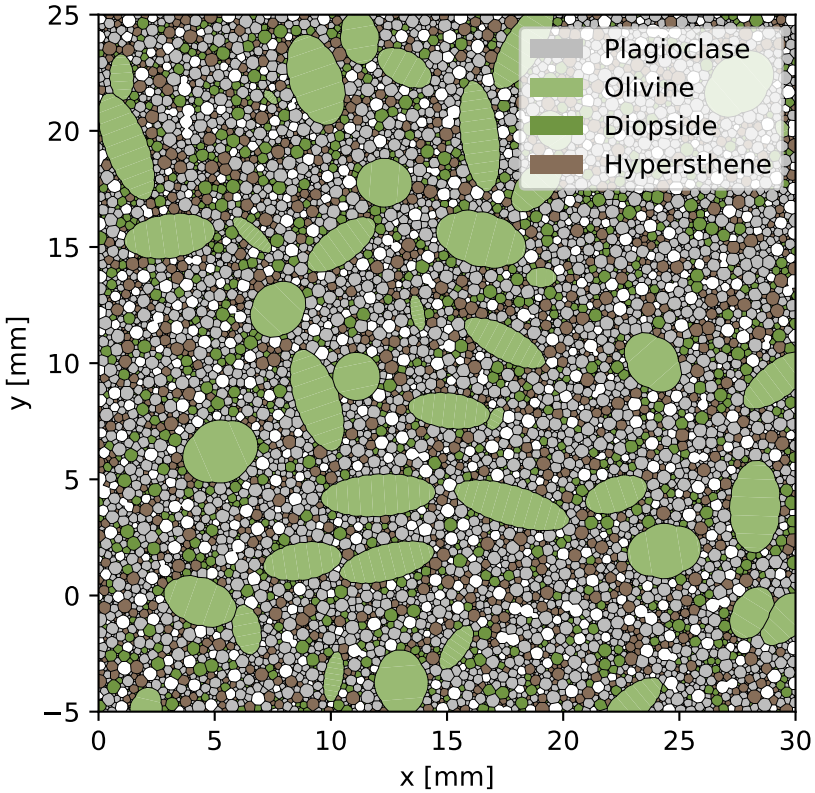

Figure 5.10: Synthetic microstructure of Martian basalt.

The mineral properties of plagioclase [128, 129, 130, 131, 132, 133, 134, 135], olivine [128, 129, 131, 132, 140, 156, 157, 158, 159, 160], diopside [129, 161, 162, 163], and hypersthene [128, 129, 134, 140, 161] are available in the literature. Table 5.3 gives the fully anistropic material properties at room temperature, as a point of reference. One exception is that anisotropic thermal conductivity (k) is unavailable, so the off-diagonal terms are zeros. The simulation uses temperature dependent properties, which is too much data to include in a table. The data in Table 5.3 allow for some insights into the dissimilar material properties of Martian basalt.

These four minerals have significantly different properties, in different ways than Barre granite. The driving factor in thermal spallation of granite is the quartz content because its coefficient of thermal expansion is significantly higher than the other minerals. In basalt,

Table 5.3: Material properties of basaltic minerals at room temperature.

Property	Plagioclase	Olivine	Diopside	Hypersthene	Units
ρ	2.69	3.22	3.31	3.20	g/cc
C_p	753	927	769	818	J/kg-K
k_{11}	2.00	7.00	9.34	7.10	W/m-K
k_{22}	2.00	7.00	9.34	7.10	W/m-K
k_{33}	2.00	7.00	9.34	7.10	W/m-K
C_{1111}	99	311	204	225	GPa
C_{2222}	184	207	175	178	GPa
C_{3333}	161	236	238	214	GPa
C_{2323}	23	70	68	78	GPa
C_{1313}	33	81	59	76	GPa
C_{1212}	36	81	70	82	GPa
C_{2233}	25	73	48	53	GPa
C_{1133}	43	70	88	54	GPa
C_{1122}	50	69	84	72	GPa
C_{1312}	1	0	0	0	GPa
C_{2312}	-4	0	-11	0	GPa
C_{2313}	0	0	0	0	GPa
C_{1123}	3	0	0	0	GPa
C_{2213}	-6	0	-20	0	GPa
C_{3312}	-1	0	0	0	GPa
C_{2212}	-3	0	0	0	GPa
C_{1112}	-3	0	0	0	GPa
C_{1113}	-5	0	-19	0	GPa
C_{3313}	-5	0	-34	0	GPa
C_{3323}	0	0	0	0	GPa
C_{2223}	1	0	0	0	GPa
α_{11}	6.89	6.53	18.50	8.03	10^6/K
α_{22}	4.71	9.76	8.90	8.03	10^6/K
α_{33}	3.30	9.73	3.70	8.03	10^6/K
α_{23}	-0.82	0.00	0.00	0.00	10^6/K
α_{13}	-0.07	0.00	0.00	0.00	10^6/K
α_{12}	-0.43	0.00	0.00	0.00	10^6/K

the volumetric heat capacities range from 2.0 to 3.0 MJ/m^3-K. The plagioclase thermal properties are fairly low overall, with a thermal inertia that is less than half the value for olivine. As heat is applied to the plagioclase, temperatures will rise quickly from low heat capacity, and the heat will remain in the plagioclase crystals due to low conductivity. From the stiffness tensors of these minerals, the non-zero values are in the axial components and the diagonal for the shear components. In index notation, these would be C_{iijj} and C_{ijij}, which indicates that the minerals are orthotropic rather than fully anistropic. Comparing the off-diagonal terms of C_{iijj} and the shear diagonals, the minerals also appear to be transversely isotropic. A common example of a transversely isotropic material would be a tree trunk, since it has radial symmetry, but different strength properties depending on whether a load is applied along the fibers or against them. Based on the C_{iiii} terms, there are significant variations in the stiffness along and across the fiber direction. Olivine, for example, is approximately three times stronger along its fiber direction than plagioclase. Comparing the thermal expansion coefficients, the minerals are mostly cubic with one major off-diagonal for plagioclase. Diopside has a high coefficient along one of its axes, with the rest of the minerals displaying transverse isotropy. Based on this analysis, the minerals in Martian basalt are transversely isotropic with significant directionality on the stiffness and thermal expansion coefficients.

5.3.2 Thermal Spallation of Martian Basalt

As with the granite model, first the results for a single value of heat flux are discussed, followed by a discussion for a range of heat fluxes. At 2.9 MW/m^2, the basalt spalls significantly slower than the granite. The steady-state surface temperature is approximately the same, as shown in Figure 5.11, however the recession rate is 0.69 mm/s. For the same applied heat flux, the granite recesses at 1.43 mm/s. Based on the analytic relationship in Equation 1.7, a lower recession rate for the same applied heat flux and temperature rise indicates a higher volumetric heat capacity.

Based on the ratio of recession rates and the granite heat capacity, the analytic model predicts that basalt would have a heat capacity of 3.9 MJ/m^3-K. From the model fits in Figure 5.11 and Figure 5.12, the heat capacity of basalt is 3.7 MJ/m^3-K. The basalt also takes half the time to reach steady state compared to the granite because its thermal conductivity is half that of granite, creating a factor of four under the square root in Equation 1.6. Lower heat capacity and conductivity result in a material that reaches the same temperature rise in a shorter amount of time.

The temperature and stress distributions within the basalt are shown in Figure 5.13. The temperature rise is concentrated in the very top of the material, which is consistent with low thermal conductivity and heat capacity. Porosity does not have a significant effect on the temperature distribution, however it does affect the stress distribution. Stress remains higher in magnitude at the top surface, however the pores concentrate that stress to flow around them. To the side of a pore, grains have a traction-free boundary condition and can expand strain-free into that space. Pores in the microstructure create a complex stress distribution in the basalt.

Figure 5.14 and Figure 5.8 show predictions for the temperature rise and recession rate of Martian basalt at multiple temperatures. Below 1.4 MW/m^2, the surface temperature rises but the material does not spall. It may be possible to achieve the same recession rate as granite by increasing the heat flux rate, however that may cause phase changes in the material from solid to liquid.

The results in Figure 5.15 could be used in a simulation of landing on basalt at Mars. CFD solutions of the exhaust flow are generated at multiple altitudes during landing. These solutions can include the convective heating boundary condition at the surface, effectively the heat flux applied in this simulation. The heat flux distribution across the landing site can be converted into a recession rate distribution through Figure 5.15. For each CFD run, there would be a recession rate distribution on the surface. Integrating in time between the CFD runs would produce the total recession depth for each point at the landing site. Given

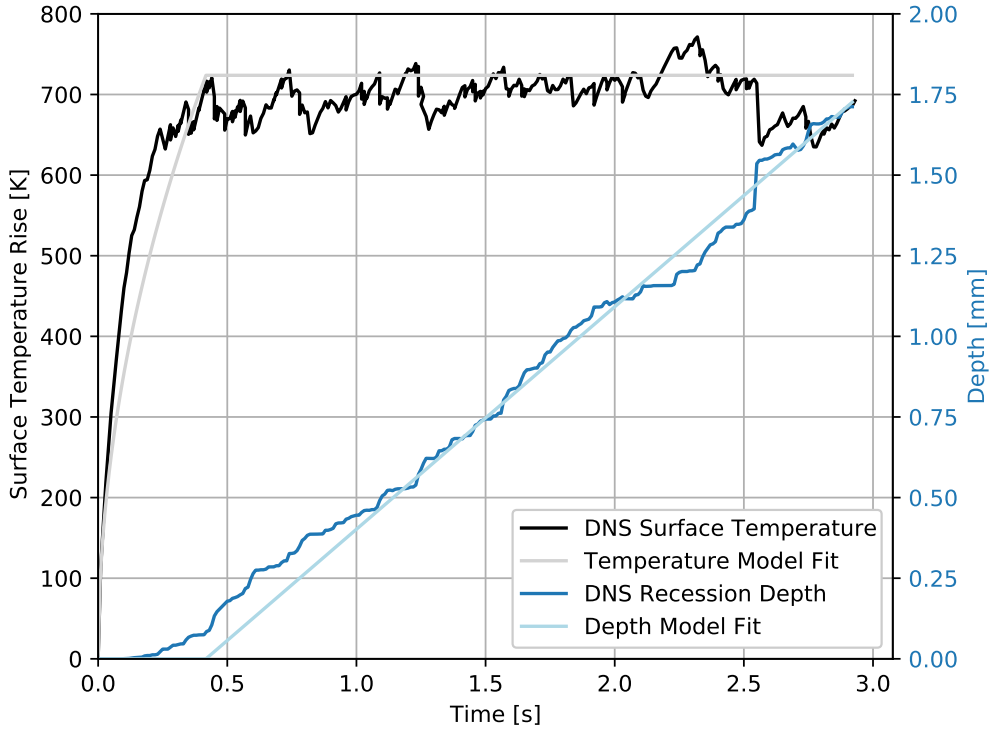

Figure 5.11: Simulated temperature and recession for Martian basalt exposed to 2.9 MW/m^2.

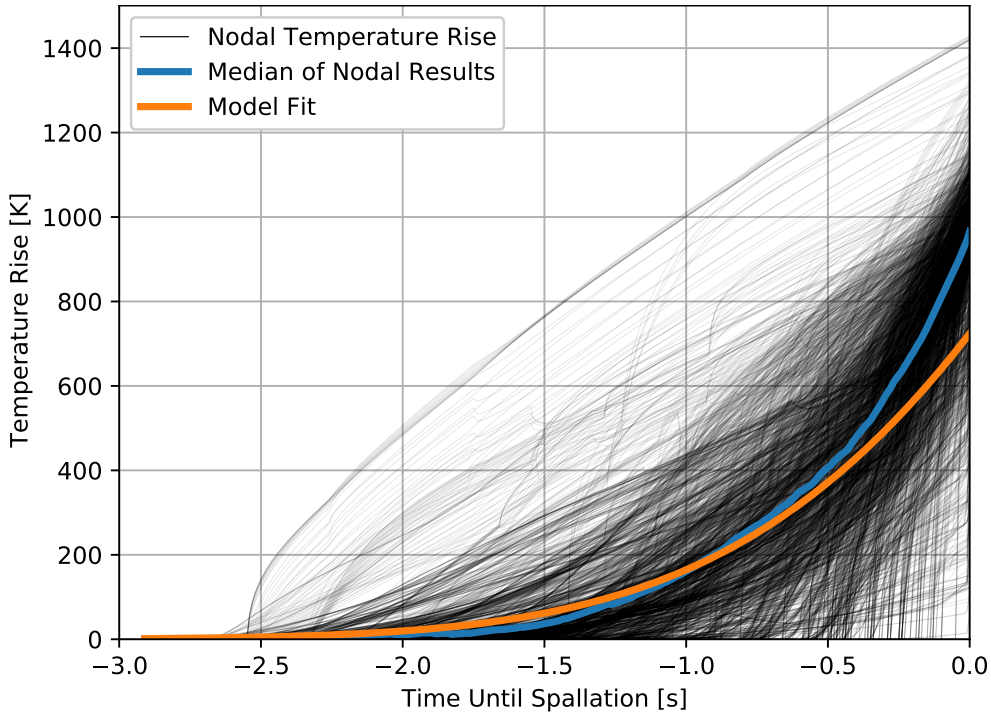

Figure 5.12: Simulated nodal temperatures for Martian basalt exposed to 2.9 MW/m^2.

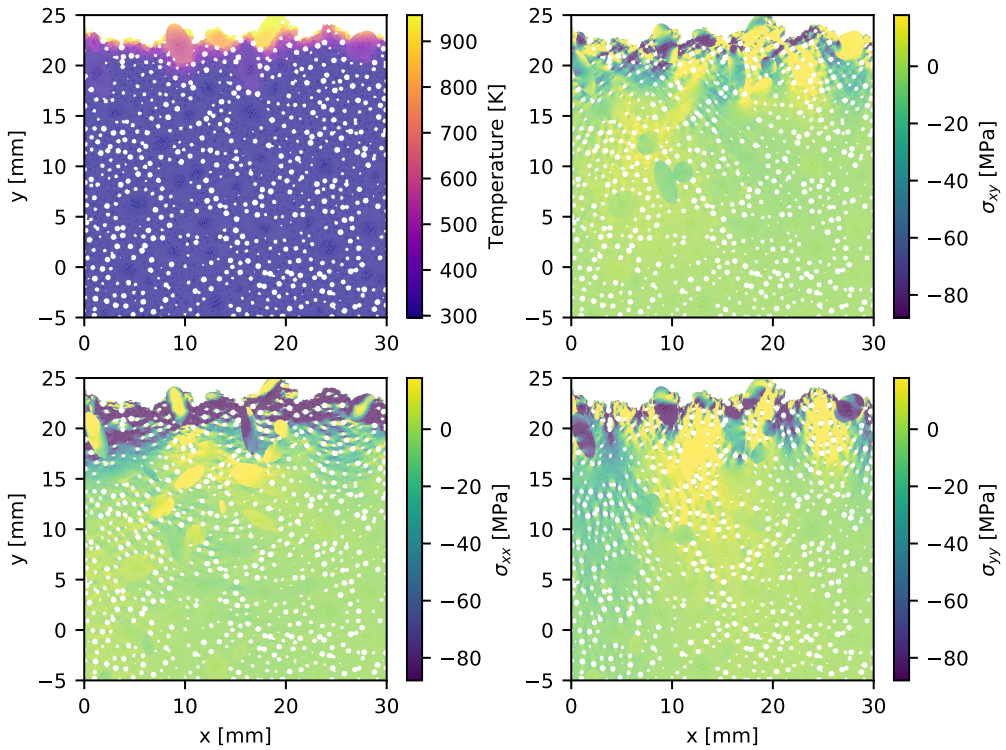

Figure 5.13: Temperature and stress distributions for Martian basalt after 2.9 seconds.

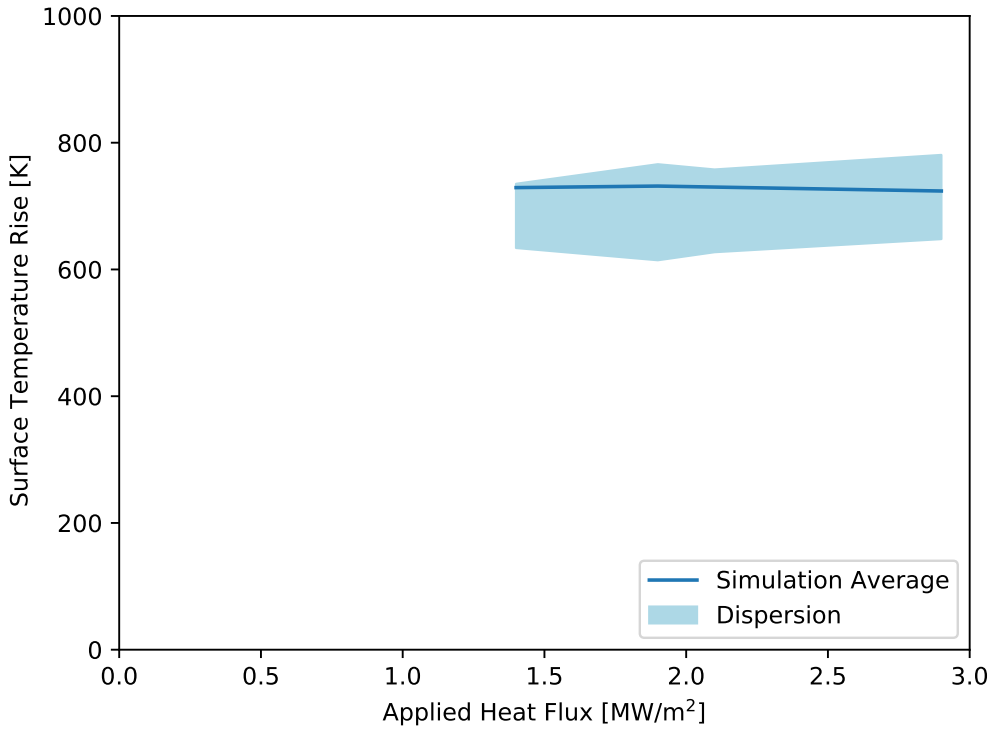

Figure 5.14: Comparison of basalt temperature rises for a range of heat fluxes.

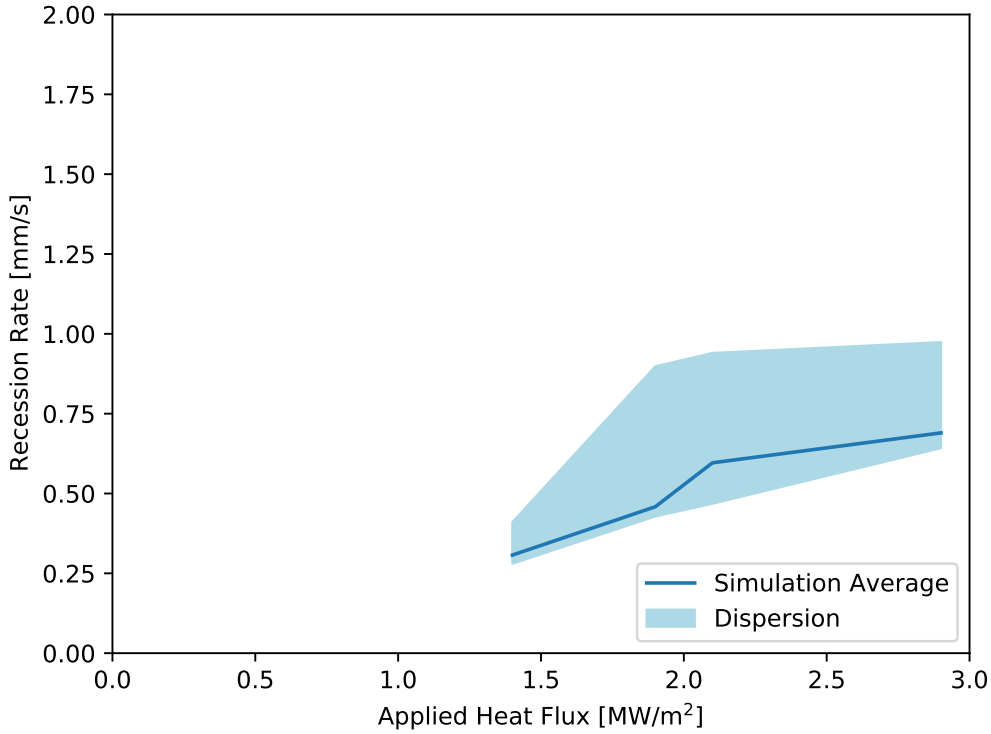

Figure 5.15: Comparison of basalt recession rates for a range of heat fluxes.

the magnitude of the recesssion rate, the recession is not expected to be significant enough to warrant re-meshing the CFD grid.

5.3.3 Influence of Porosity on Thermal Spallation

The influence of porosity on concrete spalling has been investigated by several researchers, however prior data are unavailable for basalt. [46, 164, 165] The porosity value of 15% was chosen as the midpoint of the range 10-20%. These are typical values for basalt, so to study the affect of porosity on simulation results, the simulation was run for 10% and 20% porosity. The results of these runs are close to the averages in Figure 5.14 and Figure 5.15.

The initial hypothesis for this study was that a higher porosity would lead to faster spallation. The material is weaker, so it should fail more readily. However, the presence of pores allows the material to expand more freely. The traction-free boundaries result in less stress at the grain boundaries. The impact of weakening the material by increasing porosity is countered by the ability of grains to expand freely at their traction-free boundaries.

5.4 Summary of Results

The first set of results validate the simulation with experimental measurements of Barre granite. Overall the results match to within 15-20%, which is within the expected range for geological materials. The semi-infinite solid model accurately represents the general trend in results. The direct numerical simulation approach provides greater detail about thermal spallation, compared to an analytic model. First, it captures the variability of output quantities such as the spall temperature. Second, the full history of every variable is available at every point in the domain. This level of detail leads to insights into the thermal spallation phenomenon. For example, the eigenstress arises from dissimilar mineral properties, anisotropy, and crystal lattice misorientation. The numerical model of thermal spallation is valid for granite in the range of experimental data available and provides new insights into the spallation process.

The second set of results demonstrate that the simulation can be used to predict spallation in Martian basalt. The primary driver of spallation in basalt is the misorientation of its anisotropic mineral components. The poor heat capacity and thermal conductivity lead to a reduction in recession rate compared to granite. Pores in the material create an complex stress pattern, and surprisingly the recession rates and surface temperatures do not change significantly with porosity in the basalt. The estimated recession rates can be used in conjunction with CFD to produce an approximation of the recession depth profile at the landing site.

CHAPTER 6
CONCLUSIONS

6.1 Summary

The thermal spallation process occurs when a high heat flux is applied to brittle materials. This includes concrete structures in a fire, vertical take off and landing aircraft, and propulsive landing on other planets. Experiments provide useful insights into the physics of spallation, however in some cases a sample of the material cannot be obtained or tested.

To predict this phenomenon *a priori*, the governing equations of thermoelasticity are solved numerically on a mesh of the material microstructure. This synthetic microstructure has the same composition and grain size distribution as the material, with cohesive zones at the grain interfaces for damage evolution. Grains in the microstructure are assigned lattice orientations and given fully anisotropic and temperature-dependent material properties. With this level of fidelity at the grain scale, the solution to the thermoelastic governing equations matches experimental results for Barre granite to within experimental uncertainty.

This validated model is used to predict spallation of Martian basalt for a range of heat flux values. These results indicate that the recession rates remain below 1 mm/s overall, though there is some 15-20% uncertainty based on the nature of geological materials. The functional relationship between recession rate and heat flux can be used to estimate the erosion pattern for propulsive landers by post-processing CFD results. A profile of heat flux over time at a given point in the landing zone can be converted into a profile of recession rate over time. The total depth of erosion at each point in the landing zone can be determined by integrating that recession rate profile. This numerical simulation of the thermal spallation process can be used to predict the response of materials that cannot be

tested experimentally.

6.2 Key Findings

6.2.1 Synthetic Microstructure Generation

The algorithm presented in chapter 4 is capable of modeling microstructures with multiple material phases including amorphous phases, spherical and non-spherical grains, voids, rectangular and non-rectangular domains, and arbitrary distributions for grain size, shape, orientation, and position. The resulting mesh instances show excellent agreement between the input and output microstructures. Volume fractions match to within 0.01 for circular and spherical grains, and within 0.03 for ellipsoidal grains. Grain size distributions agree with $R^2 > 0.93$ and volume distributions with $R^2 > 0.95$.

6.2.2 Direct Numerical Simulation of Thermal Spallation

The results presented in chapter 5 show that the numerical simulation can predict the recession rate and spallation temperature to within 20%. This level of accuracy is appropriate for geological materials, which can have over 30% error in their material properties. Additionally, the temperature and stress fields computed during the solution process can provide insights into the mechanisms driving thermal spallation. The validated simulation was also applied to Martian basalt. Results are limited since the material failed to spall at lower heat fluxes. The higher heat flux values indicate that the recession rate in basalt is approximately half that of granite. The difference between these results is attributed to the dissimilar volumetric heat capacity. Results from this study could be used in conjunction with CFD to estimate the recession depth profile at a propulsive Mars landing site.

6.3 Future Work

The author recommends seven areas of future work that would improve the numerical simulation of thermal spallation. First, when computing power becomes available, the simulation should be run in 3D. The simulation results presented in this paper use 2D plane strain due to limitations in modern computer power. Plane strain is consistent with crack propagation simulations, however in the case of polycrystals, each grain has an axis perpendicular to the plane. In a 3D simulation, the grain orientations can be purely random. The methods described in this thesis are general for both 2D and 3D, so no modifications would be needed when 3D DNS of statistically representative RVEs is possible.

The second recommendation is to replace the unstructured triangular mesh with polygonal elements. The shape functions for polygonal elements have already been derived, and they would significantly reduce the number of degrees of freedom required. MicroStructPy outputs convex polygons for each grain, then meshes those grains with triangles. The triangular meshing step could be skipped if the simulation used polygonal elements. This simulation would require significantly fewer degrees of freedom for each grain if polygonal elements were used.

The third recommendation is to apply a discount factor to mineral material properties. Dislocations and flaws in the crystal lattices can reduce the heat capacity and stiffness of the grains. The effect of flaws on thermal inertia are captured by the transient heating curve, however data are not available to split the thermal inertia into the thermal conductivity and volumetric heat capacity. Additional heating data would allow for these two quantities to be estimated independently. Better numerical representation of a microstructure could be achieved by including a discount factor within the grains, along with contact conductance at the grain boundaries.

The fourth recommendation is to include pre-stress in the microstructure of geological materials. Basalts cool rapidly, which results in stress concentrations. Tectonic activity also

puts stress on the material before heat is applied. These two factors result in a pre-stress state that would change the evolution of thermal spallation in the material. The simulation process described in this thesis would not change when pre-stress is added, only the initial conditions of the mechanical analysis.

The fifth recommendation for future work is to add water to the pores in the microstructure. This could be either solid or liquid water, however the high heat from thermal spallation would convert the water to steam. Steam would apply pressure to the pore walls and change the stress distribution within the material. To incorporate this pore pressure, the temperature of each surface element could be calculated during the thermal post-processing step. The mechanical pre-processor would apply pressure to each surface element based on temperature. The presence of water in the pores can be incorporated by modifying the thermal post-processor and mechanical pre-processor.

The sixth recommendation for future work is to apply the thermal spallation simulation to sedimentary conglomerates. The Mars *Curiosity* rover landed on a fluvial conglomerate, which was direct evidence of flowing water on ancient Mars. These rocks are made of smooth pebbles cemented in a fine, sedimentary matrix. Some significant modifications to the simulation framework would be required to accurately simulate this material since it is not polycrystalline. MicroStructPy can create the microstructure of a conglomerate, where the cementing material would be a matrix phase. The challenge would be modeling fracture in the matrix. One possibility is to insert cohesive elements throughout the matrix, which would be a minor modification to the mesh generator. This would pre-define the fracture paths in the cement and ultimately increase the fracture energy of the material. The XFEM approach may be more suitable to sedimentary conglomerates, as an alternative to cohesive zones.

The seventh and final recommendation for future work is to perform an uncertainty analysis on the recession rate predicted for Martian basalt. The 15-20% error reported for Barre granite is primarily epistemic, meaning that the material and its conditions are known

well so the error can be attributed to the modeling process. Martian basalt material properties are not known with the same degree of certainty and they vary by location across the planet. This increase in aleatory uncertainty would therefore increase the overall uncertainty in the basalt results, compared to those for granite. To quantify this uncertainty, key parameters could be varied in a Monte Carlo simulation. These parameters include the composition, yield strength, fracture energy, and contact conductance of the material. The means and variances of these distributions could be informed by the observations from the Mars Exploration Rovers, Mars Science Laboratory, and Mars 2020 rover missions.

Appendices

APPENDIX A

LIST OF PUBLICATIONS BY THE AUTHOR

[1] K. A. Hart and J. J. Rimoli, "Direct numerical simulation of thermal spallation in granite (in preparation)," 2021.

[2] ——, "MicroStructPy: A statistical microstructure mesh generator in Python," *SoftwareX*, vol. 12, p. 100 595, 2020.

[3] ——, "Generation of statistically representative microstructures with direct grain geometry control," *Computer Methods in Applied Mechanics and Engineering*, vol. 370, 2020.

[4] D. S. Groesbeck, K. A. Hart, and B. C. Gunter, "Simulated formation flight of nanosatellites using differential drag with high-fidelity rarefied aerodynamics," *Journal of Guidance, Control, and Dynamics*, vol. 42, no. 5, pp. 1175–1184, 2019.

[5] D. S. Groesbeck, B. C. Gunter, and K. A. Hart, "Simulated formation control maneuvers for the RANGE CubeSat mission," in *AAS/AIAA Astrodynamics Specialist Conference*, Stevenson, WA, 2017.

[6] K. A. Hart, K. R. Simonis, B. A. Steinfeldt, and R. D. Braun, "Analytic free-molecular aerodynamics for rapid propagation of resident space objects," *Journal of Spacecraft and Rockets*, vol. 55, no. 1, pp. 27–36, 2017.

[7] K. A. Hart, B. C. Gunter, and R. D. Braun, "Aerodynamics of the RANGE nanosatellites from direct flowfield simulation," in *AIAA SPACE 2016*, Long Beach, CA, 2016.

[8] K. A. Hart, B. A. Steinfeldt, and R. D. Braun, "Formulation and applications of a probabilistic Pareto chart," in *56th AIAA/ASCE/AHS/ASC Structures, Structural Dynamics, and Materials Conference*, Kissimmee, FL, 2015.

[9] K. A. Hart, K. R. Simonis, B. A. Steinfeldt, and R. D. Braun, "Analytical aerodynamic force and moment coefficients of axisymmetric objects in rarefied flow," in *AIAA Atmospheric Flight Mechanics Conference*, Kissimmee, FL, 2015.

[10] K. Hart and K. A. Bostroem, "Characterization of the STIS NUV MAMA vignetting by optical element," Space Telescope Science Institute, Baltimore, MD, Tech. Rep., 2014, pp. 1–19.

[11] K. A. Hart, K. R. Simonis, S. Dutta, B. A. Steinfeldt, and R. D. Braun, "Analytically-derived aerodynamic force and moment coefficients of resident space objects in free-molecular flow," in *AIAA Atmospheric Flight Mechanics Conference*, National Harbor, MD, 2014.

REFERENCES

[1] Air Force Civil Engineering Support Agency, "Engineering Technical Letter (ETL) 14-2 (Change 1): Preventing and Repairing Concrete Deteriotation Under MV-22 and CV-22 Aircraft," Department of the Air Force, Tyndall AFB, FL, Tech. Rep., 2014, pp. 1–10.

[2] National Aeronautics and Space Administration, "2015 NASA Technology Roadmaps," Tech. Rep., 2015.

[3] P. T. Metzger, C. D. Immer, C. M. Donahue, B. M. Vu, R. C. Latta, and M. Deyo-Svendsen, "Jet-induced cratering of a granular surface with application to lunar spaceports," *Journal of Aerospace Engineering*, vol. 22, no. 1, pp. 24–32, 2009.

[4] C. D. Immer, P. T. Metzger, P. E. Hintze, A. Nick, and R. Horan, "Apollo 12 Lunar Module exhaust plume impingement on lunar Surveyor III," *Icarus*, vol. 211, no. 2, pp. 1089–1102, 2011.

[5] M. Mehta *et al.*, "Explosive erosion during the Phoenix landing exposes subsurface water on Mars," *Icarus*, vol. 211, no. 1, pp. 172–194, Jan. 2011.

[6] A. Sengupta, J. Kulleck, S. Sell, J. W. Van Norman, M. Mehta, and M. Pokora, "Mars lander engine plume impingement environment of the Mars Science Laboratory," in *IEEE Aerospace Conference*, Big Sky, MT, Mar. 2009.

[7] J. Vizcaino and M. Mehta, "Quantification of plume-soil interaction and excavation due to the Mars Science Laboratory Sky Crane descent phase," in *8th Symposium on Space Resource Utilization*, Kissimmee, Florida, 2015.

[8] J. Sachdev, V. Ahuja, A. Hosangadi, and D. Allgood, "Analysis of flame deflector spray nozzles in rocket engine test stands," in *46th AIAA/ASME/SAE/ASEE Joint Propulsion Conference & Exhibit*, Nashville, Tennessee, 2010.

[9] P. A. Liever, M. P. Gale, R. S. Mehta, and J. S. West, "Gas-granular simulation framework for spacecraft landing plume-surface interaction and debris transport analysis," in *ASCE Earth & Space*, Cleveland, Ohio, 2018, pp. 39–48.

[10] K. Balakrishnan and J. Bellan, "High-fidelity modeling and numerical simulation of cratering induced by the interaction of a supersonic jet with a granular bed of solid particles," *International Journal of Multiphase Flow*, vol. 99, pp. 1–29, 2018.

[11] J. Marichalar, A. Prisbell, F. Lumpkin, and G. LeBeau, "Study of plume impingement effects in the lunar lander environment," in *AIP Conference Proceedings*, American Institute of Physics, vol. 1333, 2011, pp. 589–594.

[12] A. Rahimi, O. Ejtehadi, K. Lee, and R. Myong, "Near-field plume-surface interaction and regolith erosion and dispersal during the lunar landing," *Acta Astronautica*, vol. 175, pp. 308–326, 2020.

[13] P. T. Metzger, J. E. Lane, C. D. Immer, and S. Clements, "Cratering and blowing soil by rocket engines during lunar landings," in *Sixth International Conference on Case Geotechnical Engineering*, 2008, pp. 1–12.

[14] J. Regele, J. Rabinovitch, T. Colonius, and G. Blanquart, "Unsteady effects in dense, high speed, particle laden flows," *International Journal of Multiphase Flow*, vol. 61, pp. 1–13, 2014.

[15] J. C. Branner, "Decomposition of rocks in Brazil," *Bulletin of the Geological Society of America*, vol. 7, no. 1, pp. 255–314, 1895.

[16] J. L. Molaro, S. Byrne, and S. A. Langer, "Grain-scale thermoelastic stresses and spatiotemporal temperature gradients on airless bodies, implications for rock breakdown," *Journal of Geophysical Research: Planets*, vol. 120, no. 2, pp. 255–277, 2015.

[17] D. Filges and F. Goldenbaum, "Handbook of spallation research," *Resonance*, vol. 1, pp. 5–2, 2009.

[18] J. N. Johnson, "Dynamic fracture and spallation in ductile solids," *Journal of Applied Physics*, vol. 52, no. 4, pp. 2812–2825, 1981.

[19] J. Lundell, "Spallation of the Galileo probe heat shield," in *3rd Joint Thermophysics, Fluids, Plasma and Heat Transfer Conference*, 1982, p. 852.

[20] S. D. Walsh and I. N. Lomov, "Micromechanical modeling of thermal spallation in granitic rock," *International Journal of Heat and Mass Transfer*, vol. 65, pp. 366–373, 2013.

[21] F. W. Preston, "The spalling of bricks," *Journal of the American Ceramic Society*, vol. 9, no. 10, pp. 654–658, 1926.

[22] F. W. Preston and H. E. White, "Observations on spalling," *Journal of the American Ceramic Society*, vol. 17, no. 1-12, pp. 137–144, 1934.

[23] A. Leitner, "The fire catastrophe in the Tauern Tunnel: Experience and conclusions for the Austrian guidelines," *Tunnelling and Underground Space Technology*, vol. 16, no. 3, pp. 217–223, 2001.

[24] R. M. Rauenzahn, "Analysis of rock mechanics and gas dynamics of flame-jet thermal spallation drilling," Ph.D. dissertation, Massachusetts Institute of Technology, 1986.

[25] R. M. Rauenzahn and J. W. Tester, "Numerical simulation and field testing of flame-jet thermal spallation drilling-1. model development," *International Journal of Heat and Mass Transfer*, vol. 34, no. 3, pp. 795–808, 1991.

[26] ——, "Numerical simulation and field testing of flame-jet thermal spallation drilling-2. experimental verification," *International Journal of Heat and Mass Transfer*, vol. 34, no. 3, pp. 809–818, 1991.

[27] S. A. Austin, P. J. Robins, and M. R. Richards, "Jet-blast temperature-resistant concrete for Harrier aircraft pavements," *The Structural Engineer*, vol. 70, no. 23, pp. 427–432, 1992.

[28] M. C. Hironaka and L. J. Malvar, "Jet exhaust damaged concrete," *Concrete International*, vol. 20, no. 10, pp. 32–35, 1998.

[29] J. G. Mantovani, G. J. Tamasy, R. P. Mueller, I. I. Townsend, J. W. Sampson, and M. A. Lane, "Launch pad in a box," in *ASCE Earth & Space*, Orlando, FL, 2016, pp. 960–971.

[30] R. E. Williams, "The thermal spallation drilling process," *Geothermics*, vol. 15, no. 1, pp. 17–22, 1986.

[31] D. Höser, "Flame-jet assisted drilling technology," Ph.D. dissertation, ETH Zurich, 2016.

[32] M. A. Kant, E. Rossi, C. Madonna, D. Höser, and P. R. von Rohr, "A theory on thermal spalling of rocks with a focus on thermal spallation drilling," *Journal of Geophysical Research: Solid Earth*, vol. 122, pp. 1805–1815, 2017.

[33] M. A. Kant, E. Rossi, D. Höser, and P. R. von Rohr, "Thermal spallation drilling , an alternative drilling technology for deep heat mining - performance analysis , cost assessment and design aspects," *Proceedings, 42nd Workshop on Geothermal Reservoir Engineering*, 2017.

[34] I. Beentjes, J. T. Bender, A. J. Hawkins, and J. W. Tester, "Chemical dissolution drilling of Barre granite using a sodium hydroxide enhanced supercritical water jet," *Rock Mechanics and Rock Engineering*, vol. 53, no. 2, pp. 483–496, 2020.

[35] C. R. Augustine, "Hydrothermal spallation drilling and advanced energy conversion technologies for engineered geothermal systems," Ph.D. dissertation, Massachusetts Institute of Technology, 2009.

[36] M. A. Kant, D. Becker, D. Brkic, T. Meier, M. Schuler, and P. R. von Rohr, "Investigation of a novel drilling technology–influence of the surface temperature for hydrothermal spallation drilling," in *Proceedings World Geothermal Congress, Melbourne, Australia*, 2015, pp. 19–25.

[37] I. Beentjes, J. T. Bender, S. D. Hillson, and J. W. Tester, "Hydrothermal spallation of Barre granite using supercritical water jets," in *Proceedings, 43rd workshop on Geothermal Reservoir Engineering Stanford University, Stanford, California*, 2018.

[38] M. A. Wilkinson, "Computational modeling of the gas-phase transport phenomena and experimental investigation of surface temperatures during flame-jet thermal spallation drilling," Ph.D. dissertation, Massachusetts Institute of Technology, 1989, p. 273.

[39] F. Autelitano, C. Iacci, and F. Giuliani, "Thermomechanical behaviour of airfield concrete pads supporting joint strike fighter F-35B," *Road Materials and Pavement Design*, vol. 18, no. 5, pp. 1027–1048, 2017.

[40] P. Robins, S. Austin, and M. Richards, "The resistance of steel fibre concrete to VTOL engine jet blast," *Cement and Concrete Composites*, vol. 16, no. 1, pp. 57–64, 1994.

[41] C.-G. Han, Y.-S. Hwang, S.-H. Yang, and N. Gowripalan, "Performance of spalling resistance of high performance concrete with polypropylene fiber contents and lateral confinement," *Cement and concrete research*, vol. 35, no. 9, pp. 1747–1753, 2005.

[42] T. Ecker, F. Zilker, E. Dumont, S. Karl, and K. Hannemann, "Aerothermal analysis of reusable launcher systems during retro-propulsion reentry and landing," in *Space Propulsion*, Seville, Spain: Association Aéronautique et Astronautique de France, 2018, pp. 1–12.

[43] J. A. Dec, "Three dimensional finite element ablative thermal response analysis applied to heatshield penetration design," Ph.D. dissertation, Georgia Institute of Technology, 2010.

[44] K. T. Edquist *et al.*, "Mars science laboratory entry capsule aerothermodynamics and thermal protection system," in *2007 IEEE Aerospace Conference*, IEEE, 2007, pp. 1–13.

[45] M. H. H. Hettema, "The thermo-mechanical behavior of sedimentary rock: An experimental study," Ph.D. dissertation, Delft University of Technology, 1996.

[46] P. Kalifa, F. D. Menneteau, and D. Quenard, "Spalling and pore pressure in HPC at high temperatures," *Cement and Concrete Research*, vol. 30, no. 12, pp. 1915–1927, 2000.

[47] G. A. Khoury, "Effect of fire on concrete and concrete structures," *Progress in Structural Engineering and Materials*, vol. 2, pp. 429–447, 2002.

[48] W. J. Copier, "The spalling of normal weight and lightweight concrete exposed to fire," in *Fire Safety of Concrete Structures. Papers presented at the Fall Convention of the American Concrete Institute.*, 1983.

[49] X. Hu, X. Song, Y. Liu, G. Li, Z. Shen, and Z. Lyu, "Aspect ratio of spalls of granite in flame-jet spallation and its effect on the modeling prediction of spallation properties," *Journal of Petroleum Science and Engineering*, vol. 171, pp. 1390–1399, 2018.

[50] R. E. Williams, R. M. Potter, and S. Miska, "Experiments in thermal spallation of various rocks," *Journal of Energy Resources Technology*, vol. 118, no. 1, pp. 2–8, Mar. 1996.

[51] I. Beentjes, "Dissolution and thermal spallation of Barre granite using pure and chemically enhanced hydrothermal jets," M.S. thesis, Cornell University, 2018.

[52] G. N. Ahmed and J. P. Hurst, "An analytical approach for investigating the causes of spalling of high-strength concrete at elevated temperatures," in *Proceedings of the International Workshop on Fire Performance of High-Strength Concrete*, 1997.

[53] Y. Msaad and G. Bonnet, "Analyses of heated concrete spalling due to restrained thermal dilation: Application to the "Chunnel" fire," *Journal of Engineering Mechanics*, vol. 132, no. 10, pp. 1124–1132, 2006.

[54] T. Saksala, "Numerical modelling of thermal spallation of rock," in *Proceedings of XII Argentine Congress on Computational Mechanics*, Yerba Buena, Argentina: Mecánica Computacional, 2018, pp. 1567–1574.

[55] S. D. Walsh, I. Lomov, and J. J. Roberts, "Geomechanical modeling for thermal spallation drilling," Lawrence Livermore National Laboratory, Livermore, CA, Tech. Rep. LLNL-PROC-483098, 2011.

[56] ——, "Grain-scale failure in thermal spallation drilling," Lawrence Livermore National Laboratory, Livermore, CA, Tech. Rep. LLNL-CONF-523558, 2012.

[57] J. Baird, B. Caskey, M. Tinianow, and C. Stone, "GEODYN: A geological formation/drillstring dynamics computer program," in *SPE Annual Technical Conference and Exhibition*, Sep. 1984.

[58] M. A. Kant and P. R. von Rohr, "Minimal required boundary conditions for the thermal spallation process of granitic rocks," *International journal of rock mechanics and mining sciences*, vol. 84, pp. 177–186, 2016.

[59] M. Mehta, A. Sengupta, N. O. Renno, J. W. Van Norman, P. G. Huseman, and D. S. Gulick, "Underexpanded supersonic plume surface interactions: Applications for spacecraft landings on planetary bodies," in *58th JANNAF Interagency Propulsion Committee Conference*, Arlington, VA, Apr. 2011.

[60] H. W. Price, R. D. Braun, R. Manning, and E. Sklyanski, "A high-heritage blunt-body entry, descent, and landing concept for human Mars exploration," in *54th AIAA Aerospace Sciences Meeting*, San Diego, CA, Jan. 2016.

[61] H. Y. McSween *et al.*, "Characterization and petrologic interpretation of olivine-rich basalts at Gusev Crater, Mars," *Journal of Geophysical Research: Planets*, vol. 111, no. E02S10, pp. 1–17, 2006.

[62] Z. Bieniawski, "Mechanism of brittle fracture of rock: Part I—theory of the fracture process," *International Journal of Rock Mechanics and Mining Sciences & Geomechanics Abstracts*, vol. 4, no. 4, pp. 395–406, 1967.

[63] C. A. Coulomb, *Essai sur une application des règles de maximis et minimis à quelques problèmes de statique, relatifs à l'architecture*. Paris: L'Imprimerie Royale, 1776, pp. 343–387.

[64] O. Mohr *et al.*, "Welche umstände bedingen die elastizitätsgrenze und den bruch eines materials," *Zeitschrift des Vereins Deutscher Ingenieure*, vol. 46, no. 1524-1530, pp. 1572–1577, 1900.

[65] E. Hoek and E. T. Brown, "Empirical strength criterion for rock masses," *Journal of the geotechnical engineering division*, vol. 106, no. 9, pp. 1013–1035, 1980.

[66] ——, "Practical estimates of rock mass strength," *International journal of rock mechanics and mining sciences*, vol. 34, no. 8, pp. 1165–1186, 1997.

[67] N. Lundborg, "The strength-size relation of granite," in *International Journal of Rock Mechanics and Mining Sciences & Geomechanics Abstracts*, vol. 4, 1967, pp. 269–272.

[68] Y.-j. Shen, J.-s. Hao, X. Hou, J.-q. Yuan, and Z.-p. Bai, "Crack propagation in high-temperature granite after cooling shock: Experiment and numerical simulation," *Bulletin of Engineering Geology and the Environment*, pp. 1–14, 2021.

[69] M. Saadat and A. Taheri, “A numerical approach to investigate the effects of rock texture on the damage and crack propagation of a pre-cracked granite,” *Computers and Geotechnics*, vol. 111, pp. 89–111, 2019.

[70] V. Ghiasi, H. Omar, Z. B. M. Yusoff, B. K. Huat, R. Muniandy, and M. N. Alias, “A new model of microcracks propagation in granite rock,” *Australian Journal of Basic and Applied Sciences*, pp. 1–22, 2010.

[71] M. Elices, G. Guinea, J. Gomez, and J. Planas, “The cohesive zone model: Advantages, limitations and challenges,” *Engineering fracture mechanics*, vol. 69, no. 2, pp. 137–163, 2002.

[72] D. S. Dugdale, “Yielding of steel sheets containing slits,” *Journal of the Mechanics and Physics of Solids*, vol. 8, no. 2, pp. 100–104, 1960.

[73] G. I. Barenblatt, “The mathematical theory of equilibrium cracks in brittle fracture,” in *Advances in applied mechanics*, vol. 7, Elsevier, 1962, pp. 55–129.

[74] J. R. Rice *et al.*, “Mathematical analysis in the mechanics of fracture,” *Fracture: an advanced treatise*, vol. 2, pp. 191–311, 1968.

[75] S. M. Wahid and C. Madhusudana, “Gap conductance in contact heat transfer,” *International Journal of Heat and Mass Transfer*, vol. 43, no. 24, pp. 4483–4487, 2000.

[76] N. Moës and T. Belytschko, “Extended finite element method for cohesive crack growth,” *Engineering fracture mechanics*, vol. 69, no. 7, pp. 813–833, 2002.

[77] A. F. Bower, *Applied mechanics of solids*. CRC press, 2009.

[78] P.-O. Bouchard, F. Bay, and Y. Chastel, “Numerical modelling of crack propagation: Automatic remeshing and comparison of different criteria,” *Computer Methods in Applied Mechanics and Engineering*, vol. 192, no. 35-36, pp. 3887–3908, 2003.

[79] D. W. Spring, S. E. Leon, and G. H. Paulino, “Unstructured polygonal meshes with adaptive refinement for the numerical simulation of dynamic cohesive fracture,” *International Journal of Fracture*, vol. 189, no. 1, pp. 33–57, 2014.

[80] R. H. Pletcher, J. C. Tannehill, and D. Anderson, *Computational fluid mechanics and heat transfer*. CRC press, 2012.

[81] K. A. Hart and J. J. Rimoli, “Generation of statistically representative microstructures with direct grain geometry control,” *Computer Methods in Applied Mechanics and Engineering*, vol. 370, 2020.

[82] ——, "MicroStructPy: A statistical microstructure mesh generator in Python," *SoftwareX*, vol. 12, p. 100 595, 2020.

[83] G. Marsaglia, "Choosing a point from the surface of a sphere," *The Annals of Mathematical Statistics*, vol. 43, no. 2, pp. 645–646, 1972.

[84] S. Nemat-Nasser and M. Hori, *Micromechanics: Overall Properties of Heterogeneous Materials*, 2nd ed. Amsterdam, The Netherlands: North Holland, 1999.

[85] S. Torquato, *Random Heterogeneous Materials: Microstructure and Macroscopic Properties*. New York: Springer Science and Business Media, 2013.

[86] J. D. Eshelby, "The determination of the elastic field of an ellipsoidal inclusion, and related problems," *Proceedings of the Royal Society A: Mathematical, Physical and Engineering Sciences*, vol. 241, no. 1226, pp. 376–396, 1957.

[87] R. Hill, "A self-consistent mechanics of composite materials," *Journal of the Mechanics and Physics of Solids*, vol. 13, no. 4, pp. 213–222, 1965.

[88] N. J. Pagano, "Exact solutions for rectangular bidirectional composites and sandwich plates," *Journal of Composite Materials*, vol. 4, no. 1, pp. 20–34, 1970.

[89] T. Mori and K. Tanaka, "Average stress in matrix and average elastic energy of materials with misfitting inclusions," *Acta Metallurgica*, vol. 21, no. 5, pp. 571–574, 1973.

[90] M. Maldovan, "Micro to nano scale thermal energy conduction in semiconductor thin films," *Journal of Applied Physics*, vol. 110, no. 3, pp. 034308–1–6, 2011.

[91] J.-B. P. Bouquet and J. J. Rimoli, "A length-dependent model for the thermomechanical response of ceramics," *Journal of the Mechanics and Physics of Solids*, vol. 82, pp. 82–96, 2015.

[92] S. G. Lekhnitskiy, "The plane problem of the theory of elasticity of an anisotropic body," in *Anisotropic Plates*, 2nd ed., Moskow: Gosudarstvennoye Izdatel'stvo Tekhniko-Teoreticheskoy Literatury, 1957, pp. 26–58.

[93] R. J. Asaro and A. Needleman, "Texture development and strain hardening in rate dependent polycrystals," *Acta Metallurgica*, vol. 33, no. 6, pp. 923–953, 1985.

[94] G. M. Friedman, "On sorting, sorting coefficients, and the lognormality of the grain-size distribution of sandstones," *The Journal of Geology*, vol. 70, no. 6, pp. 737–753, 1962.

[95] B. D. Marsh, "Crystal size distribution (CSD) in rocks and the kinetics and dynamics of crystallisation I. Theory," *Contributions to Mineralogy and Petrology*, vol. 99, no. 3, pp. 277–291, 1988.

[96] M. Groeber, S. Ghosh, M. D. Uchic, and D. M. Dimiduk, "A framework for automated analysis and simulation of 3D polycrystalline microstructures. Part 1: Statistical characterization," *Acta Materialia*, vol. 56, no. 6, pp. 1257–1273, 2008.

[97] ——, "A framework for automated analysis and simulation of 3D polycrystalline microstructures. Part 2: Synthetic structure generation," *Acta Materialia*, vol. 56, no. 6, pp. 1274–1287, 2008.

[98] W. Ludwig *et al.*, "Three-dimensional grain mapping by x-ray diffraction contrast tomography and the use of Friedel pairs in diffraction data analysis," *Review of Scientific Instruments*, vol. 80, no. 033905, pp. 1–9, 2009.

[99] J. C. Ferguson, F. Panerai, A. Borner, and N. N. Mansour, "PuMA: The porous microstructure analysis software," *SoftwareX*, vol. 7, pp. 81–87, 2018.

[100] B. L. Adams, M. Lyon, B. Henrie, S. R. Kalidindi, and H. Garmestani, "Spectral integration of microstructure and design," *Materials Science Forum*, vol. 408, pp. 487–492, 2002.

[101] G. Saheli, H. Garmestani, and B. L. Adams, "Microstructure design of a two phase composite using two-point correlation functions," *Journal of Computer-Aided Materials Design*, vol. 11, no. 2-3, pp. 103–115, 2004.

[102] D. T. Fullwood, S. R. Niezgoda, and S. R. Kalidindi, "Microstructure reconstructions from 2-point statistics using phase-recovery algorithms," *Acta Materialia*, vol. 56, no. 5, pp. 942–948, 2008.

[103] A. Cecen, Y. C. Yabansu, and S. R. Kalidindi, "A new framework for rotationally invariant two-point spatial correlations in microstructure datasets," *Acta Materialia*, vol. 158, pp. 53–64, 2018.

[104] F. Aurenhammer, "Voronoi diagrams - a survey of a fundamental geometric data structure," *ACM Computing Surveys*, vol. 23, no. 3, pp. 345–405, 1991.

[105] J. J. Rimoli and M. Ortiz, "A duality-based method for generating geometric representations of polycrystals," *International Journal for Numerical Methods in Engineering*, vol. 86, no. 9, pp. 1069–1081, 2011.

[106] F. Aurenhammer, "Power diagrams: Properties, algorithms and applications," *SIAM Journal on Computing*, vol. 16, no. 1, pp. 78–96, Feb. 1987.

[107] R. Quey and L. Renversade, "Optimal polyhedral description of 3D polycrystals: Method and application to statistical and synchrotron X-ray diffraction data," *Computer Methods in Applied Mechanics and Engineering*, vol. 330, pp. 308–333, 2018.

[108] Z. Fan, Y. Wu, X. Zhao, and Y. Lu, "Simulation of polycrystalline structure with Voronoi diagram in Laguerre geometry based on random closed packing of spheres," *Computational Materials Science*, vol. 29, no. 3, pp. 301–308, 2004.

[109] S. Ghosh, K. Lee, and S. Moorthy, "Multiple scale analysis of heterogeneous elastic structures using homogenization theory and Voronoi cell finite element method," *International Journal of Solids and Structures*, vol. 32, no. 1, pp. 27–62, 1995.

[110] S. Swaminathan, S. Ghosh, and N. J. Pagano, "Statistically equivalent representative volume elements for unidirectional composite microstructures: Part I - Without damage," *Journal of Composite Materials*, vol. 40, no. 7, pp. 583–604, 2006.

[111] C. Redenbach, "Microstructure models for cellular materials," *Computational Materials Science*, vol. 44, no. 4, pp. 1397–1407, 2009.

[112] E. Ghazvinian, M. S. Diederichs, and R. Quey, "3D random Voronoi grain-based models for simulation of brittle rock damage and fabric-guided micro-fracturing," *Journal of Rock Mechanics and Geotechnical Engineering*, vol. 6, no. 6, pp. 506–521, 2014.

[113] D. N. Ilin and M. Bernacki, "Advancing layer algorithm of dense ellipse packing for generating statistically equivalent polygonal structures," *Granular Matter*, vol. 18, no. 3, p. 43, 2016.

[114] S. Falco, J. Jiang, F. De Cola, and N. Petrinic, "Generation of 3D polycrystalline microstructures with a conditioned Laguerre-Voronoi tessellation technique," *Computational Materials Science*, vol. 136, pp. 20–28, 2017.

[115] G. van den Bergen, "Efficient collision detection of complex deformable models using AABB trees," *Journal of Graphics Tools*, vol. 2, no. 4, pp. 1–13, 1997.

[116] D. Markauskas, R. Kačianauskas, A. Džiugys, and R. Navakas, "Investigation of adequacy of multi-sphere approximation of elliptical particles for DEM simulations," *Granular Matter*, vol. 12, no. 1, pp. 107–123, 2010.

[117] C. H. Rycroft, "VORO++: A three-dimensional Voronoi cell library in C++," *Chaos: An Interdisciplinary Journal of Nonlinear Science*, vol. 19, no. 4, p. 041 111, 2009.

[118] J. R. Shewchuk, "Triangle: Engineering a 2D quality mesh generator and Delaunay triangulator," in *Applied computational geometry towards geometric engineering*, M. C. Lin and D. Manocha, Eds., Berlin: Springer, 1996, pp. 203–222.

[119] H. Si, "TetGen, a Delaunay-based quality tetrahedral mesh generator," *ACM Transactions on Mathematical Software*, vol. 41, no. 2, p. 11, 2015.

[120] N. Hansen, "Cold deformation microstructures," *Materials Science and Technology (United Kingdom)*, vol. 6, no. 11, pp. 1039–1047, 1990.

[121] M. Voutilainen *et al.*, "Characterization of spatial porosity and mineral distribution of crystalline rock using X-ray micro computed tomography, C-14-PMMA autoradiography and scanning electron microscopy," *Applied Geochemistry*, vol. 101, pp. 50–61, 2019.

[122] S. P. Morgan, C. A. Johnson, and H. H. Einstein, "Cracking processes in Barre granite: Fracture process zones and crack coalescence," *International journal of fracture*, vol. 180, no. 2, pp. 177–204, 2013.

[123] B. Q. Li and H. H. Einstein, "Comparison of visual and acoustic emission observations in a four point bending experiment on Barre granite," *Rock Mechanics and Rock Engineering*, vol. 50, no. 9, pp. 2277–2296, 2017.

[124] M. Nasseri, B. Mohanty, and R. Young, "Fracture toughness measurements and acoustic emission activity in brittle rocks," *Pure and Applied Geophysics*, vol. 163, no. 5, pp. 917–945, 2006.

[125] K. Xia, M. Nasseri, B. Mohanty, F. Lu, R. Chen, and S. Luo, "Effects of microstructures on dynamic compression of Barre granite," *International Journal of Rock Mechanics and Mining Sciences*, vol. 45, no. 6, pp. 879–887, 2008.

[126] F. Dai, K. Xia, and M. Nasseri, "Micromechanical model for the rate dependence of the fracture toughness anisotropy of Barre granite," *International Journal of Rock Mechanics and Mining Sciences*, vol. 63, pp. 113–121, 2013.

[127] M. Wilkinson and J. Tester, "Experimental measurement of surface temperatures during flame-jet induced thermal spallation," *Rock mechanics and rock engineering*, vol. 26, no. 1, pp. 29–62, 1993.

[128] J. R. Smyth and T. C. McCormick, "Crystallographic data for minerals," in *Mineral Physics and Crystallography: A Handbook of Physical Constants 2*, T. J. Ahrens, Ed., Washington, DC: American Geophysical Union, 1995, pp. 1–17.

[129] J. D. Bass, "Elasticity of minerals, glasses, and melts," in *Mineral Physics and Crystallography: A Handbook of Physical Constants 2*, T. J. Ahrens, Ed., Washington, DC: American Geophysical Union, 1995, pp. 45–63.

[130] J. M. Brown, R. J. Angel, and N. L. Ross, "Elasticity of plagioclase feldspars," *Journal of Geophysical Research: Solid Earth*, vol. 121, no. 2, pp. 663–675, 2016.

[131] I. Kukkonen and A. Lindberg, "Thermal properties of rocks at the investigation sites: Measured and calculated thermal conductivity, specific heat capacity, and thermal diffusivity," Geological Survey of Finland, Helsinki, Finland, Tech. Rep., 1998.

[132] R. A. Robie, B. S. Hemingway, and J. R. Fisher, "Thermodynamic properties of minerals and related substances at 298.15K and 1bar pressure and at higher temperatures," US Government Printing Office, Tech. Rep., 1978.

[133] K.-i. Horai, "Thermal conductivity of rock-forming minerals," *Journal of Geophysical Research*, vol. 76, no. 5, pp. 1278–1308, 1971.

[134] Y. Fei, "Thermal expansion," in *Mineral Physics and Crystallography: A Handbook of Physical Constants 2*, T. Ahrens, Ed., Washington, DC: American Geophysical Union, 1995, pp. 29–44.

[135] N. Waeselmann, J. M. Brown, R. J. Angel, N. Ross, J. Zhao, and W. Kaminsky, "The elastic tensor of monoclinic alkali feldspars," *American Mineralogist*, vol. 101, no. 5, pp. 1228–1231, 2016.

[136] S. Haussühl, "Thermoelastic properties of beryl, topaz, diaspore, sanidine and periclase," *Zeitschrift fur Kristallographie - Crystalline Materials*, vol. 204, no. 1-2, pp. 67–76, 1993.

[137] M. Höfer and F. R., "Heat transfer in quartz, orthoclase, and sanidine at elevated temperature," *Physics and Chemistry of Minerals*, vol. 29, no. 9, pp. 571–584, 2002.

[138] D. L. Lakshtanov, S. V. Sinogeikin, and J. D. Bass, "High-temperature phase transitions and elasticity of silica polymorphs," *Physics and Chemistry of Minerals*, vol. 34, no. 1, pp. 11–22, 2007.

[139] I. Ohno, K. Harada, and C. Yoshitomi, "Temperature variation of elastic constants of quartz across the α - β transition," *Physics and Chemistry of Minerals*, vol. 33, no. 1, pp. 1–9, 2006.

[140] E. C. Robertson, "Thermal properties of rocks," United States Department of the Interior, Tech. Rep. 88-441, Jan. 1988.

[141] J. A. Kosinski, J. G. Gualtieri, and A. Ballato, "Thermal expansion of alpha quartz," *IEEE Transactions on Ultrasonics, Ferroelectrtics, and Frequency Control*, vol. 39, no. 2, pp. 502–507, 1992.

[142] J. L. Rosenholtz and D. T. Smith, "Linear thermal expansion and inversion of quartz, var. rock crystal," *American Mineralogist*, vol. 26, no. 6, pp. 103–109, 1941.

[143] L. E. McNeil and M. Grimsditch, "Elastic moduli of muscovite mica," *Journal of Physics: Condensed Matter*, vol. 5, no. 11, pp. 1681–1690, 1993.

[144] D. Pribnow and T. Umsonst, "Estimation of thermal conductivity from the mineral composition: Influence of fabric and anisotropy," *Geophysical Research Letters*, vol. 20, no. 20, pp. 2199–2202, 1993.

[145] P. Hidnert and G. Dickson, "Some physical properties of mica," *Journal of Research of the National Bureau of Standards*, vol. 35, 1945.

[146] N. T. Coleman, F. H. Leroux, and J. G. Cady, "Biotite - hydrobiotite - vermiculite in soils," *Nature*, vol. 198, pp. 409–410, Apr. 1963.

[147] I. Song, M. Suh, Y.-K. Woo, and T. Hao, "Determination of the elastic modulus set of foliated rocks from ultrasonic velocity measurements," *Engineering Geology*, vol. 72, no. 3-4, pp. 293–308, 2004.

[148] F. Tutti, L. S. Dubrovinsky, and M. Nygren, "High-temperature study and thermal expansion of phlogopite," *Physics and Chemistry of Minerals*, vol. 27, no. 9, pp. 599–603, 2000.

[149] W. Goldsmith, J. L. Sackman, and C. Ewerts, "Static and dynamic fracture strength of Barre granite," *International Journal of Rock Mechanics and Mining Sciences and*, vol. 13, no. 11, pp. 303–309, 1976.

[150] D. E. Moore and D. A. Lockner, "The role of microcracking in shear-fracture propagation in granite," *Journal of Structural Geology*, vol. 7, no. 1, pp. 95–114, 1995.

[151] O. Panagouli, K. Margaronis, and V. Tsotoulidou, "A multiscale model for thermal contact conductance of rough surfaces under low applied pressure," *International Journal of Solids and Structures*, vol. 200-201, pp. 106–118, 2020.

[152] M. Cooper, B. Mikic, and M. Yovanovich, "Thermal contact conductance," *International Journal of Heat and Mass Transfer*, vol. 12, no. 3, pp. 279–300, 1969.

[153] C. A. Goodrich, "Petrogenesis of olivine-phyric shergottites Sayh al Uhaymir 005 and Elephant Moraine A79001 lithology A," *Geochimica et Cosmochimica Acta*, vol. 67, no. 19, pp. 3735–3772, 2003.

[154] K. V. Cashman and B. D. Marsh, "Crystal size distribution (CSD) in rocks and the kinetics and dynamics of crystallization II: Makaopuhi lava lake," *Contributions to Mineralogy and Petrology*, vol. 99, no. 3, pp. 292–305, Jul. 1988.

[155] D. W. Ming, private interview, Jul. 2016.

[156] K. Fujino, S. Sasaki, Y. Takeuchi, and R. Sadanaga, "X-ray determination of electron distributions in forsterite, fayalite and tephroite," *Acta Crystallographica Section B: Structural Crystallography and Crystal Chemistry*, vol. 37, no. 3, pp. 513–518, 1981.

[157] O. L. Anderson and D. G. Isaak, "Elastic constants of mantle minerals at high temperature," in *Mineral Physics and Crystallographic: A Handbook of Physical Constants*, T. J. Ahrens, Ed., 1995, pp. 64–97.

[158] I. Suzuki, "Thermal expansion of periclase and olivine, and their anharmonic properties," *Journal of Physics of the Earth*, 1975.

[159] D. G. Isaak, O. L. Anderson, T. Goto, and I. Suzuki, "Elasticity of single-crystal forsterite measured to 1700 K," *Journal of Geophysical Research: Solid Earth*, vol. 94, no. B5, pp. 5895–5906, 1989.

[160] Y. Sumino, O. Nishizawa, T. Goto, I. Ohno, and M. Ozima, "Temperature variation of elastic constants of single-crystal forsterite between -190° and 400° C," *Journal of Physics of the Earth*, vol. 25, no. 4, pp. 377–392, 1977.

[161] A. Navrotsky, "Thermodynamic properties of minerals," *Mineral Physics and Crystallography: A Handbook of Physical Constants, AGU Ref. Shelf*, vol. 2, pp. 18–28, 1995.

[162] Z. Wang, T. A. Palmer, and A. M. Beese, "Effect of processing parameters on microstructure and tensile properties of austenitic stainless steel 304L made by directed energy deposition additive manufacturing," *Acta Materialia*, vol. 110, pp. 226–235, 2016.

[163] L. W. Finger and Y. Ohashi, "The thermal expansion of diopside to 800 degrees C and a refinement of the crystal structure at 700 degrees C," *American Mineralogist*, vol. 61, no. 3-4, pp. 303–310, 1976.

[164] D. Gawin, F. Pesavento, and B. Schrefler, "Towards prediction of the thermal spalling risk through a multi-phase porous media model of concrete," *Computer Methods in Applied Mechanics and Engineering*, vol. 195, no. 41-43, pp. 5707–5729, 2006.

[165] J.-C. Mindeguia, P. Pimienta, A. Noumowé, and M. Kanema, "Temperature, pore pressure and mass variation of concrete subjected to high temperature—experimental

and numerical discussion on spalling risk," *Cement and Concrete Research*, vol. 40, no. 3, pp. 477–487, 2010.

VITA

Kenneth Arthur Hart Jr. (Kip) was born in November 1991 and is a native of Baltimore, Maryland. In 2007, he and his brother founded The South African Lacrosse Project, a non-profit dedicated to improving the lives of children affected by HIV through the sport of lacrosse. The lacrosse project has sponsored lacrosse camps in South Africa for 12 years and was recognized by Lacrosse Magazine as the #1 opportunity to "take lacrosse on the road." After graduating high school in 2009, Kip enrolled in the aerospace engineering program at the University of Maryland. While at Maryland, he was an Omicron Delta Kappa Top 10 Freshman, a member of Tau Beta Pi and Omicron Delta Kappa, the president of Sigma Gamma Tau, and a recipient of the Sigma Gamma Tau Mid-Atlantic Regional Award. In 2013, Kip received a bachelor's of science with honors in aerospace engineering and enrolled at the Georgia Institute of Technology to pursue a doctorate in aerospace engineering. He was also honored with the Aviation Week Twenty20s Award, in recognition of his leadership, community service, and scholastic achievements.

At Georgia Tech, Kip began studying planetary entry, descent, and landing under Prof. Robert D. Braun. He developed a fast algorithm to predict the aerodynamics of low-earth orbiting satellites and created the aerodynamic database for RANGE, the first satellite mission from Georgia Tech. In 2016, Prof. Braun was named Dean of the College of Engineering at the University of Colorado Boulder and, consequently, Kip joined the Computational Solid Mechanics Laboratory to study under Prof. Julian J. Rimoli. His thesis topic, numerical simulation of thermal spallation, combines his passion for human space exploration with his talent for modeling and simulation. After graduating from the Georgia Institute of Technology, Kip will pursue a career at Blue Origin.